Energy Calibration of SNO for measurement of the Charged-Current Neutrino Reaction

by

André Stéphane Hamer

A thesis submitted to the Department of Physics
in conformity with the requirements for
the degree of Doctor of Philosophy

Queen's University
Kingston, Ontario, Canada
October, 1999

©1999 A.S. Hamer

To Rosalie

Abstract

The following thesis presents a detailed description of devices and methods used to calibrate and verify the energy response of the Sudbury Neutrino Observatory (SNO). Accurate measurements of this response are required for the analysis of solar neutrino data. This analysis will include the determination of the ^{8}B neutrino flux above a low energy threshold, and the energy spectrum of neutrinos detected via the charged-current reaction.

The primary calibration device described uses 6.13 MeV γ-rays from the decay of ^{16}N and has been implemented in the SNO detector. Other radioisotope sources that are described are the ^{8}Li source which provides β's with an endpoint near 13 MeV, and the ^{17}N source which provides neutrons. Proof of principle results for each of these sources are presented. A description of how the ^{16}N source data will be used to extract details of the energy response, such as energy scale and resolution, and position and direction dependence within the fiducial volume, is also given. Preliminary studies of the energy response of the SNO detector using these methods with ^{16}N data are presented.

Acknowledgements

I would first like to thank my supervisor Art McDonald for his guidance throughout the course of my graduate education, in particular in the writing of this thesis. I would also like to thank Aksel Hallin, Peter Skensved, Emmanuel Bonvin, Henry Lee, Fraser Duncan, and fellow graduate students Mark Boulay, Richard Ford, Chris Jillings, Ed Korpach, and Bryce Moffat for many useful discussions on physics, the calibration of SNO, and data analysis. A special thanks to Chuck Hearns and Hardy Seifert for their assistance in making things happen underground. I would like to acknowledge all the individuals who worked on gaseous radioactive sources for calibration of SNO. These people include Bhaskar Sur, Davis Earle, Guy Jonkmans, Ron Deal and Earle Gaudette at Chalk River Nuclear Laboratories; Yuen-Dat Chan, Rick Norman and Mike Dragowsky from Lawrence Berkeley Laboratories, Jason Hewett from Laurentian University and Nathaniel Tagg from the University of Guelph. Finally, I would like to thank my wife Rosalie for her patience, love, and support.

Statement of Originality

All the work, results and conclusions presented in this thesis are original except where noted in the text and below.

Because SNO is a large project, many of the systems described in this thesis, especially in Chapter 3, are the result of over one hundred collaboration member's efforts. The author participated in many aspects of the detector construction, and research and development. The most substantial contribution was in the design and construction of radioisotope transfer systems for ^{16}N, ^{17}N, and ^{8}Li sources, and installation and testing of the DT generator and radioactive gas transfer systems underground. The overall work on gaseous radioactive sources was carried out with collaboration members from Chalk River Nuclear Laboratories, Laurentian University, Lawrence Berkeley Laboratories, and the University of Guelph.

All simulations, analysis, and analysis methods presented are the author's own. Separate and concurrent analyses of the air-fill ^{16}N data were done by Chris Jillings (Queen's University) and Mike Dragowsky (Lawrence Berkeley Laboratories). A separate and concurrent study of the systematics associated with the ^{16}N source energy calibration was also done by Mike Dragowsky.

Contents

List of Figures

List of Tables

List of Acronyms and Abbreviations

ADC	Analog-to-Digital Converter
ASYNC	Asynchronous
BKS	Bahcall, Krastev, and Smirnov analysis of combined neutrino results
BooNE	Booster Neutrino Experiment at FERMILAB
CC	Charged-Current
CERN	European Laboratory for Particle Physics
CERNLIB	CERN software library
CMA	Control, Monitors and Alarms system
CMOS	Complementary Metal-Oxide Semiconductor
CNO	Carbon-Nitrogen-Oxygen (cycle of nuclear reactions)
DAQ	Data acquisition system
DB	Daughter Board
DT	Deuterium-Tritium
ECA	Electronics Calibration Analysis
eCPU	Embedded CPU
EGS4	Electron Gamma Shower computer code (version 4)
ES	Electron Scattering
ESUM	Charge sum trigger signal
FEC	Front End Card
FWHM	Full Width at Half Maximum
GALLEX	Gallium experiment
GEANT	CERNLIB Monte Carlo code system
GT	Global Trigger
HBOOK	CERNLIB histograming package
hep	$^3He + p \longrightarrow ^4He + e^+ + \nu_e$

HOMESTAKE	Homestake mine chlorine neutrino experiment
HV	High Voltage
INCO	INternational Nickel Company
KARMEN	KArlsruhe Rutherford Medium Energy Neutrino Experiment
K2K	KEK to Kamiokande long baseline neutrino experiment
LAMPF	Los Alamos Meson Physics Facility
LED	Light Emitting Diode
LSND	Liquid Scintillating Neutrino Detector
MC	Monte Carlo
MCNP	Monte Carlo code for Neutron and Photon transport
MINOS	Main Injector Neutrino Oscillation Search
MPE	Multiple Photo-Electron
MSW	Mikeyev-Smirnov-Wolfenstein matter oscillation effect
MTC	Master Trigger Card
NC	Neutral-Current
NCD	Neutral-Current Detector (^{3}He-filled proportional counter)
NHIT	Number of PMTs fired in an event
OCA	Optical Calibration Analysis
PCA	PMT Calibration Analysis
PE	Photo-Electron
pep	$p + e + p \longrightarrow d + \nu_e$
PGT	Pulsed Global Trigger
PMT	Photomultiplier tube
PMTIC	PMT HV Interface Card
PSUP	PMT support structure
QHL	High gain/long integration time charge measure

QHS	High gain/short integration time charge measure
QLX	Low gain/selectable integration time charge measure
RMS	Root Mean Square
SAGE	Soviet American Gallium Experiment
SBC	Single Board Computer
SHARC	SNO Hardware Acquisition and Readout Control
SNO	Sudbury Neutrino Observatory
SNODB	SNO DataBase
SNOMAN	SNO Monte Carlo and ANalysis program
SNP	Solar Neutrino Problem
SNU	Solar Neutrino Unit
SPE	Single Photo-Electron
SSM	Standard Solar Model
TCP/IP	Transmission Control Protocol/Internet Protocol
TUB	Trigger Utility Board
VME	Virtual Machine Extension BUS
XSNOED	SNO Event Display program
ZEBRA	CERNLIBs FORTRAN memory management package

Chapter 1

Introduction

All of the past solar neutrino experiments, Homestake [1], Kamiokande [2], GALLEX [3], SAGE [4], and just recently, SuperKamiokande [5], have shown a deficit in the observed solar neutrino fluxes when compared to the theoretical estimates. This deficit is commonly referred to as the Solar Neutrino Problem (SNP). Various astrophysical and particle physics explanations have been postulated which can explain this deficit. Present data favor particle physics explanations which imply physics beyond the standard electroweak model [6], namely neutrino mass and non-flavor-conserving processes called neutrino oscillations [7–9]. Such models have the electron neutrinos, ν_e, produced in nuclear reactions in the Sun, transform into neutrinos of other flavors (ν_μ and ν_τ) which are more difficult or impossible to detect with the experiments to date. Certain of these models predict not only a deficit in the observed fluxes, but in some instances predict a distortion in the solar neutrino energy spectrum.

The Sudbury Neutrino Observatory (SNO) is a heavy water (D_2O) Čerenkov detector designed to study all types of neutrinos from the Sun and hopefully resolve the SNP by model-independent means. The use of D_2O as a target medium permits the detection of solar neutrinos via three reactions, the elastic-scattering (ES), charged-current (CC), and neutral-current (NC) reactions. The CC reaction is sensitive exclusively to electron neutrinos, and the NC reaction is sensitive to all active neutrino types. The combined analysis of these signals will provide unique tests for neutrino oscillations and aid in resolving the SNP. An understanding of the detector response to these signals is crucial to the success of SNO.

The following thesis describes the determination of the SNO detector response to neutrinos. In particular, SNO's absolute energy scale and resolution as a function of event position and direction within the detector's fiducial volume is studied. This is required for determining the low energy neutrino threshold which is used in the neutrino flux determinations, as well as for measuring distortions in the CC energy spectrum.

Because of the complexity and size of the SNO detector, its response can only be understood through extensive simulations and calibrations. A large component of this work is therefore devoted to the description of calibration devices designed for this purpose. In particular, the development and construction of a class of calibration devices which use a commercial deuterium-tritium (DT) generator to produce short-lived radioisotopes such as ^{16}N, ^{17}N, and ^{8}Li are described. These radioisotopes are transported to the SNO detection volume where they decay producing γ-rays, neutrons, and β-rays, respectively. The main source discussed is the 6.13 MeV γ-ray from the decay of ^{16}N. It will provide SNO with a measure of the absolute energy scale and resolution of the detector, as well as a measure of the angular response to gamma-rays.

The ^{16}N source has been deployed in the SNO detector and the results of these preliminary calibrations are presented. This includes an analysis of data taken prior to the introduction of D_2O and just after the final fill. The ^{16}N "air-fill" results permitted a better understanding of the detector γ-ray response during this period. Data after D_2O fill permitted a preliminary study of the detector energy scale and resolution, as well as the position dependence of the energy response. This data is considered preliminary because, as this thesis was nearing completion, the SNO detector was still in the final stages of commissioning and had not been fully optimized. The status of the SNO detector will be discussed.

Thesis organization

The chapters are organized as follows. In chapter 2, the present state of solar neutrino astrophysics (theory and experiment) is reviewed. The motivation for new experiments like SNO is given. In chapter 3, a description of the Sudbury Neutrino Observatory and its various systems is provided. Possible strategies for neutrino analysis in the first year of data taking are outlined. Chapter 4 is a discussion of the calibration methods used to understand the detector response. Special attention is given to the energy response. Chapter 5 is a discussion of SNO's radioisotope calibration sources. A description of the associated hardware and its development is given. Chapter 6 presents a discussion of the ^{16}N source simulation and the sensitivity of the ^{16}N calibration for studying the energy response. Chapter 7 reports on preliminary ^{16}N source measurements done during the commissioning stages of the project. This includes energy scale and resolution measurements, as well as measurements of the position and directional dependence of the energy response. Chapter 8 concludes with a discussion of SNO's future measurements and a summary of the work and results presented in this thesis.

Chapter 2

Solar Neutrino Physics

2.1 Search for a neutrino mass

Neutrinos are extremely light or massless, electrically neutral, spin 1/2 particles which are sensitive only to the weak nuclear force and gravity. Neutrinos belong in the lepton family in the particle physics hierarchy. There are three types, or flavors, each associated with one of the massive leptons (ν_e with electrons, ν_μ with muons, and ν_τ with taus). Neutrino interactions are described by the standard electroweak model [6]. In the model, neutrinos are massless and flavor is conserved. If the neutrino were demonstrated to have mass or change flavor, it would have important implications in the fields of particle physics, astrophysics, and cosmology.

Many experiments have been designed and built to search for a neutrino mass (see [10] for a recent review). They include kinematic searches from tritium β decay, double β decay experiments, and searches for neutrino oscillations. Oscillations are clear indicators of a neutrino mass and imply the transformation of one flavor of neutrino into another as they propagate through space or through matter (a detailed description is given in section 2.4). The level of transformation depends on the neutrino energy, the path distance or baseline, and the density of matter through which it propagates. Oscillation experiments can be classified as solar, atmospheric, reactor, or accelerator based. The solar neutrino experiments study neutrinos produced in the energy-generating nuclear reactions in the Sun. Similarly, reactor experiments study neutrinos produced in fission reactors. The neutrinos for the atmospheric experiments are produced when cosmic ray protons collide with nuclei in the upper atmosphere. Accelerator-based experiments use relativistic protons to produce pions or kaons which subsequently decay resulting in an intense beam of neutrinos.

Of all the experiments, only two claim direct evidence for a neutrino mass via oscillations. Direct evidence implies a detection of the transformed neutrino species (i.e an appearance experiment), or some other observation which is model-independent. The first claim is by the SuperKamiokande collaboration [11]. Many experiments have shown a deficit in the observed ratio of ν_μ to ν_e atmospheric neutrinos [12]. This can be explained if the ν_μ's oscillate to ν_τ neutrinos. This ratio, however, is dependent on some theoretical inputs. SuperKamiokande confirmed this deficit, but also measured its zenith angle dependence. The zenith angle is the reconstructed direction of the incoming neutrino with respect to the horizon. Events with different zenith angles therefore correspond to different oscillation baselines varying from 20 km (downward going) to 13 000 km (upward going) . An apparent up-down asymmetry in the ν_μ/ν_e ratio was measured by SuperKamiokande, and this is strong model-independent evidence for neutrino oscillations. Confirmation of the atmospheric neutrino result will be sought by the next generation of long baseline accelerator experiments such as MINOS [13] and K2K [14].

The second claim of direct evidence for neutrino oscillations is by the LSND collaboration. They use the LAMPF accelerator to produce π^+'s which subsequently decay via $\pi^+ \rightarrow \mu^+\nu_\mu$ followed by $\mu^+ \rightarrow e^+\nu_e\overline{\nu}_\mu$. Both $\overline{\nu}_\mu \rightarrow \overline{\nu}_e$ [15] and $\nu_\mu \rightarrow \nu_e$ [16] oscillations are reported to have been observed and hence represent reappearance measurements. Similar experiments, most notably KARMEN [17] show no such evidence, and therefore the LSND result is considered controversial. KARMEN, however, is not sensitive to the entire LSND oscillation solution parameter space. New experiments such as BooNE [18] will have much greater sensitivity and should confirm or refute the LSND result.

There is also strong evidence, albeit indirect, from the observed solar neutrino deficit, or Solar Neutrino Problem (SNP). No single experiment, however, can claim model-independent proof that neutrino oscillations explain the SNP. The Sudbury Neutrino Observatory, which is described in the subsequent chapters, will hopefully provide such a proof.

Because SNO is primarily a solar neutrino experiment, the following sections introduce the subject of solar neutrino physics in more detail, beginning with a discussion of neutrino production in the Sun. This is followed by a discussion of earlier solar neutrino experiments and the discovery of the SNP. A discussion of neutrino oscillations and their impact on the solar neutrinos is given. Finally a discussion of model independent tests and the motivation for future experiments like SNO is given.

2.2 Neutrino production in the Sun

Energy is generated in the Sun via a sequence of nuclear reactions which ultimately result in the fusion of four protons into an alpha particle, two positrons, and two electron neutrinos with a total released energy of 26.73 MeV. The main sequence of reactions is the pp chain shown in Figure 2.1, with a small contribution (1.5 %) from the CNO cycle of reactions shown in Figure 2.2. Various of these reactions involve neutrino production. The neutrino energy spectrum for most of these reactions is a continuous β-decay spectrum. Two reactions, however, produce monoenergetic neutrinos (the "pep" and ^{7}Be neutrinos). The shapes of the neutrino spectra, for each individual reaction, are well understood from weak interaction and nuclear physics, and have little to do with conditions in the Sun. The calculated rates for neutrino production, however, are calculated using models based on our understanding of stellar evolution.

The Standard Solar Models, or SSMs, used to simulate the Sun's evolution are based on widely accepted stellar evolution equations and input parameters, and assumptions made about the Sun. Input parameters include nuclear reaction cross-sections, chemical abundances, and radiative opacities. Basic assumptions include hydrostatic equilibrium, energy generation via fusion reactions,

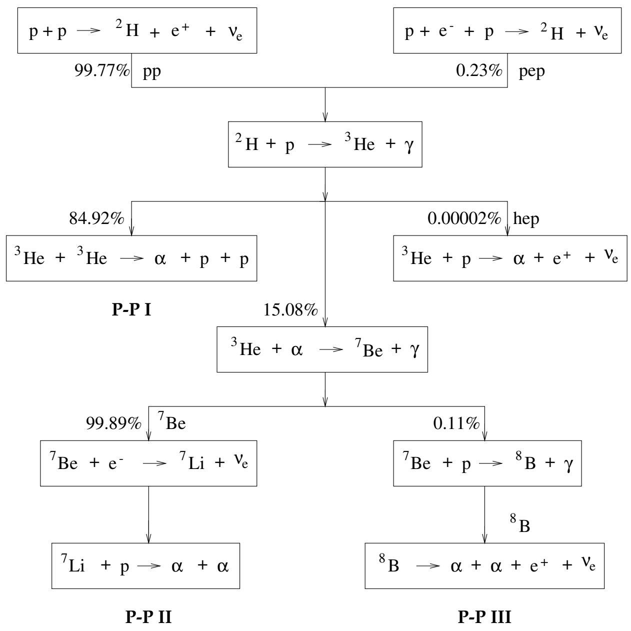

Figure 2.1: The pp chain of nuclear reactions.

and energy transport via photons and convection. It is also assumed that abundance changes are due to nuclear reactions. Unknown parameters, such as the initial ^{3}He abundance, are tuned until the product of the models evolution agrees with present day observations such as the photon luminosity, mass, radius, and best estimates of the solar age. For the most part, the SSMs agree very accurately with a large body of solar observations including recent helioseismological data [19]. The exceptions are the calculated neutrino fluxes.

The recent Bahcall and Pinsonneault SSM, BP98 [20], calculates the neutrino fluxes given in Table 2.1 for both the pp chain and CNO cycle. The BP98 energy spectra are shown in Figure 2.3. Also given in Table 2.1 is the maximum energy of the various neutrino spectra and the capture rates for two of the experiments discussed in the following section. The capture rates are presented in Solar Neutrino Units or SNUs which corresponds to 10^{-36} events per target atom per second. The pp flux is by far the greatest and its theoretical uncertainty is low because of accurate calculations of its reaction cross-sections and its relation to the observed solar luminosity. The pp endpoint energy

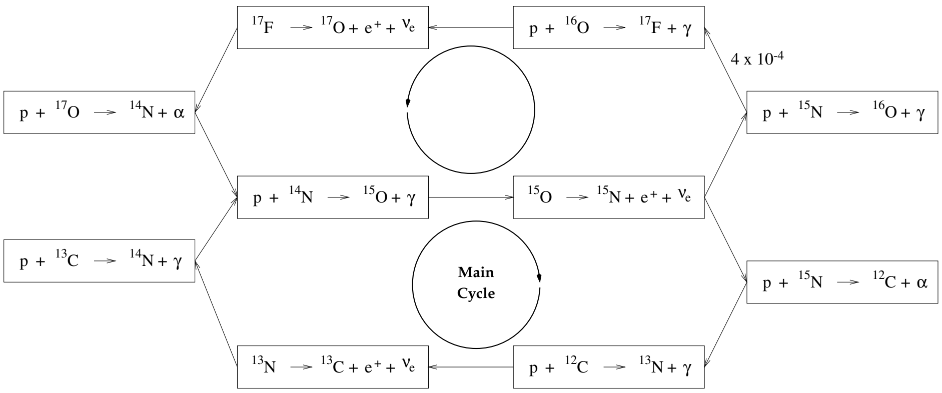

Figure 2.2: The CNO cycle of nuclear reactions.

Table 2.1: The SSM predicted neutrino fluxes and capture rates for the chlorine and gallium experiments [20]. Also given is the maximum neutrino energy for each reaction.

Reaction	Flux ($cm^{-2}s^{-1}$)	Max E (MeV)	Cl (SNUs)	Ga (SNUs)
pp	$5.94(1.00^{+0.01}_{-0.01})\text{x}10^{10}$	0.42	0.0	69.6
pep	$1.39(1.00^{+0.01}_{-0.01})\text{x}10^{8}$	1.44	0.2	2.8
hep	$2.10\text{x}10^{3}$	18.77	0.0	0.0
^{7}Be	$4.80(1.00^{+0.09}_{-0.09})\text{x}10^{9}$	0.86 (90 %)	1.15	34.4
		0.38 (10 %)		
^{8}B	$5.15(1.00^{+0.19}_{-0.14})\text{x}10^{6}$	≈15	5.9	12.4
^{13}N	$6.05(1.00^{+0.19}_{-0.13})\text{x}10^{8}$	1.20	0.1	3.7
^{15}O	$5.32(1.00^{+0.22}_{-0.15})\text{x}10^{8}$	1.73	0.4	6.0
^{17}F	$6.33(1.00^{+0.12}_{-0.11})\text{x}10^{6}$	1.74	0.0	0.1
Total			$7.7^{+1.2}_{-1.0}$	129^{+8}_{-6}

is, however, lower than the thresholds of all but the Ga (see below) solar neutrino experiments so far. The higher energy neutrinos with a sufficient rate for observation on Earth are from the ^{7}Be and ^{8}B reactions. Unfortunately the theoretical uncertainties for these fluxes are somewhat higher due mostly to uncertainties in measured nuclear cross-sections and rates.

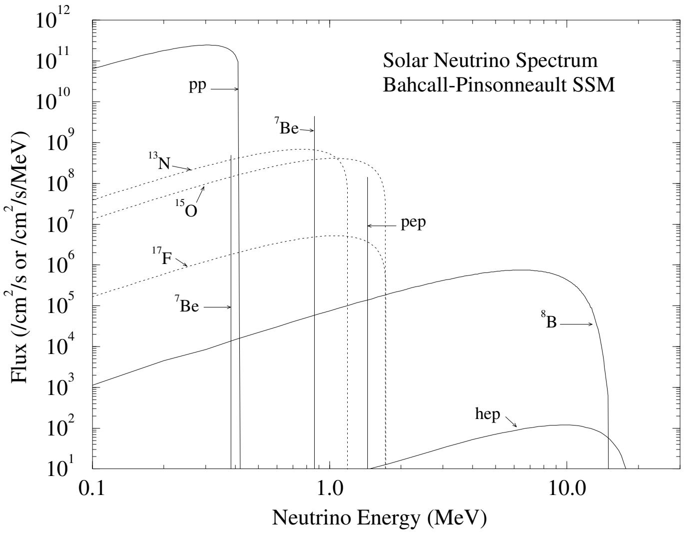

Figure 2.3: The SSM solar neutrino energy spectra. Spectra for both the pp chain and CNO cycle are shown. The flux is given in $\mathrm{cm}^{-2}\mathrm{s}^{-1}$ per MeV bin for the spectra, and in $\mathrm{cm}^{-2}\mathrm{s}^{-1}$ for the mono-energetic lines. Taken from BP98 [20].

2.3 The neutrino detection experiments and the Solar Neutrino Problem

Prior to SNO, there have been five solar neutrino experiments: Homestake, Kamiokande (II and III), GALLEX, the Soviet American Gallium Experiment (SAGE), and SuperKamiokande. Homestake, GALLEX, and SAGE are radiochemical experiments which detect inverse beta decay reactions induced by electron neutrinos, and the Kamiokande experiments are light water Čerenkov

Table 2.2: Experimental versus theoretical fluxes for past experiments. The uncertainties in the measured values in some instances include both statistical and systematic values. The ratio of result to theory includes only experimental errors. Table taken from [26].

Experiment	SSM prediction	Measured value	Result/Theory
Homestake [SNU]	$7.7^{+1.2}_{-1.0}$	$2.56\pm0.16 \pm 0.16$	0.33 ± 0.029
Kamiokande [x10^6cm^{-2}s^{-1}]	$5.15(1.00^{+0.14}_{-0.17})$	$2.80\pm0.19 \pm 0.33$	0.54 ± 0.07
Gallex [SNU]	129^{+8}_{-6}	$77.5\pm6.2^{+4.3}_{-4.7}$	0.60 ± 0.06
SAGE [SNU]	129^{+8}_{-6}	$66.6^{+7.8}_{-8.1}$	0.52 ± 0.06
SuperKamiokande [x10^6cm^{-2}s^{-1}]	$5.15(1.00^{+0.14}_{-0.17})$	$2.44\pm0.05^{+0.09}_{-0.007}$	0.474 ± 0.020

detectors. A summary of the various detector results and SSM predictions are shown in Table 2.2 [21–25].

Homestake is the original solar neutrino experiment. It consists of a target made of 615 tonnes of perchloroethylene (C_2Cl_4) in a tank located in the Homestake gold mine in Lead, South Dakota. The absorption reaction is

$$\nu_e +^{37} Cl \longrightarrow e^- +^{37} Ar \tag{2.1}$$

with a 0.8 MeV threshold and therefore is sensitive mainly to the ^{8}B and ^{7}Be neutrinos. After between one and three month exposure times, the ^{37}Ar is extracted from the holding tank and the decays by electron capture (τ_{half}=35 days) are counted with low-background proportional counters. As shown in Table 2.2, the Homestake results are much lower than the predicted SSM values. The discrepancy between the experimental and theoretical fluxes has come to be known as the Solar Neutrino Problem (SNP).

The Kamiokande and SuperKamiokande experiments detect Čerenkov photons radiated from the recoil electrons from the neutrino-electron elastic scattering interaction,

$$\nu_x + e^- \longrightarrow \nu_x + e^- \tag{2.2}$$

in water with an approximately 7 MeV energy threshold. All neutrino flavors, ν_x, can be detected via this interaction but the cross-section for ν_e is approximately six times higher. The Kamiokande experiments are sensitive only to the higher energy ^{8}B and hep neutrinos, but unlike the radio-chemical experiments they measure the neutrinos in real time and have directional sensitivity. The original Kamiokande experiment consisted of a 3000 tonne target of water with a 680 tonne fiducial volume, and 948 50-cm diameter PMTs providing about 20 % of 4π photocathode coverage. Kamiokande confirmed neutrino production in the Sun and the solar neutrino deficit. SuperKamiokande consists of 50000 tonnes of water with a 22500 tonne fiducial volume. It has 11200 50-cm diameter PMTs providing about 40 % of 4π photocathode coverage. It has confirmed the earlier Kamiokande measured flux with a lower uncertainty.

For GALLEX and SAGE, the reaction is

$$\nu_e +^{71} Ga \longrightarrow e^- +^{71} Ge \tag{2.3}$$

with a 0.233 MeV threshold. Mostly pp neutrinos are detected but contributions from the other neutrinos are important. The target for SAGE (Baksan, former Soviet Union) is 60 tonnes of metallic Ga, and that of GALLEX (Gran Sasso, Italy), a gallium chloride solution containing 30.3 tonnes of Ga. The ^{71}Ge atoms are chemically separated from the gallium or gallium chloride solution approximately every 20-50 days and the subsequent decay (τ_{half}=11.4 days) is counted with low-background proportional counters. The results for both experiments agree and confirm the solar neutrino deficit.

Further inspection based on the combined analysis of data shows other important features. The Kamiokande experiment detects mainly the ^{8}B neutrinos, and Homestake detects both the ^{8}B and ^{7}Be neutrinos. The reduction in flux is greater for the Homestake experiment and can be explained if there is a preferential reduction in the ^{7}Be neutrinos. Also the Ga experiments can be explained by a reduction in the ^{7}Be and ^{8}B fluxes and do not require a reduction in the lower energy pp neutrinos. This indicates a possible energy dependence in the neutrino flux reduction.

2.4 Various solutions to the Solar Neutrino Problem

Proposed solutions to the SNP can be classified as either astrophysical in nature or due to particle physics beyond the standard electroweak model. The proposed astrophysical solutions are basically solar models in which non-standard input parameters or assumptions are used. The particle physics solutions postulate properties of the neutrino, such as mass or magnetic moment, that have so far eluded measurement. Such neutrino properties permit oscillation behavior in which a neutrino's flavor can change as it propagates.

2.4.1 Astrophysical solutions

The simplest solution for reducing the solar neutrino flux would be to lower the solar core temperature and hence reduce the neutrino-producing nuclear reaction rates. Many mechanisms have been proposed which could cool the central core (see Bahcall [29]). The more popular theories involve some sort of mixing of the stellar material. Most of these non-standard models can be shown to be inconsistent with the observed ratio of ^{7}Be to ^{8}B neutrino fluxes inferred from a comparison to the experimental results to date [27]. ^{3}He mixing, as proposed by Cumming and Haxton, under certain conditions could explain a lower ^{7}Be production rate, yet still maintain the observed ^{8}B rate [28]. Recent helioseismological data, however, have verified many of the standard model predictions and have made solar core cooling scenarios unlikely[19]. For example, the helioseismological data permits accurate measurements of the sound velocities in the Sun. The sound velocities scale with the square root of the mean local temperature divided by the mean molecular weight. The required cooling to explain the observed reduction in neutrino flux, and mixing in the solar core, is quite inconsistent with the helioseismological determination of the sound velocities.

Other explanations are based on the uncertainties of the various solar nuclear reaction cross-sections. Many of these cross-sections are uncertain because the energies of particles in the Sun are considerably lower than is achievable with the laboratory experiments used to measure nuclear cross-sections. In many instances the cross-sections at solar energies must be extrapolated. If, for example, the ^{3}He(^{3}He,2p)^{4}He reaction has a resonance at low energy, the PPI chain termination would dominate and there would be many fewer ^{7}Be and ^{8}B neutrinos produced. Such a resonance has not been totally ruled out, but even if such a resonance exists it could not explain the ratio of the ^{7}Be to ^{8}B fluxes. Another important reaction is ^{7}Be(p,γ)^{8}B which is the precursor to the ^{8}B decay. Varying the cross-section for this interaction in the solar models will affect the calculated fluxes, but still can not explain the observed ^{7}Be and ^{8}B fluxes.

2.4.2 Neutrino oscillations

Most particle physics explanations to the SNP consist of non-flavor-conserving processes in which neutrinos produced in the Sun, ν_e, are transformed into different types of neutrinos as they propagate. The processes are called neutrino oscillations and they usually involve a finite neutrino mass. Some of the basic formalism is developed below. A more detailed review can be found in Bahcall [29] and references therein.

Vacuum oscillations

The simplest of these processes are vacuum oscillations which were first proposed by Pontecorvo [7]. The key to vacuum oscillations is that the flavor eigenstates of the weak interaction ($|\nu_e>$, $|\nu_\mu>$, and $|\nu_\tau>$) are not the same as those of the mass eigenstates ($|\nu_1>$, $|\nu_2>$, and $|\nu_3>$). It is the mass eigenstates that are used in the quantum mechanical description of the neutrino propagation through space. If the masses of these eigenstates are different, their relative phases will change as they propagate. Because each weak eigenstate is a superposition of mass eigenstates, the flavor of the original neutrino can therefore change.

In the simplified case of only two neutrino flavors, the weak and mass eigenstates are related as follows,

$$\begin{pmatrix} |\nu_e> \\ |\nu_\mu> \end{pmatrix} = U \begin{pmatrix} |\nu_1> \\ |\nu_2> \end{pmatrix} = \begin{pmatrix} \cos\theta_V & \sin\theta_V \\ -\sin\theta_V & \cos\theta_V \end{pmatrix} \begin{pmatrix} |\nu_1> \\ |\nu_2> \end{pmatrix} \tag{2.4}$$

where θ_V is the mixing angle in vacuum, the analogue of the Cabibbo angle in the case of quark flavor mixing, and U is a unitary matrix. The time evolution of the mass eigenstates is given by the Schrödinger equation

$$i\frac{d}{dt}\begin{pmatrix} |\nu_1> \\ |\nu_2> \end{pmatrix} = \begin{pmatrix} E_1 & 0 \\ 0 & E_2 \end{pmatrix} \begin{pmatrix} |\nu_1> \\ |\nu_2> \end{pmatrix}. \tag{2.5}$$

For relativistic neutrinos, one can make the approximation,

$$E_i = \sqrt{p_i^2 + m_i^2} \approx p_i + \frac{m_i^2}{2p_i^2}, \tag{2.6}$$

and if it is assumed that $p_1 \approx p_2 = p \approx E$, then

$$\begin{pmatrix} E_1 & 0 \\ 0 & E_2 \end{pmatrix} \approx p \begin{pmatrix} 1 & 0 \\ 0 & 1 \end{pmatrix} + \frac{1}{2E}\begin{pmatrix} m_1^2 & 0 \\ 0 & m_2^2 \end{pmatrix}. \tag{2.7}$$

Using the above, and removing common phases, equation 2.5 can be written

$$i\frac{d}{dt}\begin{pmatrix} |\nu_1> \\ |\nu_2> \end{pmatrix} = \frac{1}{2E}\begin{pmatrix} m_1^2 & 0 \\ 0 & m_2^2 \end{pmatrix} \begin{pmatrix} |\nu_1> \\ |\nu_2> \end{pmatrix}, \tag{2.8}$$

and its solution given by

$$\begin{pmatrix} |\nu_1> \\ |\nu_2> \end{pmatrix} = \begin{pmatrix} e^{-im_1^2 t/2E} & 0 \\ 0 & e^{-im_2^2 t/2E} \end{pmatrix} \begin{pmatrix} |\nu_1> \\ |\nu_2> \end{pmatrix}. \tag{2.9}$$

Using the above and relation 2.4, the survival probability at time t for an electron neutrino produced at time t=0 is given by

$$\begin{aligned} P_{ee} = &\ <\nu_e(t)|\nu_e(0)>^2 \\ = &\ \left(\begin{pmatrix} 1 & 0 \end{pmatrix} U \begin{pmatrix} e^{-im_1^2 t/2E} & 0 \\ 0 & e^{-im_2^2 t/2E} \end{pmatrix} U^{-1} \begin{pmatrix} 1 \\ 0 \end{pmatrix}\right)^2 \\ = &\ 1 - \sin^2(2\theta_V)\sin^2\left(\frac{\Delta m^2 t}{4E}\right) \end{aligned} \tag{2.10}$$

where Δm^2 equals $m_2^2 - m_1^2$. If one replaces t by the distance traveled, L, and introduces the following parameter, $L_\nu = 4\pi E/\Delta m^2$, known as the vacuum oscillation length, equation 2.10 becomes the more familiar survival probability equation

$$P_{ee} = 1 - \sin^2(2\theta_V)\sin^2\left(\frac{\pi L}{L_\nu}\right). \tag{2.11}$$

The above equation can be used in interpreting accelerator, atmospheric, and solar neutrino oscillation experiments. The Δm^2 range which these experiments can probe varies enormously. For example the LSND experiment reports Δm^2 values in the 10^{-1}-10^1 eV^2 range, and the SuperKamiokande atmospheric result is in the 10^{-3}-10^{-2} eV^2 range. Because of the large Earth-Sun distance, values of Δm^2 as low as 10^{-12} eV^2 can be probed with solar neutrino experiments.

Oscillation experiments report not only the Δm^2 values but also the mixing angle in terms of $\sin^2(2\theta_V)$. A recent analysis of the combined solar neutrino experimental results compared to the BP98 solar model predictions was done by Bahcall, Krastev, and Smirnov (BKS) [26]. The analysis where they considered the averaged event rates in all the experiments favors ($\Delta m^2 = 8.0\text{x}10^{-11} eV^2$, $\sin^2(2\theta_V) = 0.75$) for a vacuum oscillation solution. Figure 2.4 shows their contour plot of Δm^2 versus $\sin^2(2\theta_V)$ corresponding to the allowed regions that could explain the SNP. Note that the allowed solutions require a large mixing angle. Such solutions can result in a distortion of the observed ^{8}B ν_e energy spectrum or a seasonal dependence in the observed flux. Such solutions are called "Just So" because of their dependence on the Sun-Earth distance [30]. When the observed SuperKamiokande energy spectrum was included in the BKS analysis the favored solution became ($\Delta m^2 = 6.5\text{x}10^{-11} eV^2$, $\sin^2(2\theta_V) = 0.75$).

MSW oscillations

An attractive oscillation scenario is that given by the MSW effect introduced in the papers by Wolfenstein, and by Mikheyev and Smirnov [8, 9]. When neutrinos propagate through matter, the potentials due to interactions with the matter must be taken into account in the time evolution equations. In the Sun, neutrinos can interact with the stellar material via neutral-current and

Figure 2.4: The vacuum oscillation solution parameter space. Regions in the Δm^2-$\sin^2(2\theta_V)$ parameter space for vacuum oscillations allowed by the rates observed in the radiochemical and SuperKamiokande experiments are shown. The best-fit is indicated by the dark circle. Taken from [26].

charged-current interactions. The charged-current reactions, however, only act on the electron neutrinos. The result is that the relative phase between the electron neutrino and the other neutrino flavors changes with distance. This accompanies the phase change due to the mass difference and therefore can enhance the oscillations.

To derive the evolution equations, begin with equation 2.8 for vacuum oscillations and rewrite it in terms of the electroweak eigenstates,

$$i\frac{d}{dt}\begin{pmatrix} |\nu_e> \\ |\nu_\mu> \end{pmatrix} = \frac{1}{2E}\left(U\begin{pmatrix} E_1 & 0 \\ 0 & E_2 \end{pmatrix}U^{-1}\right)\begin{pmatrix} |\nu_e> \\ |\nu_\mu> \end{pmatrix}. \quad (2.12)$$

The potential due to interaction with the electrons must be proportional to the weak interaction coupling constant, G_F, and the local electron density, N_e. Therefore, adding $V_e=\sqrt{2}G_F N_e$ to equation 2.12 gives

$$\begin{aligned} i\frac{d}{dt}\begin{pmatrix} |\nu_e> \\ |\nu_\mu> \end{pmatrix} &= \frac{1}{2E}\left(U\begin{pmatrix} E_1 & 0 \\ 0 & E_2 \end{pmatrix}U^{-1} + \begin{pmatrix} 2EV_e & 0 \\ 0 & 0 \end{pmatrix}\right)\begin{pmatrix} |\nu_e> \\ |\nu_\mu> \end{pmatrix} \\ &= \frac{1}{2E}M^2\begin{pmatrix} |\nu_e> \\ |\nu_\mu> \end{pmatrix}. \end{aligned} \quad (2.13)$$

The above matrix, M^2, has eigenvalues

$$M_j^2 = \frac{1}{2}\left(2EV_e + m_1^2 + m_2^2 \pm \sqrt{(2EV_e - \Delta m^2\cos(2\theta_V))^2 + (\Delta m^2\sin(2\theta_V))^2}\right), \quad (2.14)$$

and eigenstates

$$\begin{pmatrix} |\nu_1^m> \\ |\nu_2^m> \end{pmatrix} = \begin{pmatrix} \cos\theta_m & \sin\theta_m \\ -\sin\theta_m & \cos\theta_m \end{pmatrix}\begin{pmatrix} |\nu_e> \\ |\nu_\mu> \end{pmatrix} \quad (2.15)$$

with the angle θ_m given by

$$\sin^2(2\theta_m) = \frac{(\Delta m^2)^2\sin^2(2\theta_V)}{[(2EV_e - \Delta m^2\cos^2\theta_V)^2 + (\Delta m^2\sin(2\theta_V))^2]}. \quad (2.16)$$

From the above, one notices a resonance when $2EV_e = \Delta m^2\cos^2\theta_V$ and mixing becomes maximal. The time evolution equation for constant density is simply

$$i\frac{d}{dt}\begin{pmatrix} |\nu_1^m> \\ |\nu_2^m> \end{pmatrix} = \frac{1}{2E}\begin{pmatrix} M_1^2 & 0 \\ 0 & M_2^2 \end{pmatrix}\begin{pmatrix} |\nu_1^m> \\ |\nu_2^m> \end{pmatrix} \quad (2.17)$$

which is analogous to the vacuum equation and so the probability for a ν_e produced at t=0 to remain unchanged is

$$P_{ee} = 1 - \sin^2(2\theta_m)\sin^2\left(\frac{\pi L}{L_m}\right) \tag{2.18}$$

where $L_m = 4\pi E/(M_2^2 - M_1^2)$.

In the case when the density is varying, the propagation equation can be written [31]

$$i\frac{d}{dL}\begin{pmatrix} |\nu_1^m> \\ |\nu_2^m> \end{pmatrix} = \frac{1}{2E}\begin{pmatrix} M_1^2 & \frac{-i\Delta m^2 \sin(2\theta_V)}{(M_2^2-M_1^2)^2}E\frac{dD}{dL} \\ \frac{i\Delta m^2 \sin(2\theta_V)}{(M_2^2-M_1^2)^2}E\frac{dD}{dL} & M_2^2 \end{pmatrix}\begin{pmatrix} |\nu_1^m> \\ |\nu_2^m> \end{pmatrix} \tag{2.19}$$

where the time variable has been replaced by distance, L, and $D = 2\sqrt{2}G_F N_e E$. If the off-diagonal elements are negligible, the time evolution is called adiabatic. The adiabatic condition is usually expressed,

$$\frac{\sin^2(2\theta_V)}{\cos(2\theta_V)}\frac{\Delta m^2}{E} \geq 2\pi\left(\frac{|dN_e/dr|}{N_e}\right)_{res} \tag{2.20}$$

and implies a slowly varying density compared to the oscillation length. Under these conditions the eigenstates $|\nu_1^m>$ and $|\nu_2^m>$ are unchanging. However, because the transformation to the weak eigenstates are density dependent, the relative $|\nu_e>$ and $|\nu_\mu>$ fractions will vary. Figure 2.5 shows the effective masses of neutrinos, for a given Δm^2 and $\sin^2(2\theta_V)$, as a function of density and can be used to illustrate adiabatic oscillations. For example, if a ν_e is produced in a region of extremely high density, the $|\nu_e>$ state nearly matches the $|\nu_2^m>$ state. As it propagates out to regions of lower density, the $|\nu_2^m>$ state is unchanging. Finally when it reaches vacuum, the $|\nu_2^m>$ state survives but now matches the $|\nu_\mu>$ state and hence a complete transformation has occurred. For the adiabatic condition, the survival probability is given by

$$P_{ee} = \frac{1}{2}(1 + \cos(2\theta_V)\cos(2\theta_m)). \tag{2.21}$$

When the off-diagonal components of the time evolution matrix are non-negligible, the adiabatic approximation no longer holds. This is most likely to happen near resonance when the mass eigenstates are most alike (i.e nearly degenerate). In this situation the neutrino can jump from one mass eigenstate to another. The jump is similar in nature to quantum mechanical tunneling. The modified survival probability, known as the Parke formula [32], is given by

$$P_{ee} = \frac{1}{2} + \left(\frac{1}{2} - P_{jump}\right) \cos(2\theta_V) \cos(2\theta_m) \tag{2.22}$$

where P_{jump} is the probability to jump from one mass eigenstate to another. P_{jump} for a linear varying density distribution can be approximated by [32]

$$P_{jump} = exp\left[\frac{-\pi\Delta m^2 \sin^2(2\theta_V)}{4\pi\cos(2\theta_V)}\left(\frac{N_e}{|dN_e/dr|}\right)\right]. \tag{2.23}$$

Approximations for other density distributions can be found in [33].

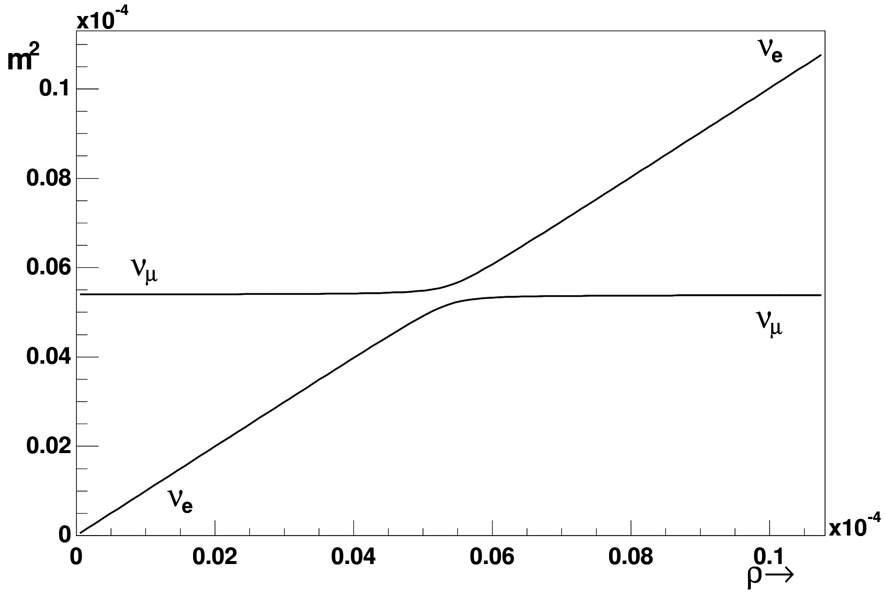

Figure 2.5: The mass eigenstates in matter for the MSW effect. The mass eigenstates are shown as a function of density for $\Delta m^2 = 5.4\text{x}10^{-6} eV^2$ and $\sin^2(2\theta_V) = 6.0\text{x}10^{-3}$. The upper and lower lines represent the ν_2 and ν_1 eigenstates, respectively. All units are in eV^2.

Both approximation equations 2.21 and 2.22, as well as detailed numerical calculations using equation 2.19, have been used in the analysis of solar neutrino data. The combined rate analysis of Bahcall, Krastev, and Smirnov applied to MSW oscillations is shown in Figure 2.6 [26]. Here the favored solutions are ($\Delta m^2 = 5.4\text{x}10^{-6} eV^2$, $\sin^2(2\theta_V) = 6.0\text{x}10^{-3}$) and ($\Delta m^2 = 1.8\text{x}10^{-5} eV^2$, $\sin^2(2\theta_V) = 0.76$). These are commonly referred to as the small and large angle solutions, respectively. A third less likely solution from the BKS analysis is ($\Delta m^2 = 7.9\text{x}10^{-8} eV^2$, $\sin^2(2\theta_V) = 0.96$). Like the vacuum oscillation case, the small angle solution can exhibit an energy dependence. The large angle MSW solutions will not exhibit a significant energy dependence, but because of the possibility of neutrino regeneration through the Earth, can have a day-night dependence [34]. In the BKS analysis where spectral distortions and the day-night effect were taken into account the favored solution is ($\Delta m^2 = 5.4\text{x}10^{-6} eV^2$, $\sin^2(2\theta_V) = 6.3\text{x}10^{-3}$).

Sterile neutrinos and exotic oscillations

Other solutions include MSW conversion into sterile (undetectable) neutrinos [35], neutrino helicity flip in the solar magnetic fields due to a non-zero neutrino magnetic moment [36], and resonant spin-flavor conversion which combines MSW and helicity flip conditions [37, 38]. Presently, small angle MSW conversion into sterile neutrinos provides good fits to the solar neutrino flux data. The combined Bahcall, Krastev, and Smirnov analysis (see Figure 2.7) has the ($\Delta m^2 = 4.3\text{x}10^{-6} eV^2$, $\sin^2(2\theta_V) = 6.9\text{x}10^{-3}$) solution favored [26]. The analysis which takes into account the SuperKamiokande energy spectrum and day-night data gives ($\Delta m^2 = 4.0\text{x}10^{-6} eV^2$, $\sin^2(2\theta_V) = 6.9\text{x}10^{-3}$).

2.5 Model independent tests and the motivation for new experiments

Although there may be evidence from atmospheric neutrinos and perhaps the LSND result that neutrino oscillations do exist, the SNP still remains unsolved. It should be noted in particular that the oscillation parameters reported in the atmospheric and accelerator neutrino based experiments are considerably different than those suggested by the solar neutrino results. This may suggest

Figure 2.6: The MSW oscillation solution parameter space. Regions in the Δm^2-$\sin^2(2\theta_V)$ parameter space for MSW oscillations into active neutrinos allowed by the rates observed in the radiochemical and SuperKamiokande experiments are shown. The best-fits are indicated by the dark circles. Taken from [26].

Figure 2.7: The oscillation solution parameter space for sterile neutrinos. Regions in the Δm^2-$\sin^2(2\theta_V)$ parameter space for MSW oscillations into sterile neutrinos allowed by the rates observed in the radiochemical and SuperKamiokande experiments are shown. The best-fit is indicated by the dark circle. Taken from [26].

that neutrino oscillations are hierarchical. The present solar neutrino data can be interpreted in terms of small angle MSW, large angle MSW, sterile, or vacuum oscillations. The next generation of experiments must distinguish between these various scenarios. More importantly they must provide model-independent proof of solar neutrino oscillations.

All of the above solutions produce a deficit in the solar neutrino flux. Certain ones, however, have solar model-independent signatures. Both the small angle MSW and vacuum solutions distort the ^{8}B energy spectrum. The vacuum oscillation case also has a seasonal variation in flux due to the difference in the Earth-Sun distance throughout the year and the "Just So" nature of the vacuum solution. For the large angle MSW solution, there is no energy dependence but there is a possibility of a day-night effect. Finally, the resonant spin solution has a seasonal dependence due to the varying paths through the Sun's magnetic field and electron density which results from a slightly inclined Earth orbit with respect to the solar equator.

The SuperKamiokande collaboration has looked for such model independent signatures of solar neutrino oscillations and has recently reported analysis results for their 825 day data-set [39]. Possible spectral distortions were investigated by subdividing the observed and predicted (from the BP98 SSM) number of events into energy bins, then determining their ratios as a function of energy. The result is shown in Figure 2.8 along with various oscillation solution predictions. A small excess is observed at high energy but the result is still not statistically significant (see [39]). It has been suggested that the excess may be due to an unexpectedly high hep neutrino rate [40]. A comparison between day (D) and night (N) fluxes was also reported. Here, the data (events above a 6.5 MeV threshold) were subdivided into bins according to the angle (Θ) of the neutrino trajectory with respect to the nadir (line to the Earth's center). The results are shown in Figure 2.9. A small excess ($\approx 2\sigma$) in the night flux is reported with

$$\frac{N}{D} - 1 = 0.067 \pm 0.033(stat.) \pm 0.013(syst.) \tag{2.24}$$

where both statistical (stat.) and systematic (syst.) uncertainties are reported. For the bin, $N5$, associated with the neutrinos traversing the Earth's core ($0.8 < \cos\Theta <= 1.0$), they report the following ratio

$$\frac{N5}{< D, N1 - N4 >} - 1 = 0.006 \pm 0.053 \pm (stat.) \pm 0.013(syst.) \tag{2.25}$$

where $< D, N1-N4 >$ is the average of the day and other night bins. This last observation is significant because it has permitted greater constraints to be made on the small angle solution parameter space. The SuperKamiokande results (flux, energy spectrum, and day-night) have permitted the oscillation parameter space to be constrained. Unambiguous proof that neutrino oscillations are responsible for the SNP, however, can not be concluded from the present results.

Figure 2.8: SuperKamiokande spectrum distortion results. Shown is the ratio of the observed electron energy spectrum to that expected from the SSM. Figure taken from [39].

The next major experiment that will continue the search for solar neutrino oscillations is the Sudbury Neutrino Observatory. SNO is unique in that it detects neutrinos via the CC, NC, and ES reactions. The CC interaction will be sensitive to electron neutrinos only, and because of its enhanced capability for determining the incoming neutrino energy, can be used to probe energy spectrum distortions. The NC reaction is sensitive to all neutrinos equally and therefore a ratio of the CC determined flux to that determined via the NC would be model-independent proof of neutrino oscillations. Similarly, a ratio of the ES determined flux to that determined with the CC

Figure 2.9: SuperKamiokande day-night results. Shown are the ratios of the observed neutrino fluxes to that expected from the SSM for the day-time (Day) and night-time (N1-N5) data. The night-time data is binned using the angle between the neutrino path and the nadir. Figure taken from [39].

reaction would provide such proof, but because of the small fraction of the ES interaction rate due to NC interactions, will be less sensitive. Like SuperKamiokande, SNO is a real-time experiment and hence can probe temporal variations in the flux. Finally, a more sensitive measure of the neutrino flux in the higher hep neutrino energy range will be permitted with CC detection. The combined analysis of these measurements should provide,

- A solar model-independent test for oscillation of solar neutrinos.
- Means for distinguishing amongst the various oscillation scenarios.
- Further constraints for the $\Delta m^2 - \sin^2(2\theta_V)$ solution space if oscillations are observed.
- A better measure of the neutrino flux in the hep energy range.

All this implies that SNO will make significant contributions to physics over the next decade.

Chapter 3

The Sudbury Neutrino Observatory

The Sudbury Neutrino Observatory (SNO) is a second generation solar neutrino experiment designed to further constrain possible solutions to the SNP, but more importantly to provide model-independent proof of neutrino oscillations. It is unique among solar neutrino experiments in that it uses heavy water, D_2O, as a reaction target for neutrinos. In the sections that follow, the neutrino reactions and detection mechanisms are described. This includes a discussion of the detector backgrounds. This is followed by a general description of the detector components. Finally, a discussion of the expected first year of neutrino data is given along with possible analysis schemes.

3.1 Neutrino detection and backgrounds

3.1.1 The detection reactions

The D_2O target in SNO permits neutrino detection via three reaction modes. Below, these detection reactions are first introduced. In section 3.1.2, the details of how the reaction products, relativistic electrons and neutrons, are detected in SNO are given.

The Charged-Current reaction

The first detection mode is via the charged-current (CC) reaction

$$\nu_e + d \longrightarrow p + p + e^-, \tag{3.1}$$

whose energy threshold is given by Q = 1.442 MeV. The total cross-section as a function of energy as calculated by Kubodera and Nozawa [41], Ying, Haxton, and Henley [42], and Bahcall and Ellis [43], is shown in Figure 3.1. Kubodera and Nozawa report a 5 % uncertainty in the cross-section determination. SNO detects the recoil electron energies. Therefore, the differential cross-sections as a function of electron energy for various neutrino energies and scattering angles are shown in Figure 3.2 [44]. In all cases, but particularly at higher energy, most of the neutrino's momentum is imparted to the electron. For this reason, and the fact that it is only sensitive to ν_e neutrinos, the CC reaction is well suited for study of the electron neutrino energy spectrum. Another advantage is the angular distribution of the recoil electrons given by [45]

$$W(\theta_e) = 1 - \frac{1}{3}\cos\theta_e \tag{3.2}$$

where $\cos\theta_e$ is the angle between the neutrino and recoil electron directions. This two-to-one backward-forward asymmetry with respect to the Sun's direction can be used to separate the CC signal from the other signals discussed below.

Neutral-Current reaction

The neutral-current (NC) reaction

$$\nu_x + d \longrightarrow p + n + \nu_x, \tag{3.3}$$

also occurs and is particularly interesting because it is equally sensitive to all active neutrino flavors. The threshold for this reaction is given by the deuteron binding energy, 2.225 MeV. The total cross-section as calculated by Kubodera and Nozawa [41], and Ying, Haxton, and Henley [42], is shown in Figure 3.3. Kubodera and Nozawa report a 5 % uncertainty for this reaction as well. However,

Figure 3.1: The CC cross-section as calculated by Kubodera and Nozawa (KN), Ying, Haxton, and Henley (YHH), and Ellis and Bahcall (EB). Taken from [44].

Figure 3.2: The differential CC cross-sections as calculated by Kubodera and Nozawa (KN), and Ellis and Bahcall (EB). Taken from [44].

they also report that there is only a 1 % uncertainty in the ratio of the CC to NC cross-sections. For the neutral-current, detection is via the neutron released and only the neutrinos above the 2.225 MeV threshold are measured. There is no additional energy information.

Figure 3.3: The NC cross-section as calculated by Kubodera and Nozawa (KN), and Ying, Haxton, and Henley (YHH). Taken from [44].

Elastic scattering reaction

The third reaction is the neutrino-electron scattering (ES) reaction

$$\nu_x + e^- \longrightarrow \nu_x + e^- \tag{3.4}$$

where ν_x can be any flavor of neutrino. Because the interaction with ν_e's can be mediated by $W^\pm$ bosons in addition to the Z^o, the cross-section for ν_e interaction is six times higher than for ν_μ and

ν_τ. The overall cross-section is much lower than that of the CC interaction, and even though there are five times more target electrons than deuterons, the expected rates are one tenth that of the CC rates. However, the scattered electron which is used for detection is highly correlated with the incoming neutrino direction and this can be used to separate these events from those of the other reactions.

3.1.2 The detection mechanisms

In SNO, as in all other neutrino experiments, it is the end-products of the neutrino reactions that are detected. In what follows, the two different detection techniques in SNO, Čerenkov light detection and direct neutron detection, are described. This thesis mainly deals with Čerenkov detection and therefore its discussion is emphasized.

Čerenkov light production and the SNO photo-array

Neutrinos can be detected in SNO via Čerenkov photons radiated by electrons moving faster than the speed of light in the D_2O medium. For the CC and ES reactions, the relativistic electron resulting from the reaction produces the Čerenkov light. For the NC reaction, light production is the result of electrons from Compton scattering of γ-rays following neutron capture. In pure D_2O, the neutrons can be captured on deuterium nuclei resulting in the release of 6.25 MeV γ-rays. The capture efficiency for neutrons in D_2O is only 24 % [46]. If 2.5 tonnes of salt ($MgCl_2$) is added to the D_2O, the neutron can be captured on ^{35}Cl resulting in a 8.6 MeV γ-ray with a 83 % capture efficiency [46].

The photons from Čerenkov radiation are emitted in a cone with a half-opening angle with respect to the electron trajectory given by

$$\cos\theta_C = \frac{1}{\beta n} \tag{3.5}$$

where β = v/c and n is the index of refraction of the medium. In the ultra-relativistic limit, v=c, and therefore $\theta_C = 41$ degrees in heavy water for which n=1.337. The number and spectrum of Čerenkov photons produced as a function of the radiating electron's path length, x, and photon wavelength, λ, is given by

$$\frac{d^2N}{dxd\lambda} = 2\pi\alpha\left(1 - \frac{1}{n^2\beta^2}\right)\frac{1}{\lambda^2} \tag{3.6}$$

where α is the fine structure constant. The integral over wavelengths can be expressed

$$\frac{dN}{dx} = 2\pi\alpha\sin^2\theta_C\int_{\lambda_1}^{\lambda_2}\frac{d\lambda}{\lambda^2}. \tag{3.7}$$

This value is roughly constant down to the Čerenkov kinetic energy threshold of 262 keV in D_2O and corresponds to ≈358 photons per cm for the spectral range in which SNO is sensitive (λ = 300 nm to 650 nm) [46]. The electron path length is approximately 0.45 cm per MeV so ≈ 1600 detectable photons are expected for a 10 MeV electron [46].

Because of multiple electron scattering and, in the case of gamma-rays, multiple pair production and Compton scattering processes, there should be considerable variation in the light output. For the same reasons, the angular distribution of photons with respect to the initial particle trajectory is not a simple delta function at $\theta = \theta_C$. The distributions are therefore simulated using the SNO Monte Carlo which is described in section 3.2 [47]. The distributions of the number of photons produced and their angular distributions for 10000 10 MeV (kinetic) electrons and γ-rays are shown in Figures 3.4 and 3.5. In both instances the wavelengths span from 200 nm to 720 nm and therefore many of the photons produced are outside the detectable range. It is evident from these figures that the statistical fluctuations in the number of photons produced are significant and this ultimately limits the detector resolution. The photon yield for γ-rays is lower because of multiple Compton scattering. Some of the Compton scattering products can become lower than the Čerenkov threshold.

In SNO, the detection of the Čerenkov photons is with an array of 9546 phototubes which surround the D_2O target volume. The D_2O is contained within a large spherical acrylic vessel. A cross sectional view of the detector is shown in Figure 3.6 and a detailed description of its components given in section 3.2. The number of phototubes hit in an event, NHIT, is proportional

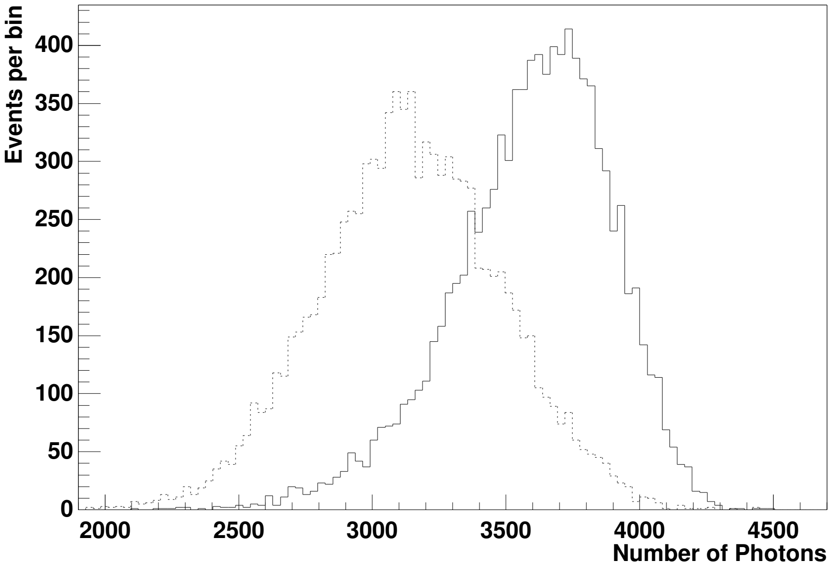

Figure 3.4: Photon production for 10 MeV electrons (solid line) and gamma-rays (dotted-line). The distributions were generated with the SNO Monte Carlo for Čerenkov light wavelengths between 200 and 720 nm.

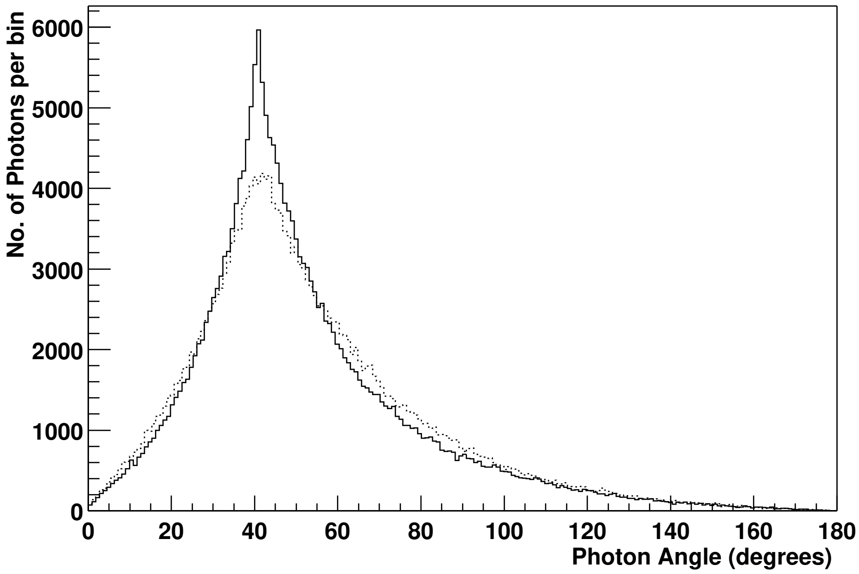

Figure 3.5: Angular distribution of photons for 10 MeV electrons (solid line) and gamma-rays (dotted line). The angle is taken with respect to the initial particle track direction. Calculated with the SNO Monte Carlo.

to the number of Čerenkov photons produced and can therefore be used as an energy estimator. The pattern of hit phototubes and their relative timing can be used to reconstruct the event position and direction. This information can be used to separate the various neutrino signals and backgrounds. Figure 3.7 shows the phototube hit pattern for a candidate neutrino event. More detailed discussions of the event energy determination and reconstruction are given in subsequent chapters.

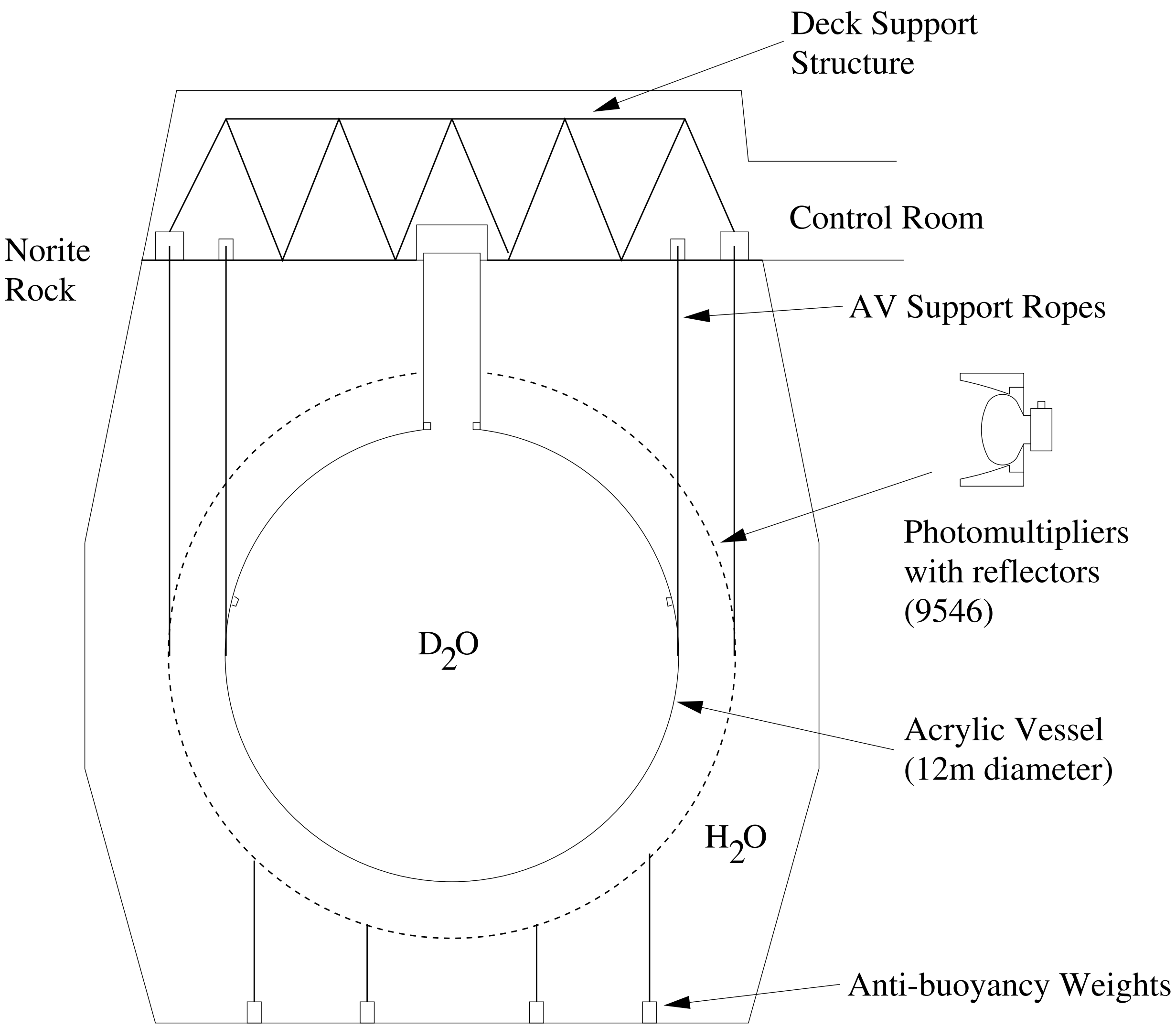

Figure 3.6: Cross sectional view of the SNO detector.

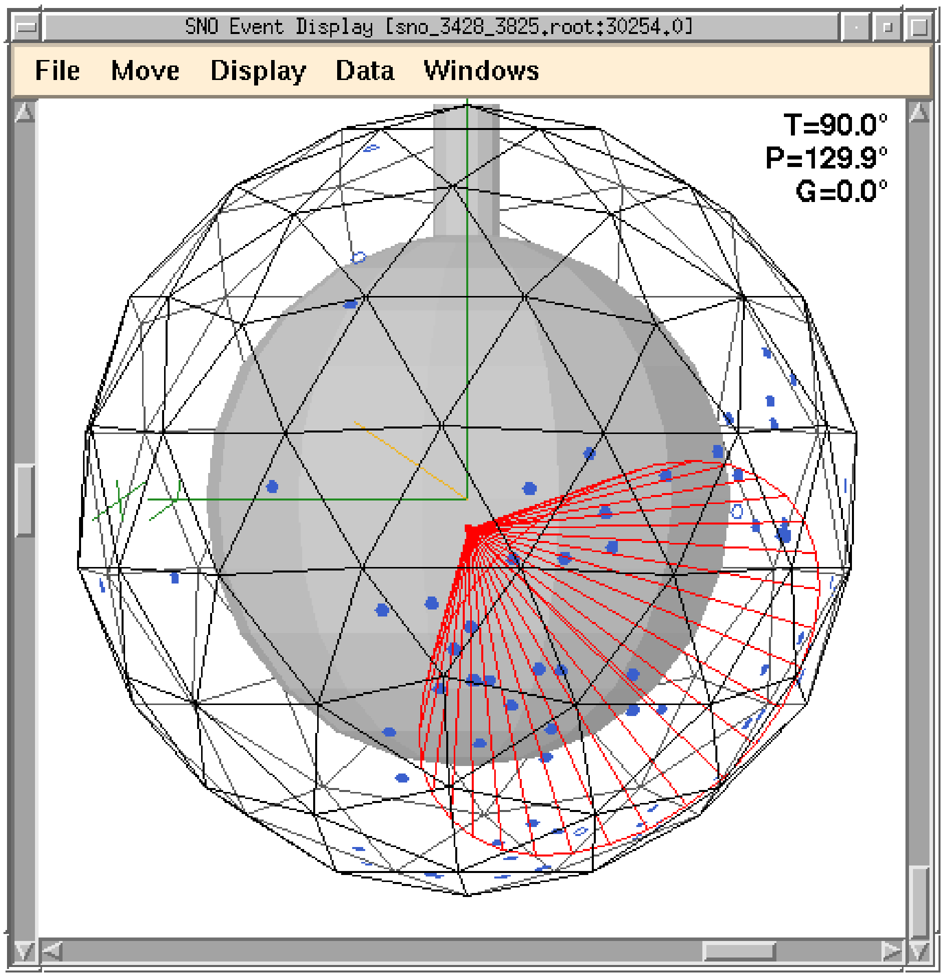

Figure 3.7: A candidate neutrino event as viewed with the SNO event display, XSNOED [48]. Shown are the 71 phototube hit locations on the SNO photoarray along with a fit to the Čerenkov cone.

The SNO Neutral-Current detector array

SNO is currently operating solely as a pure D_2O Čerenkov detector and is therefore most sensitive to the CC reaction. In the near future, however, NC detection will be enhanced using two techniques. These techniques will involve adding salt into the D_2O volume or introducing an array of neutron detectors. The introduction of $MgCl_2$ salt enhances the light output from neutron capture as the neutrons capture on Cl producing γ's with energies up to 8.6 MeV. In the other technique, the neutrons produced in the NC reaction will be detected with strings of ^{3}He-filled proportional counters (NCDs). Detection of the neutrons, which are thermalized in the D_2O, will be via the reaction

$$^3He + n \longrightarrow p +^3 H + 764\ keV \tag{3.8}$$

whose cross-section is 5330 barns. A detailed description of the proposed NCD array can be found in [49].

3.1.3 Backgrounds

The energy thresholds for the three neutrino interactions are either low, or in the case of the ES interaction, null. The effective threshold is therefore determined by the detector backgrounds.

The bulk of the background contribution due to cosmic ray muons is effectively eliminated by virtue of the detector's depth underground which is over two kilometers. The remaining muons that do penetrate are easily distinguished. However, after a muon event occurs, other events must be gated out for several seconds to avoid spallation products which mimic the ^{8}B spectrum events.

The remaining backgrounds come from gamma-rays from the surrounding rock and β's and γ's from radioactive isotopes, mostly from the uranium and thorium chains, in the detector materials. These can produce Čerenkov events in the energy range of solar neutrinos. The rock-wall gamma-ray contribution is minimized by the approximately 7800 tonne light water volume in which the entire detector is immersed. The impact of this background must nonetheless be understood because its contribution would be above the low energy threshold for neutrino detection. The backgrounds due to the decay of elements in the uranium and thorium chain are overwhelming in the lower energy range and will likely impose a $\approx$ 5 MeV electron energy threshold for neutrino detection. Great effort has gone into minimizing this contribution by choosing low radioactivity construction materials. An additional background for the NC reaction is that due to photo-disintegration of deuterium by gamma-rays above 2.223 MeV. The neutrons released are indistinguishable from those produced in the NC reaction. The main source of γ's producing photodisintegration are ^{208}Tl (2.615 MeV γ) and ^{214}Bi (2.445 γ) from the thorium and uranium chains, respectively. In all instances, a thorough understanding of the detector backgrounds is required.

3.2 General description of the detector

The SNO detector (see Figure 3.6) is located in a 34 meter high by 22 meter diameter barrel-shaped cavity located two kilometers underground in INCO's Creighton mine near Sudbury, Canada [46]. Figure 3.8 shows the layout of the observatory. Surrounding the cavity are a control room, a water storage and purification room, and various other utility rooms. The entire lab is maintained under clean room conditions and all construction materials were chosen for their radiopurity. The cavity is divided by a deck placed 27 meters above the cavity floor. The upper deck contains the SNO electronics, calibration hardware, and piping which feeds water from the water purification plant to the cavity. The detector is located below deck and consists of 1000 tonnes of isotopically pure D_2O provided by AECL with the cooperation of Ontario Hydro. The entire cavity below deck is lined with polyurethane permitting it to be filled with the $\approx$ 7800 tonnes of ultra-pure light water used to shield the detector. The liner also acts as an effective barrier to ^{222}Rn, a highly mobile U chain element, and hence an important background. In what follows, the main features of the detector including the water volumes, the acrylic vessel, the PMTs and their support structure, the electronics, and the data reduction, analysis, and Monte Carlo packages are discussed. A more detailed description of all systems will be available in an upcoming SNO collaboration instrumentation paper [50]. A description of detector calibration is given in chapter 4.

Figure 3.8: Layout of the SNO laboratory. Figure taken from [50].

3.2.1 The heavy and light water volumes and the acrylic vessel

The bulk of the detector volume consists of the target D_2O, the shielding H_2O, and a cover gas above these volumes. There is also the approximately 30 tonne acrylic vessel that contains the D_2O. For all of these components, radiopurity and cleanliness are crucial. Also the water and acrylic must be as transparent as possible to minimize the event energy dependence on position within the detector due to attenuation of the Čerenkov light.

The SNO light water systems were designed to provide SNO with ultra-clean (radiopure, biology free, and optically transparent) water. Light water is supplied by the mine surface purification plant and sent down to the lab via several kilometers of piping. A schematic showing the main features of the underground light water purification systems is shown in Figure 3.9. Before entering the lab, the water is de-aerated and passed though a multimedia filter consisting of a bed of sand and charcoal to remove large particles and a 10 micron filter to remove finer particles. The water then enters the laboratory water utility room where it passes through a charcoal filter, is softened, then sent to a reverse osmosis unit. Following the reverse osmosis unit, the water is recirculated into the SNO cavity through ion exchange columns, 1 micron filters, UV sterilizers, a custom process degasser for removing dissolved gases such as O_2, N_2, and Rn, and a chiller for maintaining the water at 10 degrees Celsius. A ten tonne tank is also included in the loop and maintains the water level in the cavity.

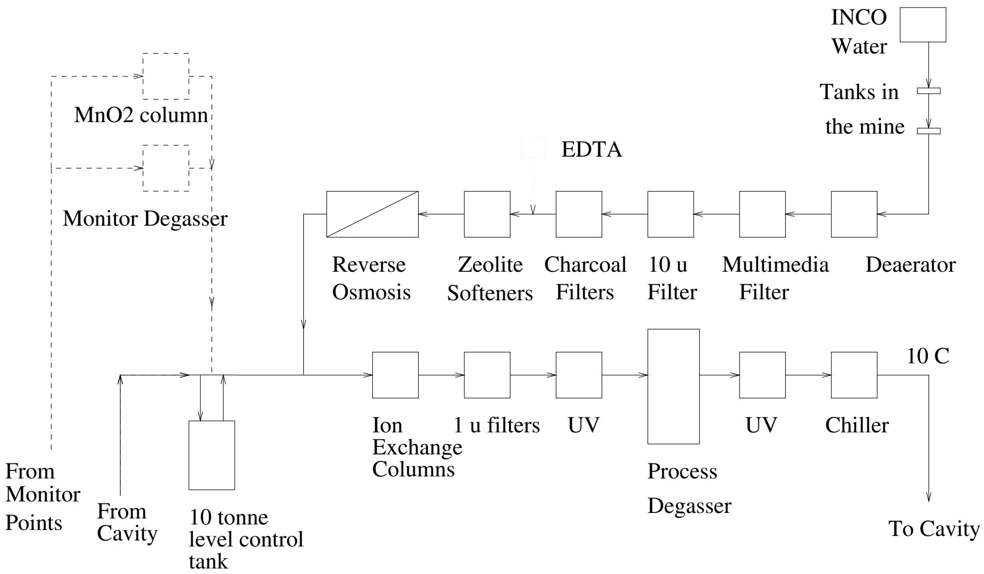

Figure 3.9: The SNO light water systems. Figure taken from [50].

The D_2O systems, like the H_2O systems, were designed to provide SNO with ultra-clean water, but also a means for introducing and removing ultra-clean salt for NC detection. A schematic of the heavy water systems is shown in Figure 3.10. The D_2O is supplied by the Ontario Hydro Bruce heavy water plant and is shipped underground in specially designed rail cars. In the water utility room, the heavy water is passed through ion exchange columns, filters coated with DTiO, tight 0.03 micron filters and ultra-filtration units. After the SNO detector was filled with D_2O, the heavy water was recirculated through a reverse osmosis system, absorption columns and additional ultra-filtration units. Introduction of $MgCl_2$ will be with a purified D_2O brine solution that will slowly be added into the SNO D_2O volume. Later desalination will be done with two dedicated reverse osmosis systems.

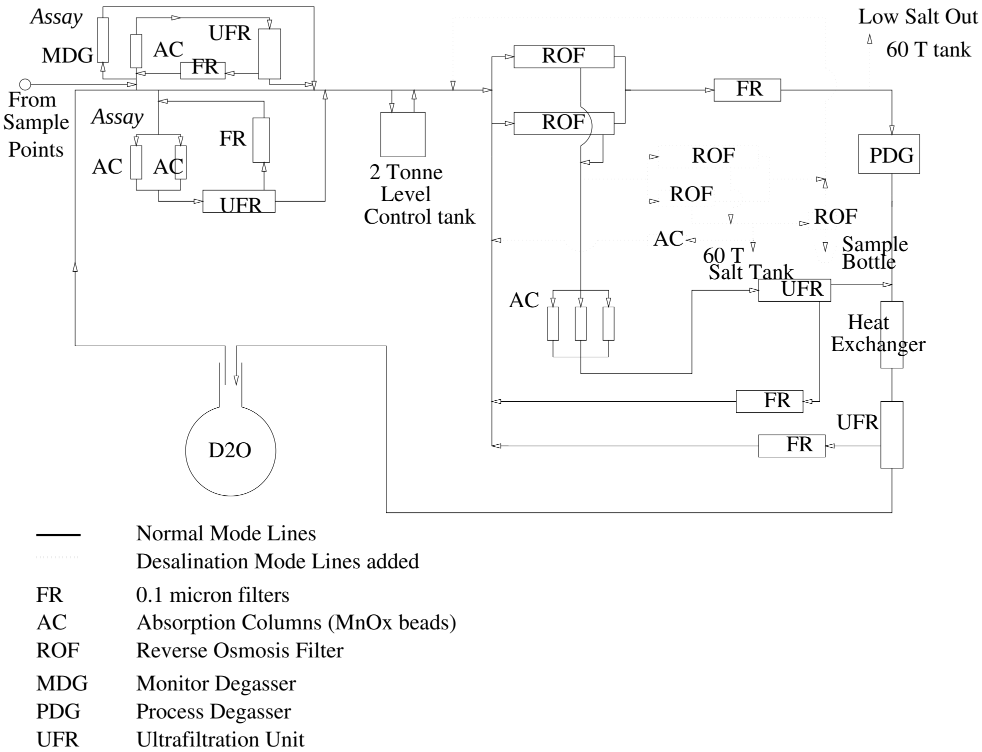

Figure 3.10: The SNO heavy water systems. Figure taken from [50].

Both the light and heavy water volumes will be routinely monitored for U and Th levels. The radiopurity of these volumes must be such that the neutron production rates due to photodisintegration do not exceed one-tenth that of the SSM NC production rate ($\approx$ 1 per day). This corresponds to $3\text{x}10^{-15}$ g/g Th and $4.5\text{x}10^{-14}$ g/g U concentrations in the D_2O. Techniques to assess these levels, and hence the photodisintegration background, were developed. Most of the assay techniques remove medium-lived (days) parent isotopes in the chains via ion-exchange and subsequently count their decay. Th, Ra, and Pb can be extracted with filters coated with DTiO [51] and Ra with MnO_x [52]. The Th, Ra, and Pb are stripped off the DTiO filters and counted in a scintillation cocktail. The Ra from MnO_x decays to Rn, which subsequently decays to Po, which is electrostatically precipitated onto a Si photodiode for detection. ^{222}Rn in the H_2O and D_2O is studied using a vacuum degassing technique [53] which removes the Rn from sampled SNO water. The Rn is trapped cryogenically then transferred to an activated ZnS coated scintillation cell for counting [54].

The D_2O containment vessel (see Figure 3.11) was designed to hold the nearly kilotonne volume of heavy water and was required to be radiopure and transparent to ultra-violet light. It is spherical and consists of 122 acrylic panels that were transported underground then bonded in situ. Most of the panels are approximately 5.5 cm thick. The equatorial panels have an approximately 11.4 cm thickness and have grooves for support ropes connected to the deck. The acrylic vessel also has a 1.5 meter diameter, 8 meter high chimney made of 5 additional cylindrical segments. The chimney permits the insertion of calibration devices and the D_2O piping from the water utility room. The sphere is made of ultraviolet-transmitting (UVT) acrylic panels for maximal transmittance of light, and the neck of ultraviolet absorbing (UVA) acrylic to prevent it from acting like a light guide.

With the acrylic vessel and cavity filled to their maximum levels, the cavity below the deck is sealed and filled with a pure nitrogen cover gas from liquid nitrogen boil off to minimize radon infiltration from the upper deck. The radon concentration above deck is 3 pCi/l (1 Ci = $3.7\text{x}10^{10}$ disintegrations per second) of mine air. Below deck the concentration is designed to be 10^{-5} pCi/l of cover gas.

3.2.2 The photomultiplier tube array

The requirements for the SNO phototubes are low noise, high efficiency for single photoelectron detection, and a small transit time spread for the electrons produced at the photocathode. All of these contribute to the energy resolution of the detector and its ability to do event reconstruction.

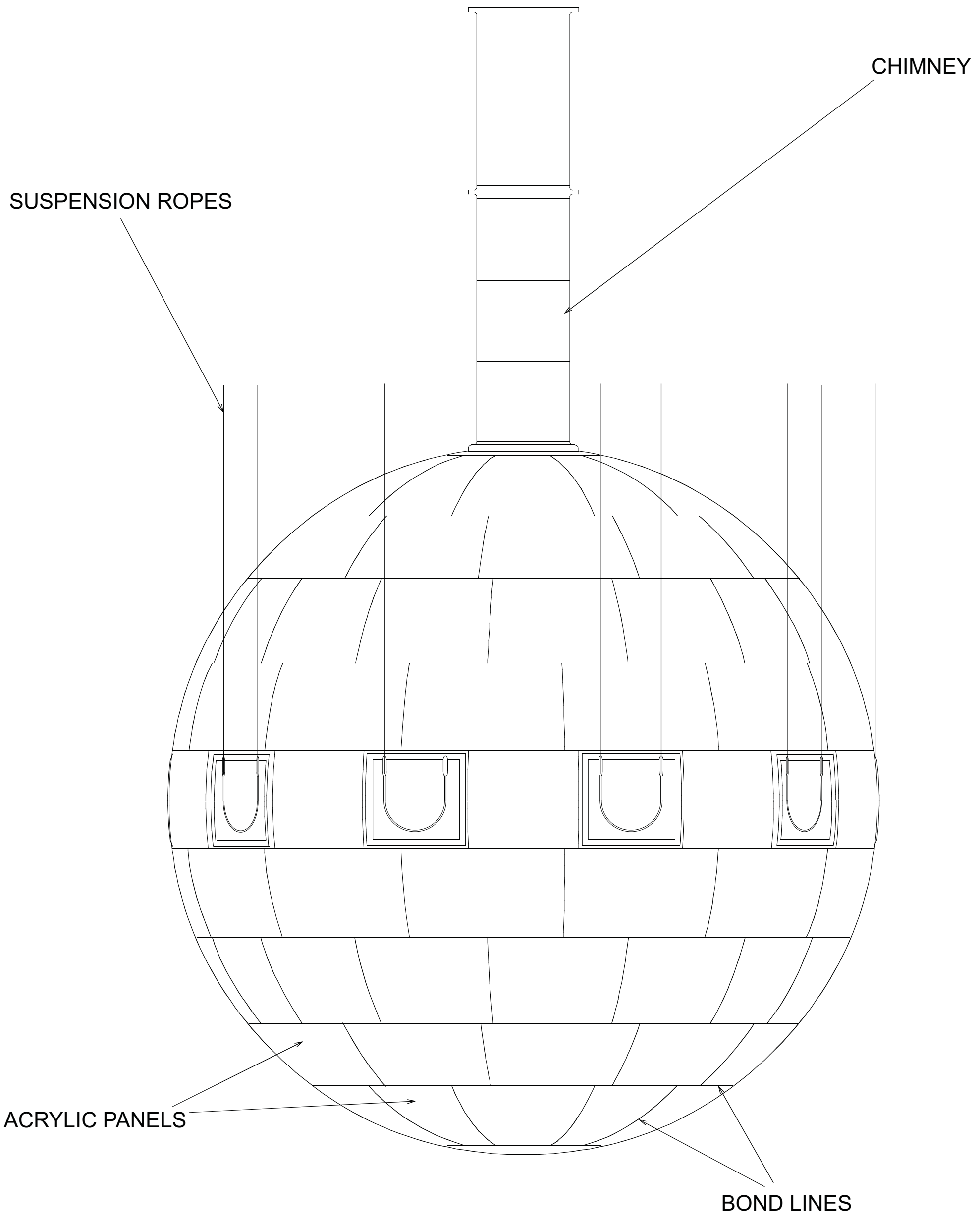

Figure 3.11: The acrylic vessel. Figure taken from [50].

In addition the phototubes must be low in radioactivity (K, U, and Th). SNO uses the mushroom-shaped Hamamatsu R1408 photomultiplier tubes which have a 20.4 cm diameter (see Figure 3.12). The R1408 has a venetian-blind dynode structure and is operated at positive high voltage in the 1700 to 2400 Volt range. The 9546 PMTs provide a total photocathode coverage of about 31 % of 4π. The 28 cm diameter light concentrators mounted on each phototube increase the coverage to about 64 % of 4 π. The light concentrators are made of thin dielectric-coated aluminum sheets. An additional 91 tubes are outward facing and are used to veto the few remaining cosmic ray muons.

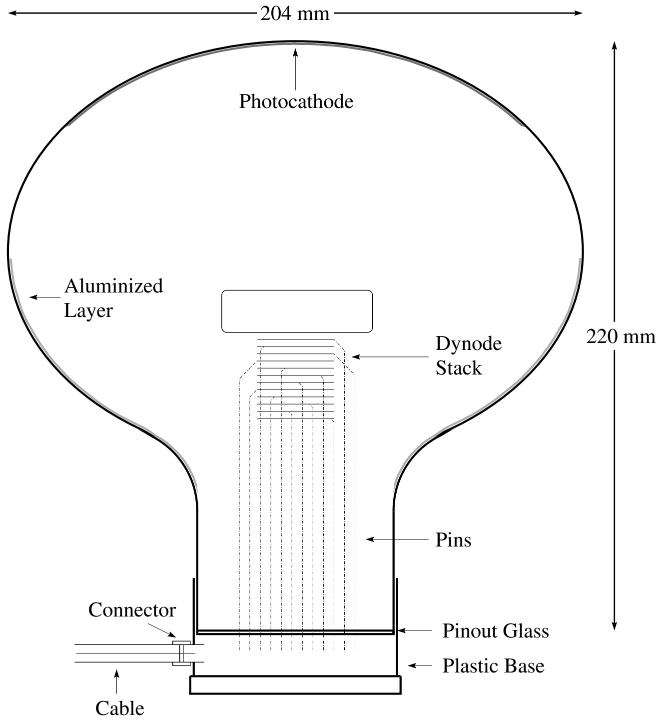

Figure 3.12: The SNO phototube. Figure taken from [55].

The phototubes and their concentrators, and the outward looking tubes, are mounted on a PMT Support Structure or PSUP. The PSUP was designed primarily to optimize the overall geometrical efficiency. It also acts as a partial barrier to enable H_2O flow from the inner H_2O volume between the acrylic vessel and the PSUP to the outer cavity volume. The skeleton of the PSUP consists of a geodesic structure constructed out of 92 nodes and 270 struts made of various stainless steel alloys. Mounted on the geodesic structure are 751 hexagonal ABS plastic housings which hold between 7 and 21 PMTs each. The PMTs are situated on average about 2.5 meters away from the acrylic vessel.

Each PMT base is mounted in a waterproof enclosure which interfaces to 32 meter long, 75 Ω, RG59/U type cables which penetrate up through to the upper deck electronics. Horizontal coils are placed around the cavity to cancel out the vertical component of the Earth's magnetic field and hence improve the tube gain by about 10 % on average.

3.2.3 Electronics, trigger, and data acquisition systems

The electronics and trigger systems must be able to identify events of interest (i.e neutrinos from the Sun and supernovae, calibration source events, etc), and for each event record the universal time of the event and number of phototubes that fire, along with the individual PMT timing and charge information. The systems must be able to do this at high rates (for supernovae) with nearly zero deadtime. The events must then be written to tape for subsequent analysis. Detailed descriptions of the electronics, trigger, and data acquisition systems are given in [56].

An overview of the SNO electronics, trigger, and data acquisition systems is shown in Figure 3.13. The electronics are organized into 19 crates which can handle up to 512 PMTs each. Each PMT cable is connected to the back of the crate to one of 16 PMT interface cards (PMTICs) which supply the high voltage and interfaces to 16 front end cards (FECs). Each FEC has four daughter boards (DB), each processing 8 channels. Each DB contains discriminator chips, integrator chips, and CMOS chips which are used to provide analog memory, time-to-amplitude converters, and channel and trigger logic for the detector. The FECs are attached to a custom backplane("SNOBus") which distributes power and signals. Attached to the backplane are a translator card and a trigger formation card. The translator card communicates with a similar card in the DAQ VME crate. The trigger card sums the individual channel triggers and sends the sum to the Master Trigger Card (MTC).

The MTC uses the number of phototube hits, NHIT, as its primary event trigger. The counting

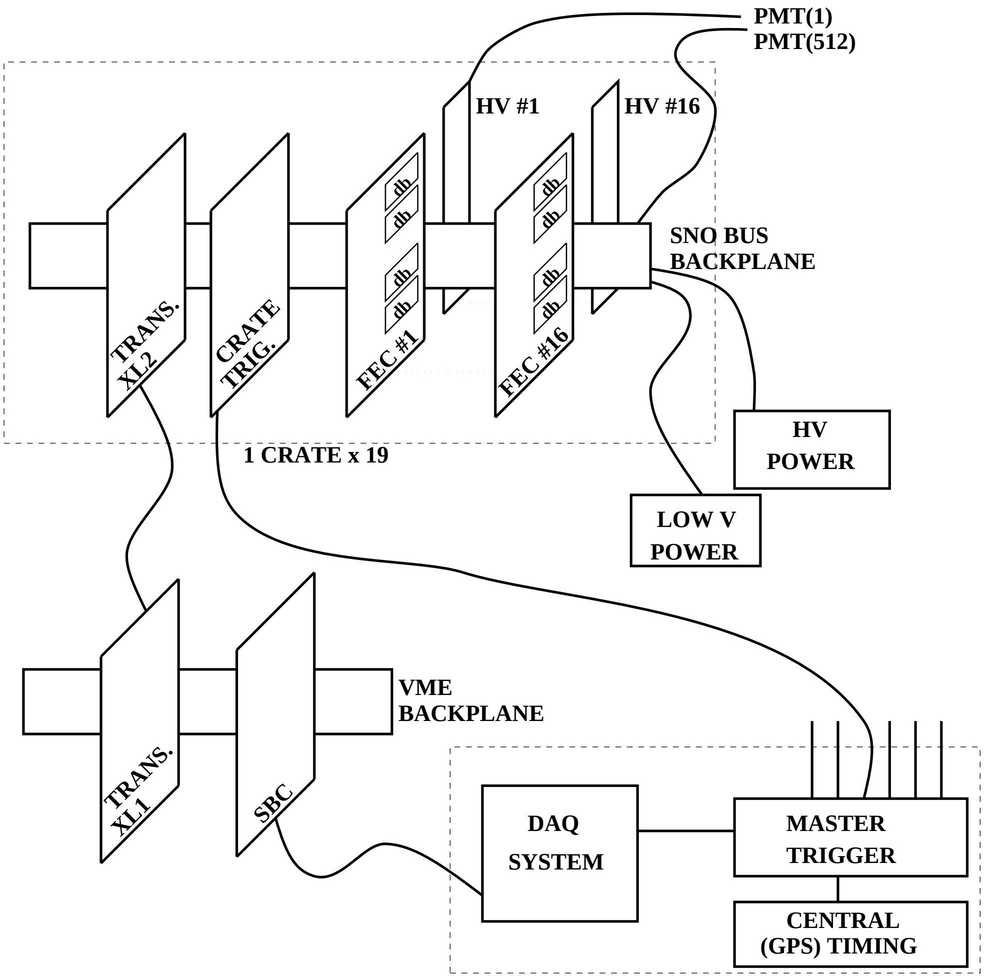

Figure 3.13: The SNO electronics and data acquisition systems. Figure taken from [50].

of hits is done by analogue summing of signals from the SNO CMOS chips. If the sum is above a programmable threshold, a global trigger (GT) is set. The nominal setting for the trigger time window is 100 nanoseconds which is slightly longer than the transit time of light across the detector (66 nanoseconds). A short time window (20 nanosecond) trigger, a summed charge trigger (ESUM), and a programmable trigger (Pulse GT) are also available along with special triggers for calibration devices. The MTC is connected to a commercial Global Positioning System (GPS) which synchronizes a 10 MHz universal clock. This timing permits 100 nanosecond time resolution and can be used for correlating the observation of astrophysical events (i.e supernovae) with that from other experiments such as SuperKamiokande. A 50 MHz quartz oscillator is used as well and gives a finer resolution (20 nanoseconds) for inter-event timing.

The data acquisition system was designed to read out the contents of the FEC memory and the Master Trigger Card, and sort the associated hit tube information with events. The built events are then written to disk and tape and routinely shipped via ethernet to the surface where they are written to disk as well. Some fraction of the events (depending on the rates) can be sent via internet to other computers for online analysis and event display. The heart of the data acquisition system consists of a single VME crate containing a Motorola 68040 single-board computer (SBC), a PCIbus-VME interface card, an SBus-VME interface card, the Master Trigger Card, and seven XL1 cards. The SBC or eCPU (embedded CPU) reads out sequentially the FECs in each crate. Communication between the SBC and the crates is via the XL1 cards. It also has access to memory in the MTC. This information is transferred to a Sun Ultra Sparc 1/170 workstation via the SBus-VME Interface. The Sun sorts the FEC and MTC data, builds the events, and writes the events (in ZEBRA format [57]) to disk and tape. Control of the DAQ is via the user interface program SHARC (SNO Hardware Acquisition and Readout Control) which runs on a Power Computer 250 MHz PPC Macintosh and communicates to the SBC via the PSIbus-VME interface.

3.2.4 Data reduction, analysis, and Monte Carlo

SNO combines its off-line data analysis and event simulation software into one package called the SNO Monte Carlo and ANalysis code, or SNOMAN [47]. The SNOMAN data analysis must take data written and packed to tape, unpack it and apply calibrations to the data. Calibrations include, for example, corrections for PMT charge pedestals or application of PMT time-offsets. The Monte Carlo code must simulate Čerenkov photon production in the detector, their propagation, and their detection with the photo-array. It must also permit identical treatment of the higher order analysis for both Monte Carlo and real data.

SNOMAN is primarily written in FORTRAN, having several independent processors acting on a central ZEBRA-based data structure. Examples of processors include Monte Carlo, calibration, and analysis processors. The calibration constants and detector status information used are stored in ZEBRA format and are stored in the SNO database (SNODB). Parts of the Monte Carlo are based on already established software packages. This includes EGS4 [58] used for propagation of electrons, MCNP [59] for neutrons, and GEANT [60] for muons. Simulation of solar neutrinos and oscillations is based on code written by Hata [61]. The photon propagation code was written by SNO collaboration members and includes attenuation, refraction, reflection, and Rayleigh scattering. This requires a detailed modeling of the detector geometry. For example, the details of the acrylic vessel include belly plates, bond joints, the neck, the rope grooves, and support ropes. Detailed PSUP, PMT, and reflector geometries are included as well. Much of the higher order analysis can be done within SNOMAN with special processors. The SNOMAN data structure can, however, be output to CERNLIB HBOOK files for subsequent analysis with the PAW analysis package [62]. Similarly the data can be analyzed with the ROOT analysis package [63].

Table 3.1: Monte Carlo event rates for a 5 MeV threshold (NHIT ≈ 43) and a 600 cm radial fiducial cut for SSM, non-adiabatic (NA), large angle (LA), vacuum (VAC), and sterile (ST) oscillation solutions.

	SSM	NA	LA	VAC	ST
CC	9850	3417	1794	3271	3515
NC	687	654	665	669	209
ES	1136	470	313	429	350
Total	11681	4541	2772	4369	4074

3.3 The first year data and analysis

The initial SNO operation is with pure D_2O. In this phase, the expected SSM neutrino spectrum in terms of NHIT as simulated by the Monte Carlo is shown in Figure 3.14 where only events which reconstructed within the 600 cm radius of the acrylic vessel are considered. For the SSM prediction, the CC flux will dominate. However, if there are oscillations, the CC flux will be depleted and the relative flux ratios will change. This is shown in Tables 3.1 and 3.2 which give the results for one year Monte Carlos for all three interactions for a 5 MeV and 7 MeV low energy threshold, respectively. Clearly within one year of pure D_2O running there will be enough statistical accuracy to extract meaningful physics. Oscillation searches and constraining the $\sin^2 2\theta$ and Δm^2 solution space, however, will require a sophisticated analysis which will include as complete a knowledge as possible of the physics and detection processes involved. The details of how the final analysis will be done are still being developed by the SNO collaboration. The following discusses one possible approach.

Because it is not possible to separate completely the CC, NC, ES, and background "signals" on an event by event basis, the analysis must include the entire dataset above the chosen low energy threshold. The distinguishing features of each signal will be used to determine their contribution to the data-set. First, the energy spectra of the reactions will be different. The CC and ES reactions

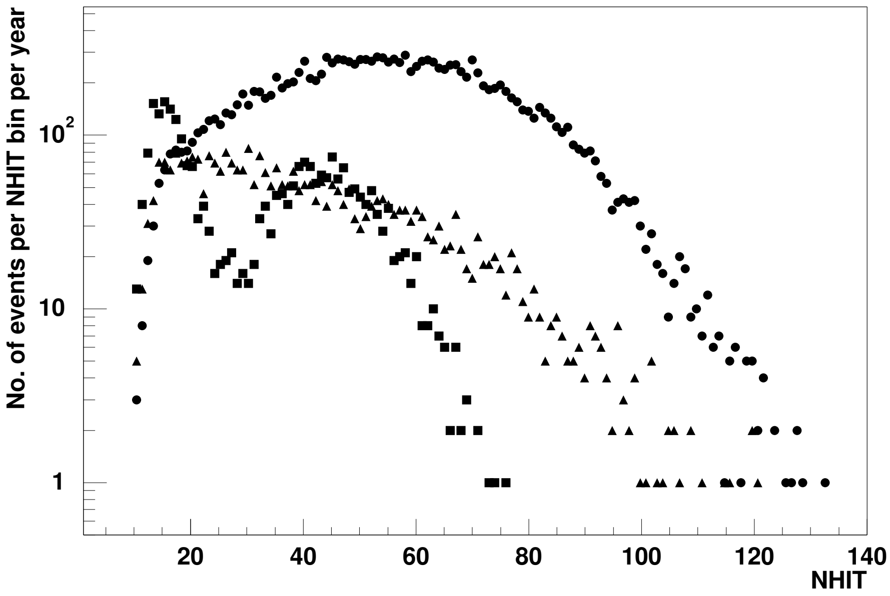

Figure 3.14: The SNO SSM neutrino NHIT spectra. Shown are the Monte Carlo CC (circles), NC (squares), and ES (triangles) reaction NHIT spectra for one year of data taking in pure D_2O. The bimodal distribution for the NC events are due to a significant fraction of the NC events near the acrylic vessel capturing on Hydrogen producing 2.2 MeV gammas rather than 6.25 MeV gammas.

Table 3.2: Monte Carlo event rates for a 7 MeV threshold (NHIT $\approx$ 60) and a 600 cm radial fiducial cut for SSM, non-adiabatic (NA), large angle (LA), vacuum (VAC), and sterile (ST) oscillation solutions.

	SSM	NA	LA	VAC	ST
CC	5944	2162	1105	2357	2263
NC	68	76	59	70	26
ES	565	242	164	246	188
Total	6577	2480	1328	2674	2477

result in relativistic electrons from interactions of ^{8}B or hep neutrinos. The energy that the neutrino imparts to the electron is different for these two interactions and is given by the differential cross-sections. In pure D_2O, the NC energy spectrum will be that of 6.25 MeV gamma-rays from the (n,γ) reaction on deuterium. The background energy spectrum will also include 6.25 MeV γ's from the neutron released by the photodisintegration of deuterium, but will also include Čerenkov light from other β and γ radioactivity. In addition to energy dependences, there are angular dependences with respect to the direction from the Sun. The ES reaction electron is strongly forward peaked, whereas that of the CC reaction has a two-to-one backward-to-forward asymmetry. The γ emission from the NC neutrino reaction should be isotropic but the background signals could have angle dependences with respect to the detector itself. There will also be radial dependences. For example, the NC events will have a radial dependence because neutrons produced near the acrylic vessel are more likely to capture on Hydrogen producing a 2.2 MeV gamma rather than the 6.25 MeV γ from neutron capture on deuterium. Backgrounds will also likely have a radial dependence.

To take all of these dependences into account a measure of the effective electron energy, E_{SNO}, the angle with respect to the Sun, $\cos\theta_{SNO}$, and radial position, X_{SNO}, would be determined for each event. The full data set would then be subdivided into cells each covering a range of energies, angles with respect to the Sun, and radial positions. Further sub-division of the data, for example into DAY and NIGHT, could be implemented as well. Analysis would then be performed by minimizing a chi-square function of the form.

$$\chi^2 = \sum_{E_{SNO_i}} \sum_{\cos\theta_{SNO_j}} \sum_{X_{SNO_k}} \left(\frac{F_{ijk}^{DATA} - F_{ijk}^{THEO}}{\sigma_{ijk}} \right)^2 \tag{3.9}$$

where F_{ijk}^{DATA} would be the number of events in each cell determined from experiment, and F_{ijk}^{THEO} would be the theoretical prediction which would include survival probabilities for various $\sin^2 2\theta$ and Δm^2 values. The σ_{ijk} would represent the theoretical and experimental (statistical and systematic) errors. Theoretical errors would include the uncertainty in the ^{8}B energy spectrum and the CC, ES, and NC cross-sections. The experimental errors would include the uncertainty in the energy scale and resolution, the event position and direction reconstruction uncertainties, etc. Some of the errors will also be correlated and this must be taken into account in the χ^2 analysis.

The theoretical values, F_{ijk}^{THEO}, would be determined with the SNOMAN Monte Carlo which includes the full knowledge of the detector response. The effective electron energy, E_{SNO}, used for both F_{ijk}^{DATA} and F_{ijk}^{THEO} would be parameterized simply by the number of PMT's hit in the event, NHIT, or could be a more complex parameter including energy calibration information and compensating for optical attenuations at the event location.

To discuss the main features of F_{ijk}^{THEO}, however, this differential response can be presented in terms of simple, approximate, analytic expressions. F_{ijk}^{THEO} can then be expressed as follows,

$$F_{ijk}^{THEO}\Delta_{ijk} = \left[\int\int\int \left(F_{ijk}^{CC} + F_{ijk}^{ES} + F_{ijk}^{NC} + F_{ijk}^{Bkg}\right) dx dE d\cos\theta\right]\Delta_{ijk} \tag{3.10}$$

where x, E, $\cos\theta$, are the true positions, energies, and solar angles of the particles detected, and Δ_{ijk} represents the ranges of X_{SNO}, $\cos\theta_{SNO}$, and E_{SNO} in the calculation. The terms F_{ijk}^{CC}, F_{ijk}^{ES}, F_{ijk}^{NC}, and F_{ijk}^{Bkg}, represent the neutrino signals and backgrounds. F^{CC} is the charged-current contribution and is given by

$$F_{ijk}^{CC} = f^{CC}\cdot R_{ijk}^{E,e}(E, E_{SNO})\cdot R_{ijk}^{\theta,e}(\cos\theta, \cos\theta_{SNO})\cdot R_{ijk}^{x,e}(x, X_{SNO})\cdot \epsilon_{ijk}^{CC}(E, x, \cos\theta) \tag{3.11}$$

with

$$f^{CC} = \int_0^{E_{\nu max}} P(E_\nu, \Delta m^2, \sin^2 2\theta)\frac{d\sigma_{CC}^{\nu_e}(E_\nu, E, \cos\theta)}{dE d\cos\theta}\lambda(E_\nu)dE_\nu. \tag{3.12}$$

In this last expression, $P(E_\nu, \Delta m^2, \sin^2 2\theta)$ is the calculated survival probability for neutrino oscillations,

$$\frac{d\sigma_{CC}^{\nu_e}(E_\nu, E, \cos\theta)}{dE d\cos\theta} \tag{3.13}$$

is the differential cross-section for the product electron energy and direction, and $\lambda(E_\nu)$, is the combined ^{8}B and hep neutrino energy spectrum. In equation 3.11, $R^{E,e}$ is the energy response function which can be expressed approximately as a Gaussian distribution,

$$R^{E,e}(E, E_{SNO}) = \frac{1}{\sqrt{2\pi\sigma(E)}}\exp\left(\frac{-(E_{SNO} - E)^2}{2\sigma^2(E)}\right) \tag{3.14}$$

where $\sigma(E)$ is the resolution width. Similarly $R^{\theta,e}$ and $R^{x,e}$ are response functions for the event angles and positions, respectively. The superscript, e, indicates that the responses are for electrons. Finally, ϵ^{CC} is the detection efficiency for events of a given energy, position, and direction. This would include data reduction efficiencies.

Similarly an expression can be written for the elastic scattering interaction,

$$F_{ijk}^{ES} = f^{ES} \cdot R_{ijk}^{E,e}(E, E_{SNO}) \cdot R_{ijk}^{\theta,e}(\cos\theta, \cos\theta_{SNO}) \cdot R_{ijk}^{x,e}(x, X_{SNO}) \cdot \epsilon^{ES}(E, x, \cos\theta) \tag{3.15}$$

with

$$\begin{aligned} f^{ES} = & \int_0^{E_{\nu max}} P(E_\nu, \Delta m^2, \sin^2 2\theta) \frac{d\sigma_{ES}^{\nu_e}(E_\nu, E, \cos\theta)}{dE d\cos\theta} \lambda(E_\nu) dE_\nu \\ & + \int_0^{E_{\nu max}} (1 - P(E_\nu, \Delta m^2, \sin^2 2\theta)) \frac{d\sigma_{ES}^{\nu_\mu}(E_\nu, E, \cos\theta)}{dE d\cos\theta} \lambda(E_\nu) dE_\nu \end{aligned} \tag{3.16}$$

where $\sigma_{ES}^{\nu_e}$ and $\sigma_{ES}^{\nu_\mu}$ are the ES cross-sections for ν_e and ν_μ neutrinos, respectively. Because the CC and ES reactions both produce electrons, the response terms ($R^{E,e}$, $R^{\theta,e}$, $R^{x,e}$) and the efficiency term (ϵ^{ES}) in equation 3.15 are identical to those in equation 3.11.

For the neutral current reaction

$$F_{ijk}^{NC} = f^{NC} \cdot R_{ijk}^{E,\gamma}(E, E_{SNO}) \cdot R_{ijk}^{\theta,\gamma}(\cos\theta, \cos\theta_{SNO}) \cdot R_{ijk}^{x,\gamma}(x, X_{SNO}) \cdot \epsilon^{NC}(E, x) \tag{3.17}$$

with

$$f^{NC} = \int_0^{E_{\nu max}} \sigma_{NC}^{\nu_x}(E_\nu) \lambda(E_\nu) dE_\nu \tag{3.18}$$

where $\sigma_{NC}^{\nu_x}$ is the NC cross-section, and the superscript, γ, indicates that the response functions are for 6.25 MeV γ-rays. The term ϵ^{NC} takes into account the efficiency for neutron detection. Finally, the last term in equation 3.10, F^{Bkg}, will be constructed once the detector backgrounds are understood.

The above expressions can also be used to illustrate the separate calibration tasks required to determine the systematic uncertainties necessary for the neutrino analysis. The uncertainties associated with the energy scale and resolution would be determined by directly comparing the measured response to monoenergetic gamma-ray calibration sources, $R_{DATA}^{E,\gamma}$, to the Monte Carlo prediction, $R^{E,\gamma}_{MC}$. Uncertainties in the electron response, $R^{E,e}$, would be inferred from these calibration measurements. Measurements with γ-ray sources would also be used to infer uncertainties in the angular response, $R^{\theta,e}$. In the case of the position reconstruction response, $R^{x,e}$, electron sources would be used. Čerenkov light sources (γ-rays and electrons) will also be used to test the ϵ^{CC} (ϵ^{ES}) efficiency, and neutron sources, the ϵ^{NC} efficiency. Detailed discussions of the use of γ-rays for the above purposes are given in the chapters that follow.

Chapter 4

Detector Energy Response and Calibration

The last chapter ended with a discussion of the analysis of neutrino data. The experimental results will be compared directly to those of SNOMAN Monte Carlo simulations including physics effects such as neutrino oscillations. In order for such a scheme to work, the Monte Carlo simulations must accurately reproduce all aspects of the SNO detector response. In particular, the detector optical and energy response must be modeled correctly. This requires that various physical quantities, or constants, used to describe the detector properties in detail be measured with calibration devices. Certain constants, in particular those relating to the performance of the individual electronics channels and PMTs, are required for the experimental data analysis as well. Calibration of SNOMAN will include electronics, phototube, optical, and energy scale measurements. Once SNOMAN is fully parameterized, its performance must be checked. This will be done by comparing the Monte Carlo and experimental data as a function of energy, position, and direction for various calibration sources. This will permit a measure of any systematic uncertainty associated with the detector energy response, and hence any energy-dependent measurement in SNO. This would, for example, permit an estimate of the uncertainty in the low-energy threshold determination required for a ^{8}B neutrino flux analysis, as well as the uncertainties associated with a spectral analysis or any analysis similar to that presented in section 3.3. Finally, given an understanding of the detector response, the methods for assigning neutrino events a given position, direction, and energy must be considered along with any additional systematic they may introduce.

The above methods are described in this chapter, beginning with a short description of the various calibration devices used for these measurements. A short discussion of the phototube, electronics, and optical calibration is then given. A description of the absolute energy scale determination is given followed by the methods for determining the systematic uncertainties associated with the absolute energy calibration. A short discussion on event position and direction reconstruction algorithms is then given. Finally a discussion of the event analysis is given which includes a discussion of event energy determination.

4.1 Calibration devices and hardware

In addition to electronics pulsers for calibration, SNO has many devices that can be used for detector calibration. These include sources for optical calibration and for determining the detector response to γ's, β's, and neutrons. A short description of these sources is given below along with the methods for positioning the sources inside the detector volumes.

Optical sources

SNO has several optical sources for electronics, timing, and optical calibration. These sources must have short time pulse widths, span the Čerenkov wavelengths of interest, be triggerable, and in most cases provide isotropic light at varying intensities. The nitrogen/dye laser system [64, 65] uses the Laser Photonics Inc. LN203C laser which generates pulsed radiation at 337.1 nm up to a 45 Hz pulse rate. The laser can be used to pump dye lasers with wavelengths ranging from 360 to 700 nm. The laser is coupled via 35 meters of fiber-optic cable to a 10 cm diameter diffuser ball, or "laserball", which is used to emit nearly isotropic light. The pulse width of the emitted light is about 2 nsec and hence is well suited for timing and optical calibration. The use of neutral density filters permits several decades of light intensities for calibration. The laserball is the workhorse of the optical sources. There are, however, other sources which include a sonoluminescent bubble source which can be used to produce intense, short (< 0.1 nsec) pulses of light at ≈ 25 kHz rates. The short pulse width enables PMT timing calibration and the high rates enable tests of the SNO burst detection capabilities. SNO also has light-emitting diodes mounted at various locations on the PSUP which can be used for further tests.

Gamma-ray and beta-ray sources

Sources producing Čerenkov light are required for the absolute energy scale determination and the verification of the detector response. The sources are preferably triggered and mono-energetic and together must span the solar neutrino energy range. The decay of ^{16}N with a 7.13 second half life is used to produce 6.13 MeV (66.2 % branch) and 7.12 MeV (4.8 % branch) gamma-rays. The coincident beta accompanies each of the γ's and is used for triggering. A detailed description of this source is given in chapter 5. An activated NaI detector is used for a lower energy gamma source [66, 67]. The NaI will be activated at the Chalk River Laboratories reactor. The ^{24}Na produced has a 15 hour half-life permitting the necessary time to transfer the source to Sudbury. ^{24}Na beta-decays (Q = 5.5 MeV) to states which simultaneously emit 1.37 MeV and 2.75 MeV gamma-rays. The energy deposited in the NaI can be used to identify whether the 1.37 MeV γ, 2.75 MeV γ, or both γ's escape into the D_2O volume.

Higher energy gammas are provided using a miniature accelerator source that can be lowered into the detector volume [68]. Ions (H^+'s) are supplied by a cold Penning trap and then accelerated across a 20-30 kilovolt potential onto a tritium target producing 19.8 MeV gammas from the ^{3}H(p,γ)^{4}He reaction. This source is usually referred to as the (p,t) source. A beta spectrum source is provided from the decay of ^{8}Li which has a roughly 13 MeV endpoint and can be used as a further test of the energy scale, but also as a means to test position determination algorithms for electrons. The ^{8}Li source will be discussed in chapter 5 as well.

Neutron and background sources

Neutron sources are necessary for neutron capture efficiency determination and U and Th sources are required for studying the detector backgrounds. ^{252}Cf ($\tau_{1/2}$ = 2.64 years) has a 3.09 % fission branch and therefore can be used for neutron calibration. The ^{252}Cf can be encased in a plastic scintillator which can be used to tag the neutrons via the detection of scintillation light from the fission fragment betas and gammas. The decay of ^{17}N can also be used (see chapter 5) to produce neutrons where the coincident beta can be used as a tag. Sources to simulate radioactive backgrounds include U and Th chain elements encased in acrylic, and a proportional counter source in which ^{228}Th is deposited on the anode wire [69].

Source manipulation

The large size and complexity of the SNO detector requires that calibration measurements be done at several positions inside and outside the fiducial volume. This required the development of an accurate source-positioning system which can deploy and retrieve calibration devices without introducing radon-polluted deck air.

In SNO, all the optical, γ-ray, β-ray, neutron, and background sources will be inserted into the heavy water volume of the detector via the Universal Interface (UI) which interfaces the top of the acrylic vessel neck to the upper deck. Sources are lowered into the detector and can be situated within two orthogonal vertical planes (east-west and north-south) of the detector via a system of ropes and pulleys (see Figure 4.1). Source positions can be determined to better than 5 cm accuracy. Most of the sources require signal and power wires from the deck for triggering apparatus. The laserball requires fiber optic cable and the short-lived radioisotope sources (see chapter 5) require gas lines. Each source therefore has an umbilical which connects to the source via compression fittings. The umbilicals consist of 35 meter long, 1.27 cm outer diameter, silicone tubes. Signal wires, fiber optic and gas lines, etc. are potted inside the silicone tubing with silicone gel (GE-RTV615). Certain calibration devices can also be lowered into the light water volume between the acrylic vessel and PSUP via guide tubes which penetrate from the deck.

4.2 Electronics, phototube, and optical calibration

The calibration procedure for Čerenkov detection can be divided into four major categories. These are electronics (ECA), PMT (PCA), optical (OCA), and absolute energy scale calibration. Short descriptions of the first three categories are given here. A detailed description of the energy scale calibration is given in the next section.

The ECA calibration consists of determining the transfer functions used to convert the stored digitized information, or ADC values, for each PMT channel into charges (picoCoulombs) and times (nanoseconds). For each pulse from a PMT there are three charge measures, a high gain/long integration time (QHL), high gain/short integration time (QHS), and low gain/selectable integration time (QLX). Calibration for the three charges and one time conversion consists of first determining their pedestal values and then their slopes. For the charges, the pedestal is determined by triggering the PMT a finite number of times with no charge input and taking the mean ADC value. Varying charges are then injected into the system and the mean ADC values for each setting measured. Subsequent off-line analysis fits the ADC count versus injected charge to a low-order polynomial. The time pedestals and slopes are determined in a similar fashion with the time between the PMT input pulse and trigger varied in small increments.

The PCA calibration deals with the individual PMT gains, or conversion of picoCoulombs into photoelectrons, and the corrections due to the timing dependence on the PMT charge, or "walk" correction. Runs with the laserball positioned at the center of the detector, emitting light to provide a single photoelectron in each PMT on average, permit the relative gains of each PMT to be monitored. Subsequent runs at progressively higher intensities permit a charge vs time mapping

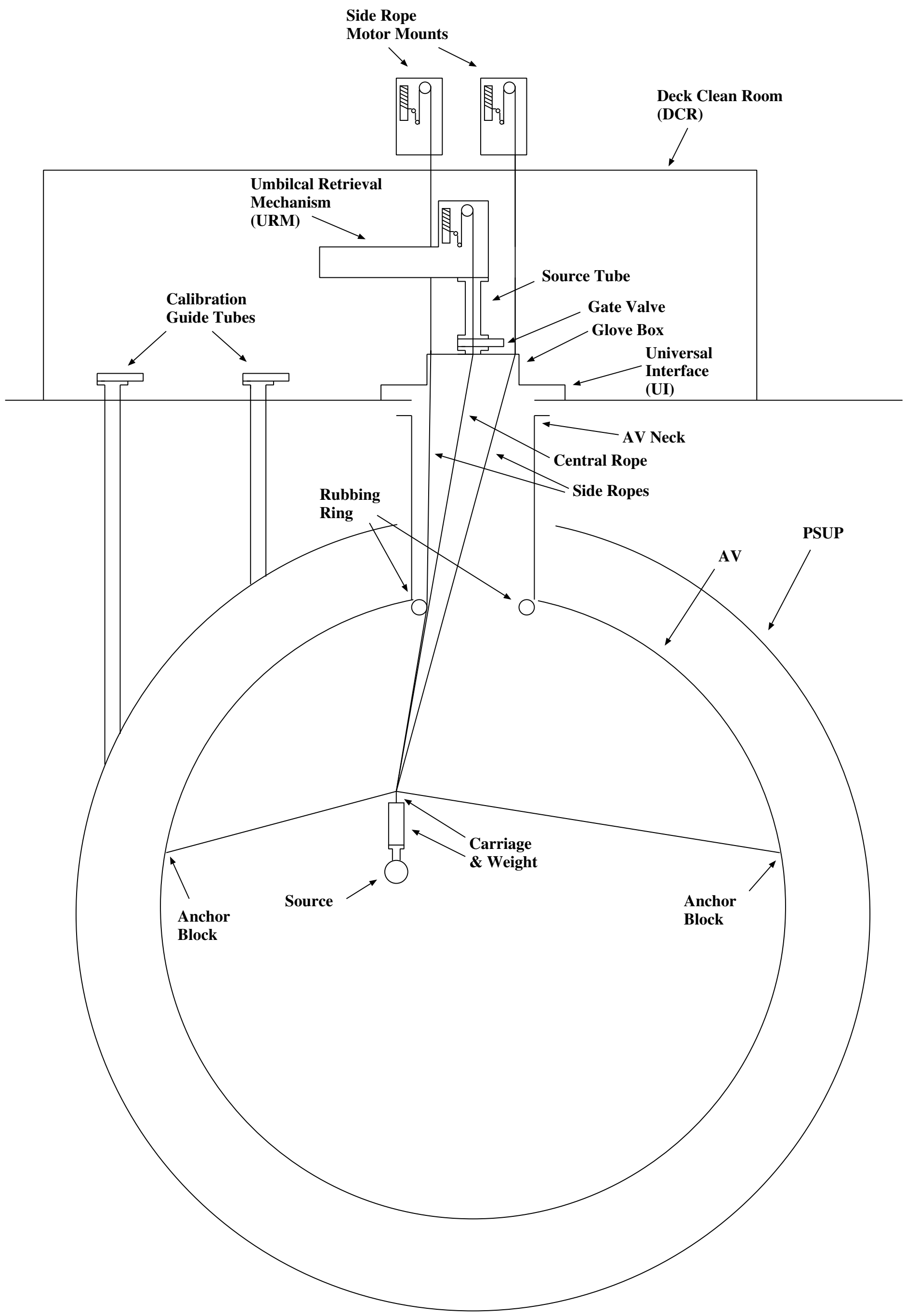

Figure 4.1: The source manipulator system used for moving calibration sources inside the SNO water volumes. Figure taken from [70].

for the walk correction. In addition, the laserball at the center position is used to determine time off-sets for all the channels. These measurements are meant to complement earlier off-line measurements of the individual phototube properties measured at Queen's University [71]. These off-line measurements were done at a 0.25 photoelectron (PE) threshold and included measurements of the relative efficiencies, noise, timing resolution, and timing characteristics.

The OCA calibration determines the attenuation and scattering coefficients through the D_2O, acrylic, and H_2O, and the reflection properties of the detector. The attenuation coefficients are determined by placing the laserball at various locations and measuring the integrated light measured by the detector for different wavelengths. Additional information on the acrylic attenuation can be obtained by placing the laserball inside the light water volume for comparison. Scattering and reflection properties can be studied by looking at the summed timing histograms for all the channels. This will have a prompt peak corresponding to direct light, and late peaks due to reflections off the acrylic, PSUP, and concentrators. Additional processes, in particular Rayleigh scattering, will result in slightly late hits and their impact can be assessed by determining the number of hits in time slices slightly after the prompt peak. Additional features like PMT after-pulsing can be studied with the timing structure as well. The relative phototube efficiencies will be studied with the laser set at longer wavelengths so that the D_2O, acrylic, and H_2O are most transparent. A more detailed description of the optical calibration can be found in [72, 73].

The calibration constants determined with ECA, PCA, and OCA measurements and analysis are input into SNOMAN and then tested with calibration devices. For example the performance of the timing constants is judged by how well the event vertex position algorithms work (see below). If these calibrations are successful, the absolute energy scale determination (see below) is introduced into the SNOMAN and further tests done with Čerenkov sources.

4.3 Energy scale calibration

The last step in the calibration procedure for Čerenkov light detection is the determination of the absolute energy scale. The number of photons produced is proportional to the initial radiating particle's energy. The number of photomultiplier tubes hit in an event, NHIT, is also proportional to the number of photons produced and hence can be used as an energy estimator. Figure 4.2 shows the Monte Carlo determined NHIT distributions for 10 MeV electrons and gamma-rays. NHIT is used instead of the total integrated charge because photodetection is mostly at the single photoelectron level and the PMT charge resolution is insufficient in this range. Given that NHIT can be used as the energy estimator, the final adjustment of the absolute energy can therefore consist of adjusting SNOMAN so that its NHIT response (NHITs per MeV) agrees with that from calibration devices with known energy output in MeV.

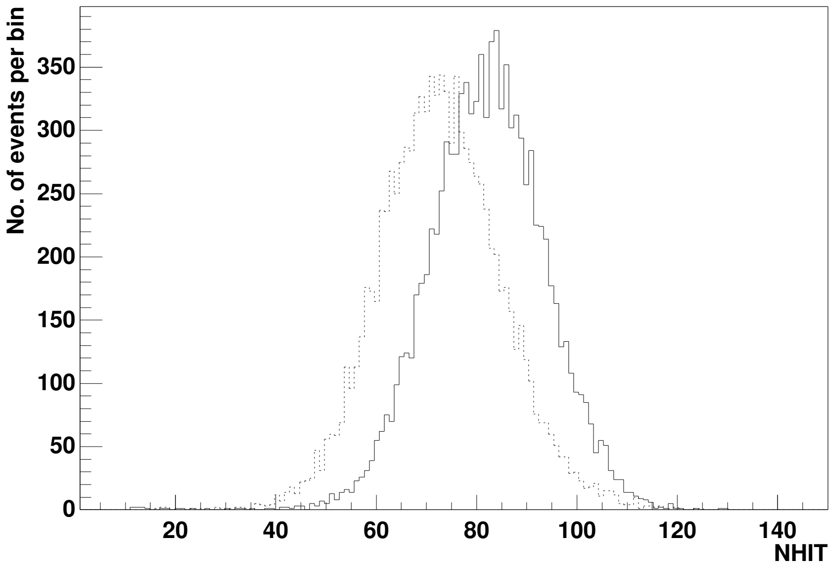

Figure 4.2: NHIT distribution for 10 MeV electrons (solid line) and gamma-rays (dotted line). Both distributions are from Monte Carlo simulations (10 000 events each).

SNO uses mono or nearly monoenergetic γ-rays for this purpose. The main calibration source, which is described in detail in chapter 5, uses the γ's from the decay of ^{16}N. The calibration procedure consists of accumulating data from the ^{16}N source placed at the center of the detector and comparing the resulting NHIT distribution to that determined via the SNOMAN Monte Carlo (MC). A first order estimate of the scaling factor, S_{Energy}, can then be obtained from the ratio of the NHIT means

$$S_{Energy} = \frac{\mu_{DATA}}{\mu_{MC}}. \tag{4.1}$$

S_{Energy} is then used as a single parameter to multiply the PMT collection efficiency for every tube. Such a tuning procedure is justified because the overall absolute energy scale determination made with a single calibration measurement improves the accuracy, even though all the measured phototube and optical properties have been included as completely as possible. S_{Energy} would be recalculated with the scaled Monte Carlo result and the process repeated until S_{Energy} was within a fraction of a percent of unity. A more refined analysis would then be done with a χ^2 test of the binned NHIT values for Monte Carlo and experimental results. The PMT collection efficiency corresponding to the minimum χ^2 value would then be chosen for the most accurate determination of S_{Energy}. This procedure was applied to recent ^{16}N source data and the results are presented in chapter 7.

4.4 Systematic uncertainties in the energy response measurements

The possible systematic uncertainties associated with the detector energy measurements can be divided into the three following categories,

- those associated with the modeling of the calibration source used to measure the energy scale,
- those associated with the differences in electron and gamma-ray modeling,

and

- those associated with the modeling of the SNO detector.

The systematic uncertainties associated with the ^{16}N source are discussed in chapter 6. The latter two categories are discussed below.

In SNO, the energy calibration is done with gamma-rays and it is assumed that the Monte Carlo properly treats the difference between electrons and γ-rays. If, however, there is any uncertainty in how the Monte Carlo treats these differences, it should be included as an additional systematic uncertainty in the energy scale determination. The main difference in γ-ray detection is that there is a multiplicity of electrons produced. The total number of Čerenkov photons produced for γ-rays is therefore reduced because the additional electrons produced as the gamma-ray loses energy will eventually fall below the Čerenkov threshold. In addition, pair production processes will affect the total number of photons produced. Any uncertainty in the calculation in the number of Compton processes above the Čerenkov threshold, or the relative cross-sections for pair production versus Compton scattering, would result in a systematic shift in the energy scale determination.

To study the effect of the above, 100 000 6.1 MeV gamma-rays were generated with the Monte Carlo and the number of Compton and pair production interactions for each event cataloged. The 6.1 MeV γ-ray was chosen because it is near in energy to the γ's for the ^{16}N source. The distribution in the number of Compton scattering interactions above the low energy Čerenkov threshold is shown in Figure 4.3 (left panel) where the mean is 2.46. The NHIT values as a function of the number of Compton interactions, normalized to the mean value of 2.46, are shown in the Figure 4.3 right panel. There is a reduction of roughly 7.6 % in the mean NHIT value for each additional interaction. Also shown is the mean value if events in which pair production occurred are ignored (a 2 % increase in mean).

We now consider the uncertainties in the EGS4 calculations of the number of Compton scattering interactions and pair production to determine the uncertainty in the absolute energy normalization. The important calculations in EGS4 are the cross-sections and the number of Compton scattering interactions (equivalent to the number of electrons produced). The total pair-production

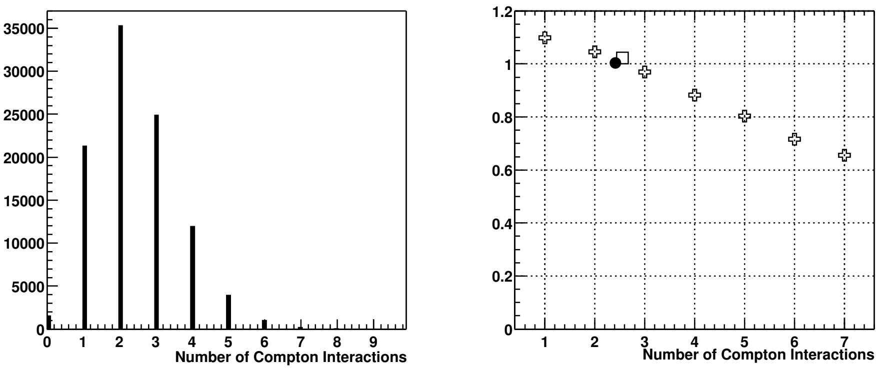

Figure 4.3: Effect of Compton scattering and pair production. The left panel shows the number of Compton scattering interactions above the Čerenkov threshold for 6.1 MeV gamma-rays. The right panel shows the ratio of the mean NHIT value as a function of the number of Compton scattering interactions above the Čerenkov threshold (open crosses) compared to the averaged result (dot). Also shown is the value for events in which pair production is absent (open square).

cross-section below 50 MeV in EGS4 used in SNOMAN is taken from Storm and Israel where an approximate accuracy to within 5 % is reported [74]. The resulting contribution to the uncertainty in the absolute energy scale determination due to uncertainties in this cross-section would therefore be negligible (< 0.1 %) given that the total contribution from events involving pair-production changes the mean NHIT value by only 2 %. The total number of Compton scatters, and the energy imparted to electrons on each scattering interaction, are directly related to the differential cross-section. In EGS4 the differential and total cross-section for Compton scattering is calculated using the Klein-Nishina formula which assumes the electron is free. This assumption is valid if the momentum transferred to the electron is much greater than the initial momentum of the electron within an atom or a molecule. Even at energies as low as 300 keV, atomic binding effects only have a 0.3 % effect on the total scattering cross-section for water [75]. Binding effects should therefore not affect the cross-section calculation for the energy range of interest (i.e. where Compton scattering dominates and above the Čerenkov threshold). Also, higher-order electrodynamic corrections for the Klein-Nishina formula are of the order of one percent only for the total cross-section and less for the shape of the differential cross-section [75]. The uncertainty in the average number of Compton scattering interactions is therefore below a fraction of a percent and therefore the effect on the mean NHIT value is less than 0.1 % as well. From the above, it is clear that cross-section data and the physics principles used for the γ-ray interactions cannot contribute significantly to the uncertainties in the energy determination.

If there is any uncertainty in EGS4, it would be associated with the details of the code itself such as "bugs" or the choice of step length and threshold cut parameters used in the particle propagation. The important step length parameter is the maximum fractional "continuous" energy loss between steps in the propagation code. The threshold parameters determine the energies at which a particle stops being tracked or below which no new particle can be created. Details of the step length and cut parameters can be found in the EGS4 user's manual [58]. The EGS4 code has been tested extensively on a wide variety of experiments and it is therefore unlikely that major flaws exist in the coding [76]. Also, tests in which the EGS4 code was tested against

GEANT [60] (another particle simulation code) have been done for experiments similar to SNO (i.e SuperKamiokande) [77]. The choice of code parameters can, however, have on impact on the EGS4 simulation [78]. An earlier study assigned a 0.2 % uncertainty in the total Čerenkov light output in SNO for electrons due to the choice of parameters [79]. For gamma-rays, the interaction cross-sections are relatively low compared to those for electrons (i.e the radiation lengths are long), and therefore the choice of parameters such as step length should matter less in the treatment of the primary γ-ray propagation. If there is any uncertainty associated with Čerenkov light output for γ-rays it is due to the subsequent electron interactions in the shower. The major uncertainty is in the electron propagation and is therefore common to both electrons and gamma-rays. However, because the uncertainties in the electron study were due mainly to the treatment of the light output near threshold, and there is an average of 1.5 additional electrons from each γ, an additional uncertainty of 0.3 % (1.5 times the uncertainty reported in [79] for single electrons) is assigned to the energy scale determination. This is likely a very conservative estimate.

The uncertainties associated with the modeling of the SNO detector include the energy scale and resolution as a function of energy, and as a function of position and direction. These systematic uncertainties are due mainly to the uncertainties associated with the parameterization of the detector optical properties. Certain of the uncertainties associated with the measurement of individual optical parameters can be estimated, but because of the complexity of the detector and the possibility that subtle optical effects are ignored, the uncertainties in the absolute energy response must be measured independently. These measures can be provided by direct comparison of Monte Carlo calculations with data from γ-ray calibration sources at several energies and placed at various positions within the SNO fiducial volume. To discuss this comparison, we first use Monte Carlo calculations to discuss the response of the SNO detector to electron energy and its variation with event position and direction.

Given the primary energy scale determination with the ^{16}N source, the Monte Carlo can be used to calculate NHIT as a function of energy. This is shown in Figure 4.4 where the mean NHIT response is given as a function of energy for electrons and gamma-rays. For each Monte Carlo calculation, a PMT dark noise rate of 0.5 KHz was used. The calculated NHIT scales roughly linearly as a function of energy and can be expressed with functions of the form

$$NHIT = -0.26 + 8.18 * E(e^-) \tag{4.2}$$

and

$$NHIT = -8.37 + 8.12 * E(\gamma) \tag{4.3}$$

for electrons and gamma-rays, respectively. The energies in equations 4.2 and 4.3 are in MeV. Functions 4.2 and 4.3 are equivalent to the more general expression

$$NHIT = \beta_E * (E - A) + Noise \tag{4.4}$$

with the the constants β_E and A calculated separately for electrons and gamma-rays. In the above expressions, β_E is a measure of the absolute energy scale (or NHITs per MeV) and is quite similar for electrons and gamma-rays. $Noise$ is the PMT dark noise contribution to the observed NHIT value. The parameter A is an energy off-set and is directly related to the threshold for the Čerenkov light production and the lower Čerenkov yield near this threshold (see equation 3.6). For γ's, the off-set is higher because of multi-electron production due to Compton scattering.

Equation 4.4 has a linear relationship between NHIT production and event energy which is quite accurate over most of the detection energy range. However, deviations at low energy due to threshold effects, and at higher energy due to multiple photoelectron (MPE) detection, may make the true response deviate from this linear relationship. The Monte Carlo should take these effects into account. Verification of the NHIT dependence on energy will be done with the NaI, ^{16}N, and (p,t) sources. The ^{16}N source will provide the absolute normalization, the NaI will test the response at low energy, and the (p,t) source will test the response at high energy.

The energy resolution is here defined as the ratio of the NHIT width to its mean. The width of the distribution is defined as the square root of the average of the deviations from the mean squared, or RMS. This is shown in Figure 4.5 as a function of energy for both electrons and gamma-rays. In both cases, the resolution is best fit to a quadratic function. The energy resolution is mostly due

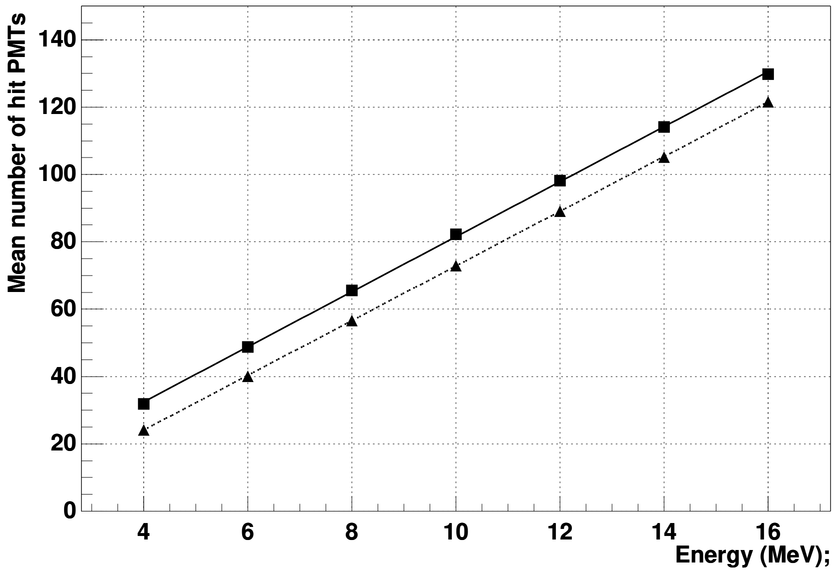

Figure 4.4: Mean NHIT values as a function of energy for electrons (solid line) and gamma-rays (dotted line). For each energy, 10 000 events were generated using the SNOMAN Monte Carlo.

to photon statistics in Čerenkov light production. It is, however, also dependent on the detector optical properties and the charge resolution and threshold of the individual phototubes in the photo-array. Verification of the Monte Carlo energy resolution prediction for gammas will be done with the NaI, ^{16}N, and (p,t) sources.

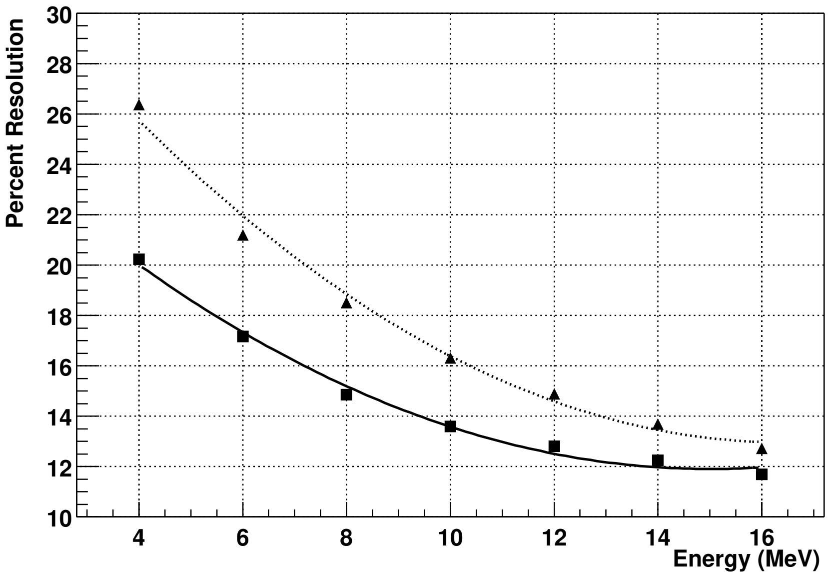

Figure 4.5: Percent resolution as a function of energy for 10 MeV electrons (solid line) and gamma-rays (dotted line). For each energy, 10 000 events were generated using the SNOMAN Monte Carlo.

The Monte Carlo NHIT response averaged over the detector was shown in Figure 4.4. Optical properties of the detector, such as attenuations through the various detector media, should introduce noticeable dependences on the event position and direction. This is illustrated in Figures 4.6 and 4.7 for Monte Carlo generated 10 MeV electrons and gamma-rays, respectively. In both figures, the mean number of NHITs is given as a function of radius cubed and and $\cos\theta_{\overline{r}}$, which is the cosine of the angle between the vector joining the detector origin and the Monte Carlo particle generation position, and the Monte Carlo generation direction. In Figure 4.7 for gamma-rays there is an obvious increase in the mean NHIT value for outward-going events near the edges of the fiducial volume. This is due to events in which Compton scattering of the initial gamma-ray occurs in the H_2O volume and the light is not attenuated by the acrylic. Figure 4.8 shows the mean NHIT values for γ-rays if the reconstructed event positions and directions (see section 4.5) are used. In this instance, mostly the Compton scattering interactions which occur in the D_2O are selected. The figure for the reconstruction of the mono-energetic electrons is not shown because it is not very different from the results of Figure 4.6. The variations shown in Figures 4.6 and 4.7 are for the optical and energy scale parameters used in the 3.0185 version of the SNOMAN Monte Carlo and therefore the response will likely change once the actual measured OCA and energy scale parameters are used.

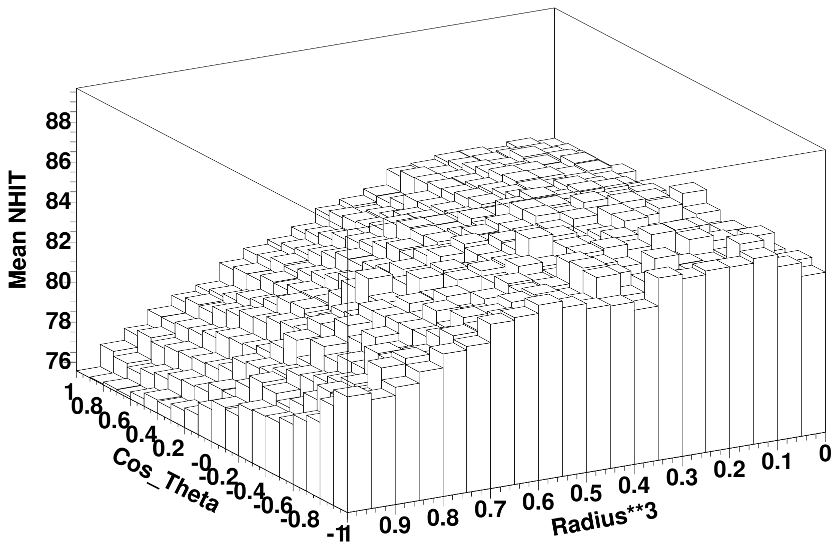

Figure 4.6: Mean NHIT values as a function of position and direction for 10 MeV electrons. NHIT means were calculated from 1 000 000 Monte Carlo electrons generated evenly throughout the D_2O volume.

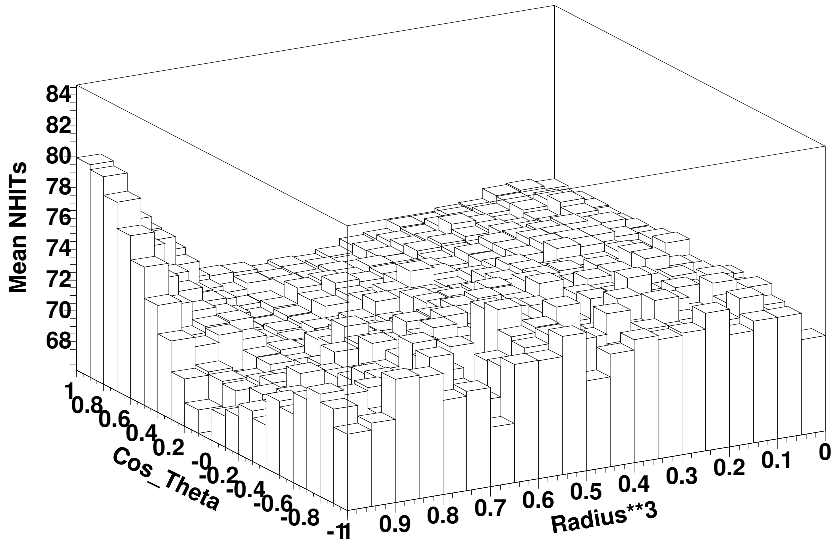

Figure 4.7: Mean NHIT values as a function of position and direction for 10 MeV gamma-rays. NHIT means were calculated from 300 000 Monte Carlo gamma-rays generated evenly throughout the D_2O volume. The increase in the mean for outward-going γ-rays near the edges of the fiducial volume is due to Compton scattering in the light water volumes where there is no light attenuation due to the acrylic.

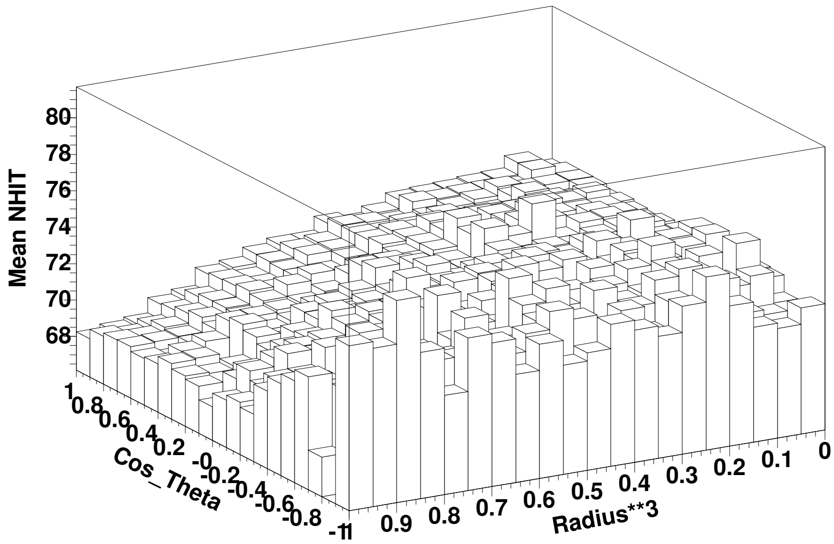

Figure 4.8: Mean NHIT values as a function of position and direction for reconstructed 10 MeV gamma-rays. NHIT means were calculated from 300 000 Monte Carlo gamma-rays generated evenly throughout the D_2O volume.

The energy response as a function of position and direction should be reproduced by the Monte Carlo provided the optical calibrations are correct. Verification of the Monte Carlo will be done with calibration data for sources at different positions within the fiducial volume. The fitters used to determine event position and direction are described in the next section 4.5. The difference in the mean number of NHITs for calibration data and Monte Carlo will be used as a measure of this deviation and can be expressed by:

$$\Delta\mu^{\overline{x},\overline{u},E} = \frac{\mu_{DATA}^{\overline{x},\overline{u},E} - \mu_{MC}^{\overline{x},\overline{u},E}}{\mu_{DATA}^{\overline{x},\overline{u},E}} \tag{4.5}$$

where the superscript $\overline{x}$ represents event position, $\overline{u}$ is event direction, and E is the source energy. For both data and Monte Carlo, the reconstructed position and direction will be used. The energy resolution will also be tested with

$$\Delta\sigma^{\overline{x},\overline{u},E} = \frac{\sigma_{DATA}^{\overline{x},\overline{u},E} - \sigma_{MC}^{\overline{x},\overline{u},E}}{\sigma_{DATA}^{\overline{x},\overline{u},E}} \tag{4.6}$$

where the σ's are the RMS's of the NHIT distributions. The above measures will be used to verify the optical calibration results and may even be used to constrain optical inputs in the Monte Carlo. Eventually they will be used to define the systematic uncertainties in the energy response (energy scale and resolution) as a function of position and direction and will be incorporated in the neutrino analysis as discussed in section 3.3. Preliminary analysis of the ^{16}N position and direction dependence is presented in chapter 7 from data taken with the source located at various positions along the Z axis of the detector.

4.5 Vertex fitters and the position and angular resolution

For both Figures 4.6 and 4.7, the detector response was presented with the actual positions and directions of the electron and γ-ray particle creation in the Monte Carlo. In the event analysis the reconstructed position and direction will be used. For γ-rays it will be the reconstruction of the Compton scattering vertices as shown in Figure 4.8. The following therefore discusses the reconstruction algorithms, or "fitters", and methods for assessing their performance.

The simplest of the fitters is the time fitter which takes the positions, r_i, and times, t_i, of each hit photomultiplier tube in an event and calculates the transit time deviation which is defined as

$$\Delta t_i = \frac{1}{c}(r - r_i) - (t - t_i) \tag{4.7}$$

where $(r - r_i)$ is the distance of the fit position to the tube, and $(t - t_i)$ is the time difference between the fit time and the pmt time. The best fit is given when the χ^2 statistic

$$\chi^2 = \frac{1}{n-4}\Sigma\left[\frac{(\Delta t_i)^2}{\sigma_i^2}\right] \tag{4.8}$$

is minimized. Here σ_i correspond to the timing resolution of the phototubes. The direction can then be taken as the average of the vectors from the fitted position to the tubes used in the fit. Noise and scattered and reflected light can affect the resulting fit. In order to avoid such effects, the fit is repeated multiple times, each time rejecting the most out-of-time tube. The process is repeated until all the phototubes lie within a time window of predetermined width. An early time and a late time with respect to the final fit time are used to define the window. The default early and late times are set to 8 nsec and 4 nsec, respectively. Other fitters have also been developed which use slightly different algorithms [80–82].

The measures of the fitter performance are its position resolution, angular resolution, and reconstruction efficiency, all of which will have an impact on the neutrino analysis (see section 3.3). Figure 4.9 shows the difference in the Monte Carlo generation position and the time-fitted position for 10 MeV electrons and γ-rays. The gamma-ray resolution is broader simply because the Compton scattering vertices are fitted and not the gamma-ray origin. The angular resolution is given by the difference in the fitted direction compared to the original electron track direction. The cosine between these two vectors is shown in Figure 4.10 for 10 MeV electrons, and for values greater than zero can be fit to an exponential.

To verify the performance of the fitters and their efficiency, the ^{16}N and ^{8}Li sources will be used. For the ^{16}N source, the reconstructed position distributions from data will be compared to the Monte Carlo. Because the ^{16}N source is triggered, the efficiency of the fitter can also be determined

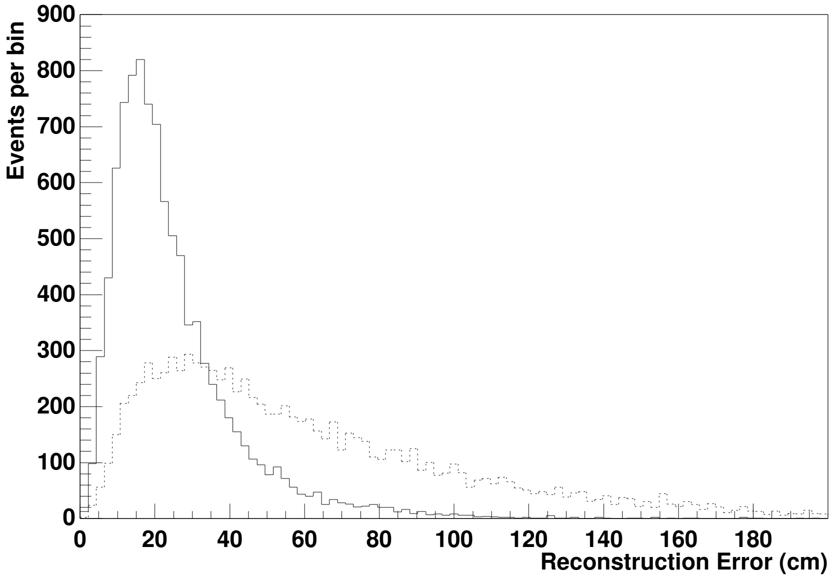

Figure 4.9: Fitter reconstruction performance for 10 MeV electrons (solid line) and gamma-rays (dotted line). Shown are the differences in the event origins and the fit vertex positions. Both distributions were calculated using the SNOMAN Monte Carlo.

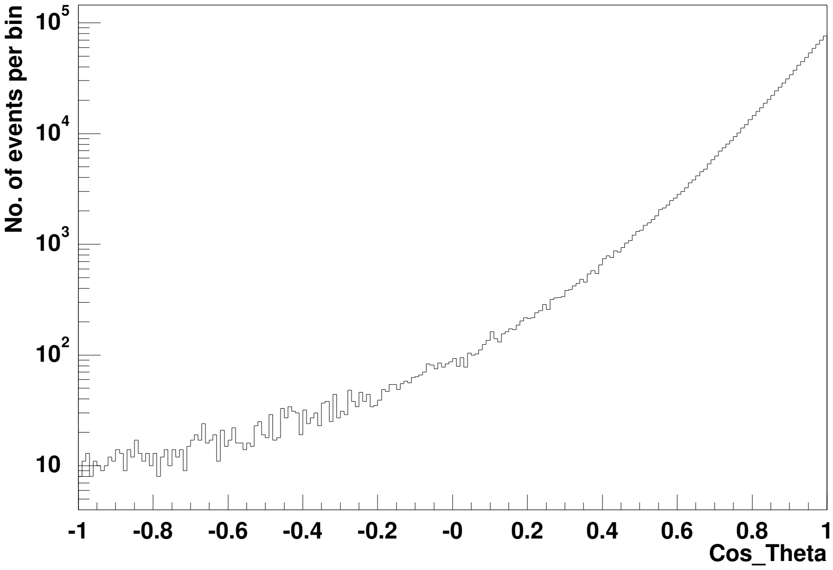

Figure 4.10: Distribution of angles between fit direction and initial track direction for 10 MeV electrons. Calculated using the SNOMAN Monte Carlo (1 000 000 events).

as well as the effect of data reduction cuts. Similar comparisons will be done with the ^{8}Li source. For the ^{8}Li source, however, an electron is produced and is therefore localized near the source. In this instance the absolute fitter resolution can be determined. SNO does not have a collimated electron source and therefore must use gamma-rays for its angular resolution determination. The method applied is illustrated in Figure 4.11 where the initial gamma-ray direction is determined by drawing a vector from the source to the reconstructed position. The angle between this vector and the fitted direction can then be used to determine the angular resolution for gamma-rays. This can be directly compared to the Monte Carlo and conclusions made about the electron angular resolution [83]. Some preliminary fitter studies with ^{16}N data are presented in chapter 7.

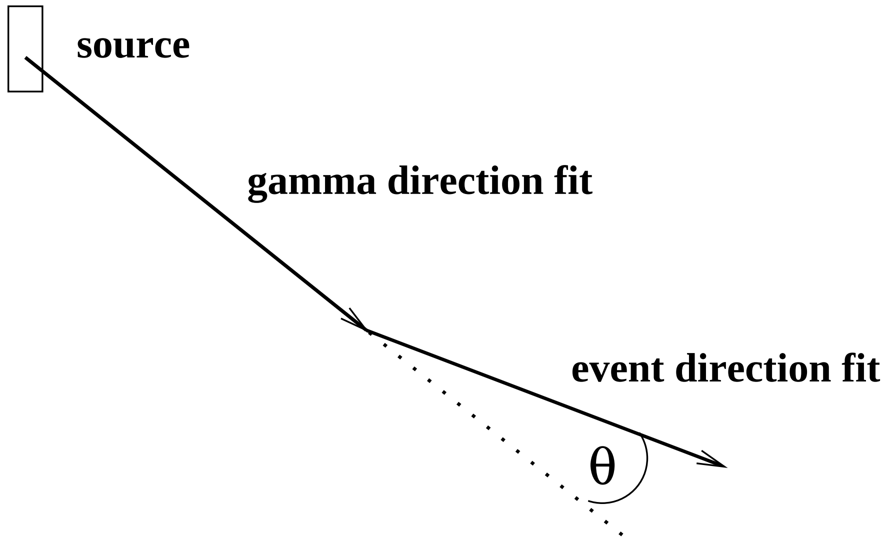

Figure 4.11: Illustration of the gamma-ray angular resolution determination. The angle between the reconstructed gamma-ray direction and the reconstructed event direction, θ, is determined. The resulting distribution is then compared to the Monte Carlo result.

4.6 Event analysis

Once the detector is fully calibrated and the energy response understood, the methods for analyzing data on an event-by-event basis must be developed and then tested. The additional systematic uncertainties associated with this process must also be assessed.

Following data reduction cuts, each event must be classified according to its reconstructed position, direction, and energy, and then incorporated into the neutrino analysis as discussed in section 3.3. The measure of energy can consist of the raw NHIT values of that event. Alternatively, an energy estimate which includes not only phototube hit information, but also corrections for the effects of the detector optical properties and noise could be incorporated. In this instance, each event must be treated separately and the conversion to energy applied prior to any further analyses. In what follows, a discussion of the latter methods for event energy determination are given.

Given that there are noise hit tubes, that there are position and direction dependencies in the NHIT response, and that methods exist for reconstructing event positions and directions, more refined methods for event energy determination should be considered. One possible strategy would be to determine an effective NHIT value, N_{Eff}, which removes the position and direction dependence as well as the noise contribution. Equation 4.4 could then be rewritten

$$E = A_{Eff} + B_{Eff} * N_{Eff} \tag{4.9}$$

where

$$N_{Eff} = (N_{Win} - Noise) * C_{Optical}(\overline{x}, \overline{u}, E) * C_{Hardware}(\overline{x}, \overline{u}), \tag{4.10}$$

and A_{Eff} and B_{Eff} would be the scaling factors determined via the Monte Carlo. Above, N_{Win} is the number of phototubes that fire within a time-of-flight corrected time acceptance window, $Noise$ is the estimated number of dark noise PMT hits in the time acceptance window, and $C_{Optical}(\overline{x}, \overline{u}, E)$ and $C_{Hardware}(\overline{x}, \overline{u})$ are corrections for the optical and photo-array response for the N_{Win} hits. The optical correction would take into account the attenuation through the D_2O, acrylic, and H_2O, the PMT angular response, transmission and reflection efficiencies at the media interfaces, and the

MPE effect (see page 84). The photo-array correction would calculate the effective photocathode coverage for a given event's reconstructed position and direction taking into account the relative efficiencies of each of the phototubes in the photo-array.

N_{Eff} would be calculated on an event by event basis using a special SNOMAN data analysis processor which is presently under development [84] and based on methods originally outlined in [73]. The method applies a ray-tracing technique which tracks individual photon paths and calculates the probability for each of the photons to be detected. Summing the probabilities for photon paths representative of the Čerenkov angular and wavelength distributions for a given event position and direction gives the relative NHIT scale for that event. The calculation is analytical but should reproduce the averaged Monte Carlo result.

Figure 4.12 illustrates the above method where a Čerenkov photon path is tracked and the individual optical effects noted. The event occurs with the position given by the radial vector $\overline{r}$ from the origin and the direction given by the vector $\overline{u}$. The angle between the two vectors is given by $\theta_{\overline{r}}$. In this model, spherical symmetry is assumed and therefore all event positions and directions can be expressed in terms of $\overline{r}$ and $\theta_{\overline{r}}$. A more realistic model might include various detector asymmetries such as the acrylic vessel belly plates and variations in the acrylic vessel panel properties. At the initial position (A), photons are emitted at angles θ' and ϕ' with respect to the initial electron direction. The angular distribution of photons g(θ',ϕ') can be taken from the Monte Carlo for either electrons for ν's or gamma-rays for calibration devices. The wavelengths of the photons will correspond to that of the Čerenkov emission distribution (see equation 3.7). If one follows the path of one of the photons, it will first traverse the heavy water volume (B) where it can be absorbed. At the D_2O/acrylic interface (C) it has a probability for reflection or transmission. These probabilities are calculated using the Fresnel reflection coefficients which are functions of the angles of incidence and the refractive indices. The path length through the acrylic, taking into account refraction, is then used to determine the absorption probability through that medium (D). Reflection off the acrylic/H_2O interface (E) and the absorption in the light water (F) must be considered. Finally (G) the photon reaches the phototube where the quantum efficiency as a function of wavelength must be considered, as well as the PMT angular response.

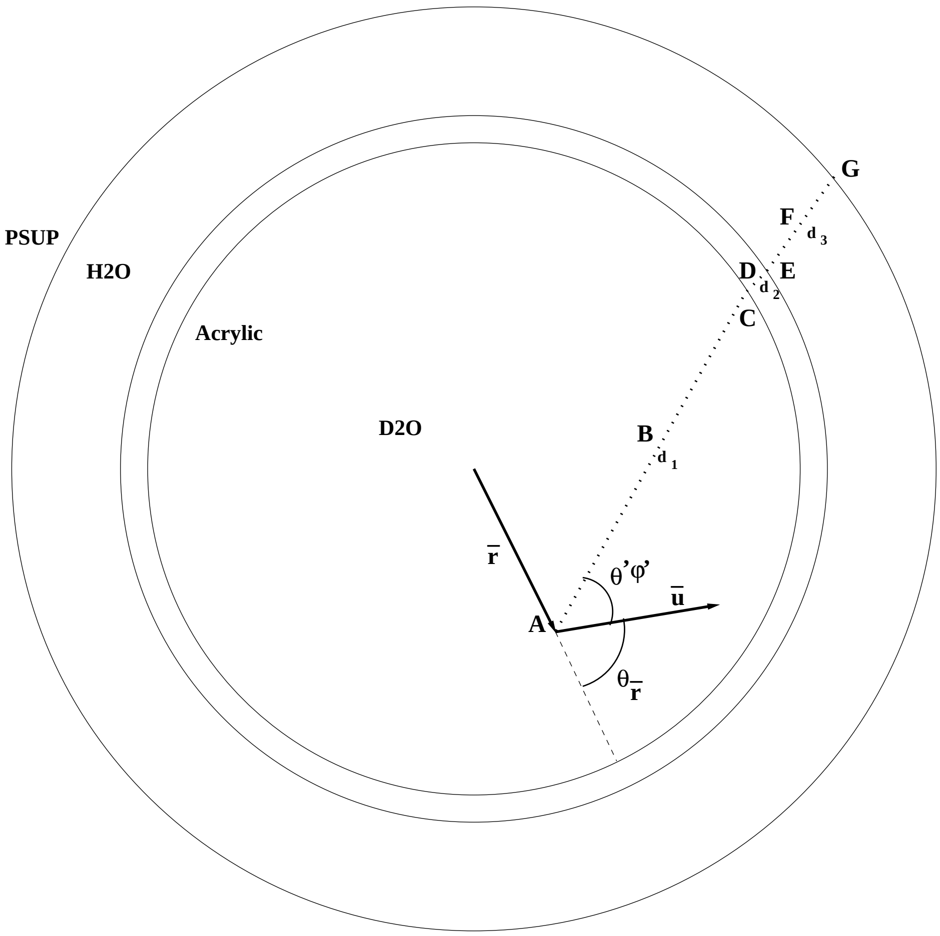

Figure 4.12: Illustration of the optical ray-tracing technique. Shown is the the path of a single photon through the D_2O, acrylic, and H_2O. The letters represent the effects of the various optical properties and are defined in the text. The other symbols are defined in the text as well.

To calculate the overall effect, an integration over all photon paths, g(θ',ϕ'), and wavelengths, λ, is done. This can be done using a Riemannian sum of the form [73],

$$\begin{aligned} C_{optical}(\overline{x},\overline{u})^{-1} = \; & \sum_{\theta'} \sum_{\phi'} \sum_{\lambda} \frac{\epsilon(\lambda)}{\lambda^2} g(\theta',\phi') e^{-\mu_1 d_1} e^{-\mu_2 d_2} e^{-\mu_3 d_3} \\ & \cdot P(r,\theta,\theta',\phi') \cdot C_{Reflection}(r,\theta,\theta',\phi') \cdot C_{MPE}(r,\theta,\theta',\phi',\lambda). \end{aligned} \tag{4.11}$$

The terms μ_i are the attenuation coefficients for D_2O, acrylic, and H_2O, and d_i are the distances through each media. The term $P(r, \theta, \theta', \phi')$ is the PMT angular response, the term $C_{Reflection}(r, \theta, \theta', \phi')$ is a correction for reflections off the H_2O/acrylic and acrylic/H_2O interfaces, and $C_{MPE}(r, \theta, \theta', \phi', \lambda)$ is a correction for the MPE effect (discussed below). For each event position and direction, survival probabilities for 400 rays in θ' and ϕ' are calculated and summed. For each ray, survival probabilities for 100 wavelengths between 250 and 600 nm are calculated and summed. The overall sum is normalized with respect to the result for Čerenkov emission at the center of the detector. Figure 4.13 illustrates the results for such a calculation for 10 MeV electrons.

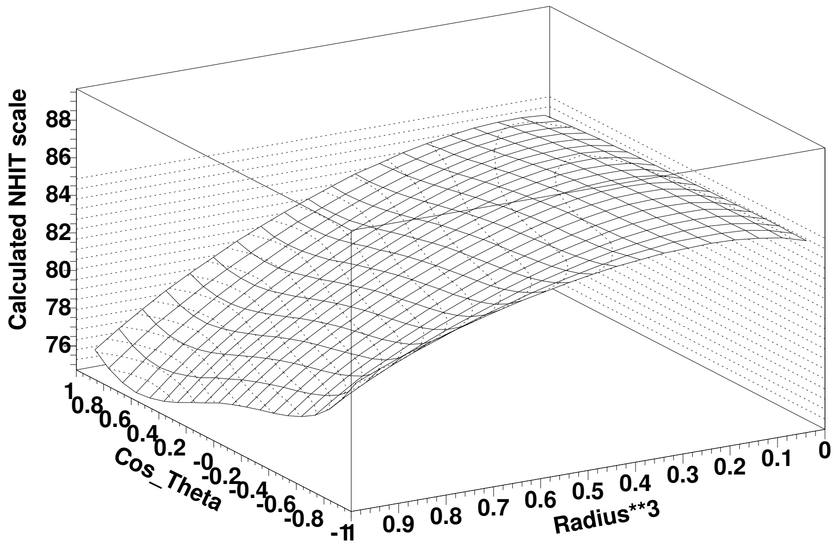

Figure 4.13: The overall optical response using ray-tracing techniques for 10 MeV electrons. The calculation was done using the ROOT analysis package and includes the D_2O, acrylic, and H_2O attenuations, as well as the MPE effect.

With the exception of a small effect due to the Čerenkov angular distribution dependence on energy, the above effects are essentially energy independent. However, because SNO uses the number of PMT hits for energy determination as opposed to the total integrated charge, the effect of multiple photo-electron (MPE) detection in the tubes must be considered. For most of the ^{8}B neutrino range, one expects single photo-electron (SPE) levels. For the higher energy events which are near the edges of the fiducial volume and which are outward-going, one begins to deviate from SPE levels. The MPE effect is incorporated into the equation 4.11 sum by calculating the mean detectable light impinging on the area at the PSUP radius for each ray (for each wavelength) used in the sum. The mean, μ_{Light}, would take into account the PMT quantum efficiency, the Čerenkov emission distribution, the total number of photons produced, and the solid angle. Assuming the distribution of photoelectrons per PMT is Poissonian, the correction factor for each element in the equation 4.11 sum is [73]

$$C_{MPE}(r, \theta, \theta', \phi', \lambda) = \frac{1 - P(0, \mu_{Light})}{\mu_{Light}} = \frac{1 - e^{\mu_{Light}}}{\mu_{Light}}. \tag{4.12}$$

Because the MPE effect is energy dependent, an initial estimate of the energy is determined from NHIT or N_{Win} and is used to estimate the total number of photons produced for the equation 4.12 calculation.

$C_{Hardware}(\overline{x}, \overline{u})$ can also be included in the equation 4.11 sum if for each ray, the effective local photocathode efficiency is calculated. This would be done by integrating the total number of active PMTs near the PSUP position where the ray passes through. This last integral would take into account the relative efficiencies of the individual phototubes. Alternatively, $C_{Hardware}$ can consist of a separate correction factor

$$C_{Hardware}(time) = \frac{N_{Total}}{N_{Live}} \tag{4.13}$$

where N_{Live} is the number of operational tubes in a run and N_{Total} is the PSUP total. Because individual crates or channels (really paddle cards which are groups of eight PMTs) may be turned off during any particular run to await maintenance, $C_{Hardware}$ is a function of time.

If the above energy estimation methods are used, the calibration procedures outlined in sections 4.3 and 4.4 would have to be slightly modified so that the treatment of Monte Carlo and DATA is identical. In this instance, the N_{Eff} or energy distributions would be used instead of NHIT for both the energy scale determination and energy response verification.

Chapter 5

Short-Lived Radioisotope Sources

An important class of calibration devices use the radiations (γ's, β's, and neutrons) from short-lived radioisotopes. In what follows, the radioisotopes and their uses in SNO are described. This includes a description of the systems used for radioisotope production, transfer, and SNO detector triggering. This is followed by a discussion of the radioisotope yields.

5.1 The Radioisotope sources

Systems have been developed for the production of three radioisotopes for calibration purposes. Some of the uses of these sources were discussed in chapter 4. Here, the decay schemes are first presented.

5.1.1 ^{16}N decay

The decay scheme from the table of isotopes for ^{16}N decay to the ground state of ^{16}O is shown in Figure 5.1 [85]. The values were evaluated by Tilley, Weller, and Cheves [86]. As shown, ^{16}N beta-decays a large fraction of the time to excited states of ^{16}O including the 6.13 MeV (66.2 % branch) state and the 7.12 MeV (4.8 % branch) state which subsequently emit γ's of these energies.

28 % of the time it β-decays to the ground state and there are a few other smaller γ-emitting branches. The 6.13 MeV branch dominates and for this reason the ^{16}N source is called nearly monoenergetic. The 7.12 MeV γ branch is the only other significant branch.

Figure 5.1: ^{16}N decay scheme as taken from the Table of Isotopes [85].

For SNO, the idea is to construct a source which would use the Compton scattered γ-ray in D_2O from ^{16}N decay for calibration purposes, and the beta for triggering [87–89]. The source was to be designed such that the beta would be blocked and only the γ-ray would exit into the D_2O or H_2O volume. Even though the source would not be purely mono-energetic, the simplicity of the decay scheme would make modeling easy. Finally, because the ^{16}N half-life is only 7.13 seconds, a method for producing the source in situ and in sufficient quantities had to be developed. The details of how this was achieved are discussed in section 5.2.

5.1.2 ^{17}N decay

The ^{17}N decay from the table of isotopes evaluated by Tilley, Weller, and Cheves is shown in Figure 5.2 [86]. As shown, ^{17}N decays 95 % of the time to excited states of ^{17}O which subsequently decay to the ground state of ^{16}O producing neutrons. The idea here is to use the neutrons for calibration and the coincident β's (endpoint $\approx$ 2.3-4.1 MeV) for triggering [90]. ^{17}N is also short-lived ($\tau_{1/2}$ = 4.173 sec) and methods had to be developed to produce it in situ and in adequate quantities as well.

Figure 5.2: ^{17}N decay scheme as taken from the Table of Isotopes [85]. .

5.1.3 ^{8}Li decay

The decay scheme for ^{8}Li as evaluated by Ajzenberg-Selove is shown in Figure 5.3 [91]. In this instance ^{8}Li decays to the metastable state of ^{8}Be which subsequently breaks up into two alpha particles. Here the beta-ray would be used for calibration of the SNO detector and the α for triggering [92]. The half-life is 838 msec and therefore the production requirements for the ^{16}N and ^{17}N sources apply here as well. One interesting point to note is that ^{8}Li and ^{8}B are mirror decays, both decaying to the metastable state of ^{8}Be. It has been suggested that because of this the ^{8}Li energy spectrum may be useful in the ^{8}B spectral analysis [93].

Figure 5.3: ^{8}Li decay scheme as taken from the Table of Isotopes [85].

5.2 The SNO DT generator and gas calibration system

The radioisotopes discussed in section 5.1 are produced by (n,p) or (n,α) reactions using 14.2 MeV neutrons from a commercial deuterium-tritium (DT) generator. The targets are gaseous or solid. The DT generator can not be inserted directly in the SNO detector volume, and therefore a system had to be designed to rapidly transfer the radioisotopes from the DT generator to the SNO fiducial volume. This is achieved via gas or gas-particle jet flow through thin capillaries. The radioisotopes are sent to a decay chamber within the SNO fiducial volume. The decay chambers are instrumented to trigger the SNO electronics via the detection of coincident decays. The basic features of the gas source system are illustrated in Figure 5.4 where radioisotope production, transfer, and triggering are all displayed. A more detailed description of the systems is given below.

5.2.1 The DT generator

SNO uses a commercial DT generator, the MF Physics model A-320, to produce fast neutrons [94]. A DT generator is basically a miniature particle accelerator that generates 14.2 MeV neutrons by accelerating a mixed beam of deuterium and tritium onto a target containing both

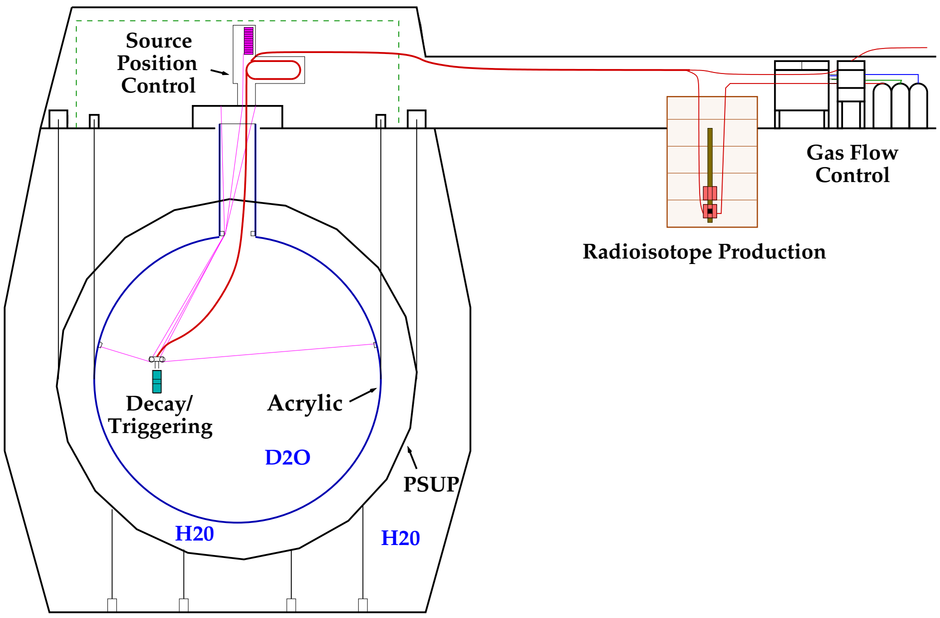

Figure 5.4: Main features of the gas calibration system. Gas from a compressed bottle supply is sent to target chambers at the bottom of a concrete shielding pit labelled radioisotope production. There, neutrons from a DT generator produce short-lived radioisotopes. The activities are transported in the gas stream via thin capillary to a decay chamber within the SNO detection volume. The decay chamber can be placed at various positions within the east-west and north-south vertical planes of the detector. The γ's, β's, and neutrons produced are detected by SNO and used for calibration. The chambers are designed to detect coincident decays for triggering the SNO electronics.

deuterium and tritium. This results in the fusion reaction

$$D + T \longrightarrow n +^4 He \tag{5.1}$$

where the neutrons produced are emitted isotropically.

The A-320 is a sealed-tube neutron generator in which the required ion source, ion optics, and accelerator target are enclosed in a vacuum-tight enclosure. Ceramic or glass is used as high voltage insulation between the ion optical elements. The sealed tube, in turn, is enclosed in a metal housing called the accelerator head and is filled with a dielectric medium for insulating the tube from the external environment. The accelerator head is cylindrical, 2.2 meter long, with a diameter of 4.29 cm. The target is placed 18.73 cm from one end of the accelerator head. The accelerator and ion source high voltage are supplied by external power supplies and control of the D-T generator is via an external console. The A-320 is a pulsed neutron generator with pulse rates adjustable between 200 and 2000 Hz with a 10 % duty cycle. The neutron output is adjustable between 2x10^7 to 1x10^8 per second.

The SNO DT generator accelerator head is mounted on a custom built stand and placed inside a concrete shielding pit located in a lab utility room $\approx$ 40 meters away from the center of the deck above the SNO cavity. The pit effectively eliminates any radiation hazard. An interlock system is in place to assure the concrete blocks of the shielding pit are present, that there is no water in the pit, and that radiation levels in the lab are acceptable. The radiation levels in the lab are monitored with a TEXAS NUCLEAR dose meter. Also included in the interlock loop is an optional computer-controlled on-off switch. Figure 5.5 shows the accelerator head and its mounting stand, the concrete shielding pit, and the adjacent control panels. Also shown are two annular target chambers surrounding the accelerator head and used for ^{16}N, ^{17}N, and ^{8}Li production. Both chambers are mounted on a movable stepper-motor-controlled linear table which can be used remotely to optimize either chamber's position relative to the D-T target for maximizing the neutron flux through them and hence the radioisotope yields. Also placed inside the pit is a fast neutron detector for monitoring purposes.

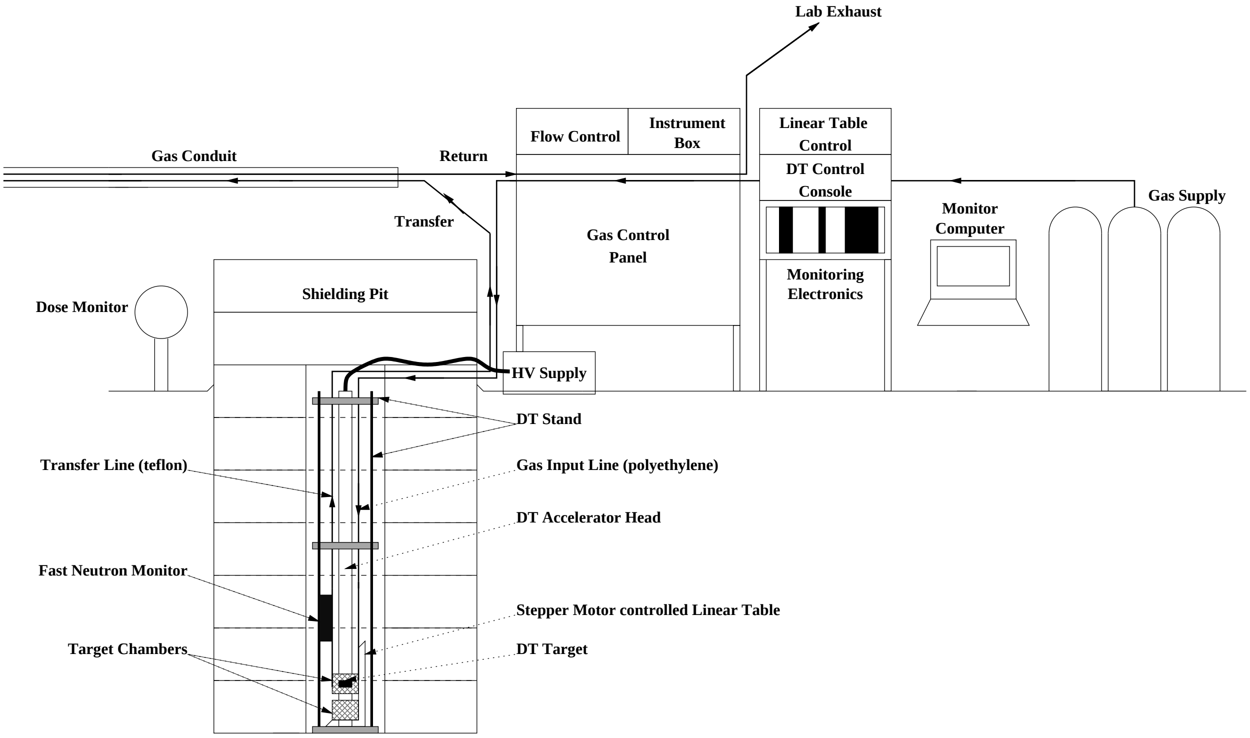

Figure 5.5: Contents of the DT generator pit and surrounding area.

Table 5.1: Summary of radioisotope source properties and cross-sections. Cross-sections taken from [95].

Source	Reaction	Cross section	Half-life	Calibration	Trigger
^{16}N	^{16}O(n,p)	35 mb	7.13 s	6.13 MeV γ	β
	^{19}F(n,α)	25 mb			
^{17}N	^{17}O(n,p)	28 mb	4.4 s	n	β
^{8}Li	^{11}B(n,α)	30.5 mb	0.84 s	β spectrum	α

5.2.2 Radioisotope production

Targets for radio-isotope production with fast neutrons from the DT generator can consist of liquids, gases, or solids provided they contain the appropriate target nucleus. A list of target reactions and their properties is shown in Table 5.1. These targets are contained in one of the two annular target chambers sitting near the target of the DT generator at the bottom of the DT pit.

^{16}N production

A variety of liquid and solid targets were considered for ^{16}N production, including the solid teflon (C_2F_4) and liquids, water (H_2O), heavy water (D_2O), perfluoro-dimethylcyclohexane (C_8F_{16}) [87]. The liquid targets were initially favored because the greater mass density would provide much greater ^{16}N yields. The transfer times for gases, however, were much faster, and the triggering with the β would be simpler if a gas transfer system was used. It was decided that O_2 gas could be used as both target and carrier and hence the target chambers were designed with this in mind. INCO mine regulations deemed oxygen to be a potential fire hazard and so CO_2 is now used as both target and carrier. Oxygen-containing and fluorine-containing fibers were also tested for use in the gas target chambers with a variety of carrier gases acceptable for mine use. The relative yields for the above gas and fiber targets are reported in section 5.3. Certain fibers provided good yields but CO_2 was adequate and was more compatible with the original design concept of the chambers and the transfer system.

^{17}N production

The production of ^{17}N requires the expensive separated isotope ^{17}O and therefore the choice of target has the additional constraint that the total target mass is limited and should preferably be recoverable. Solid targets were considered as well, but $C^{17}O_2$ will likely be used and recovered cryogenically.

^{8}Li production

The ^{8}Li target consists of small target plates made of ^{11}B powder mixed in a polyethylene matrix and was produced at Chalk River Laboratories [96]. The target plates line the walls of the ^{8}Li target chamber. When the ^{8}Li recoils out of the target it is captured on NaCl aerosol particles and transferred out of the chamber in a helium stream. A potential background concern is the production of ^{11}Be via the (n,p) reaction on the ^{11}B target.

Target chambers

Two target chambers were designed. A schematic of the chamber used for ^{16}N production is shown in Figure 5.6, and that used for ^{8}Li in Figure 5.7. Both are annular in shape so they can slide over the DT accelerator head tube. They are both approximately 11.4 cm long and when placed such that the DT target is at the middle of the chamber, provide nearly 4π coverage of the outward going neutron flux. Minor differences in the chamber design are the input and outputs for the gas lines. In one case the gas enters the bottom chamber through a distributor plate and exits the top of the chamber. In the other chamber, gas enters both through the top and bottom and exits through a series of small holes placed around the center of the chamber. Both chambers can be used for ^{16}N, ^{17}N, or ^{8}Li production. The ^{8}Li targets are mounted on sleeves which can be easily slid into either chamber.

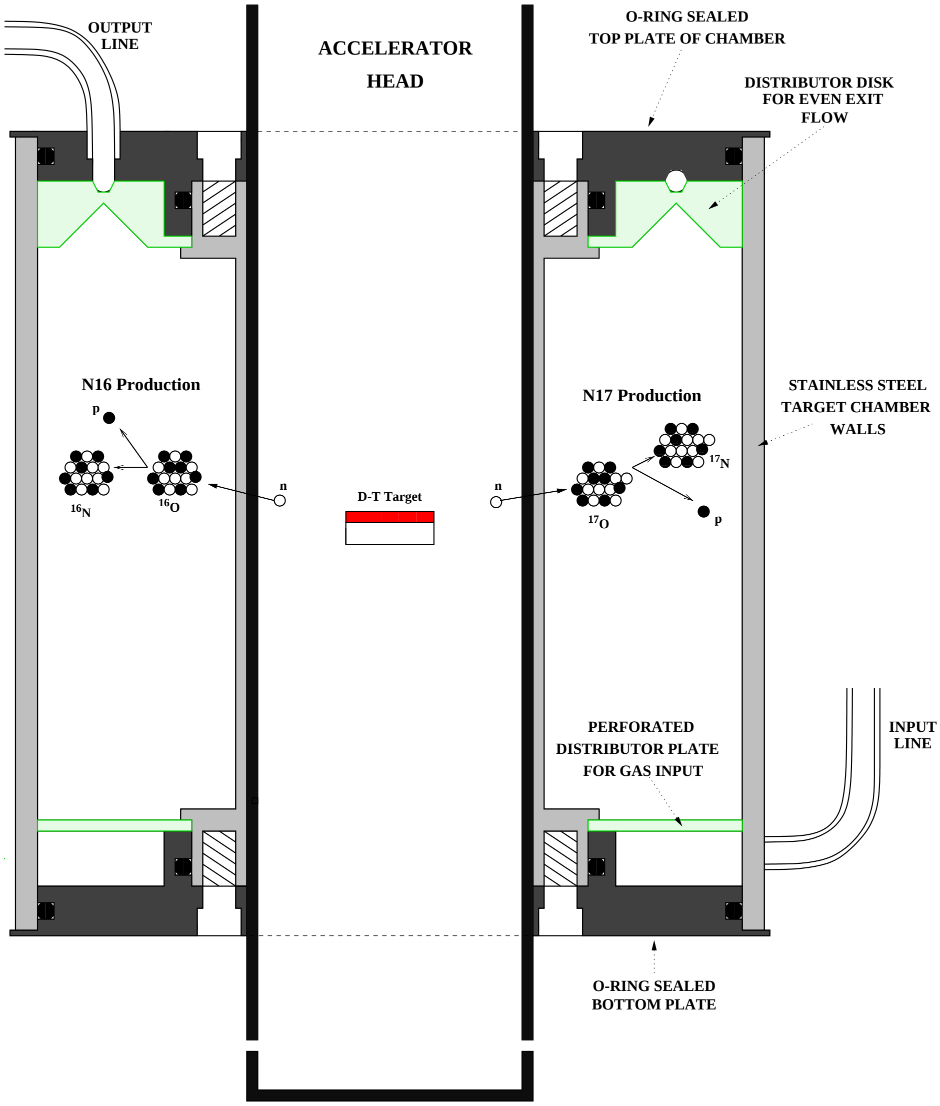

Figure 5.6: Cross sectional view of the annular ^{16}N target chamber.

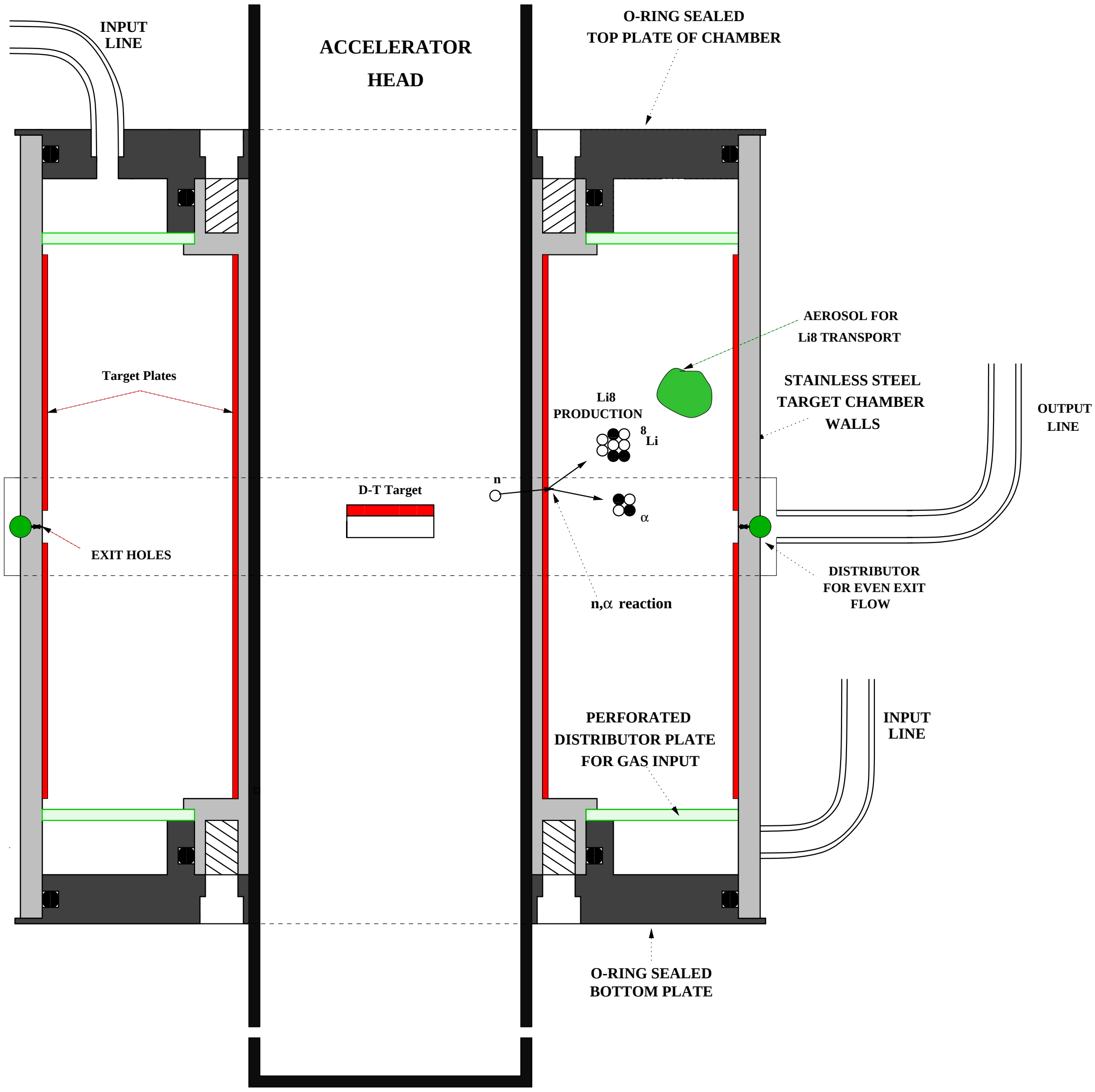

Figure 5.7: Cross sectional view of the annular ^{8}Li target chamber.

5.2.3 The gas transfer and monitoring systems

The purpose of the gas capillary transfer system is to transfer the short-lived isotopes quickly from the target chambers to the deck above the detector, then down to the decay chamber inside the D_2O volume [97]. In what follows, the details of the transfer systems for ^{16}N, ^{17}N, and ^{8}Li are given.

For ^{16}N, CO_2 from a compressed gas bottle is sent via polyethylene tubing to a control panel which directs the flow to the target chamber at the bottom of the pit. From there, the ^{16}N produced is entrained in the gas flow and sent via teflon tubing to the Universal Interface (UI) which interfaces with the detector below. There, the gas flow is sent down an umbilical (see Figure 5.8) through a thin-walled teflon capillary to the decay chamber. The return flow is sent back up the umbilical through a polyethylene line. The capillary and polyethylene are arranged coaxially. From the UI, the flow is sent back to the control panel via polyethylene tubing where it can be sent to the lab exhaust. Flow rates are typically around 200 cm^3 per second and pressures range from 6.5 atmospheres at the target chamber to atmosphere at the exhaust. An alternative to flushing is recirculation with the aid of a metal bellows pump. The list of all the existing ^{16}N gas lines with their lengths and diameters is given in Table 5.2.

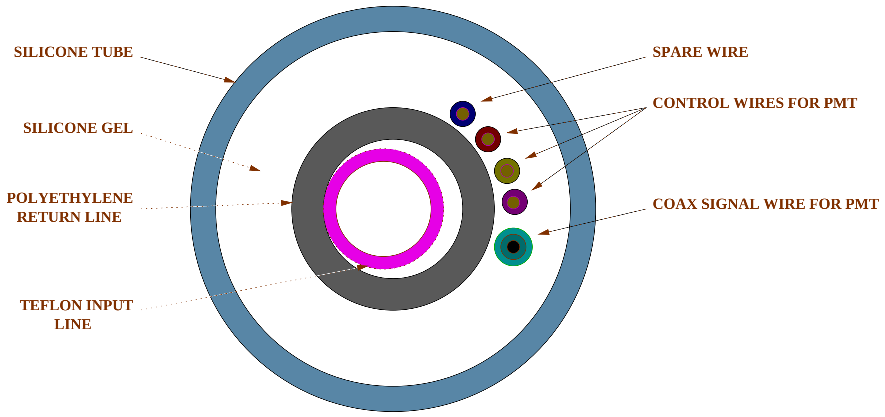

Figure 5.8: Slice through the ^{16}N source umbilical.

Table 5.2: Transfer lines for ^{16}N and ^{17}N calibration. The inner diameters are given. Because the umbilical lines are coaxial, the outer diameter for the thin-walled teflon line is given in brackets.

From	To	Type	Length	Diameter
Gas Bottles	Control Panel	Polyethylene	6 m	0.432 cm
Control Panel	Target Chamber	Polyethylene	6 m	0.432 cm
Target Chamber	Universal Interface	Teflon	43 m	0.3175 cm
Universal Interface	Decay chamber	Teflon	30 m	0.241(0.301)cm
Decay chamber	Universal Interface	Polyethylene	30 m	0.432 cm
Universal Interface	Control Panel/Exhaust	Polyethylene	40 m	0.432 cm

In the case of ^{17}N production, $C^{17}O_2$ is supplied by a small compressed gas bottle and is injected into the gas board and recirculated with a metal bellows pump. Prior to injection, the control panel and all the gas lines are evacuated. After use, the $C^{17}O_2$ is recovered cryogenically by immersing the supply bottle in a liquid nitrogen bath. ^{17}N calibration would use the already existing ^{16}N transfer lines listed in Table 5.2. Cryogenic recovery of pure ^{17}O was tested at Chalk River Laboratories with an 80 percent efficiency [98]. A mock-up of the final system in Sudbury was used, including the target and decay chambers, and an early version of the gas control board. The transfer line lengths for these tests, however, only totalled 30 meters. The recovery efficiency for the full transfer line lengths has not yet been measured. It should be noted that the recovery efficiencies with $C^{17}O_2$ are expected to be higher because of the higher freezing temperature.

For ^{8}Li, the carrier gas is first directed through an aerosol generator, then to the target chamber. The aerosol generator is a quartz tube containing NaCl and mounted on a Lindberg oven which is operated at 600 degrees Celsius. Helium is used as the primary carrier but CO_2 may also be added (at 5 %) as a quench gas for the decay chamber which may be a proportional chamber (see below). Both gases are supplied by compressed gas bottles. The ^{8}Li gas lines are not yet installed but will have lengths similar to those used for ^{16}N calibration.

The gas control panel, shown in Figure 5.9, consists of 21 manual two-way and three-way valves, 14 input and output ports, 2 solenoid valves, 3 flow controllers, 4 pressure gauges, 4 particle filters, 2 pressure relief valves, a recirculation pump, and a vacuum Pirani gauge. Its purpose is to monitor and control the flow of gas through the system. All of the board transducers are connected to the system's main instrument box. The main instrument box has digital displays but also sends the transducer signals to a monitor computer equipped with a National Instruments data acquisition card and LabView software. The gas flow meters are controlled via separate instrument boxes but the signals are directed to the monitor computer via the main instrument box. Control of the solenoids, the recirculation pump, and the oven, is via switches on the main instrument box but can be controlled via solid state relays connected to a digital output card (National Instruments) in the monitor computer.

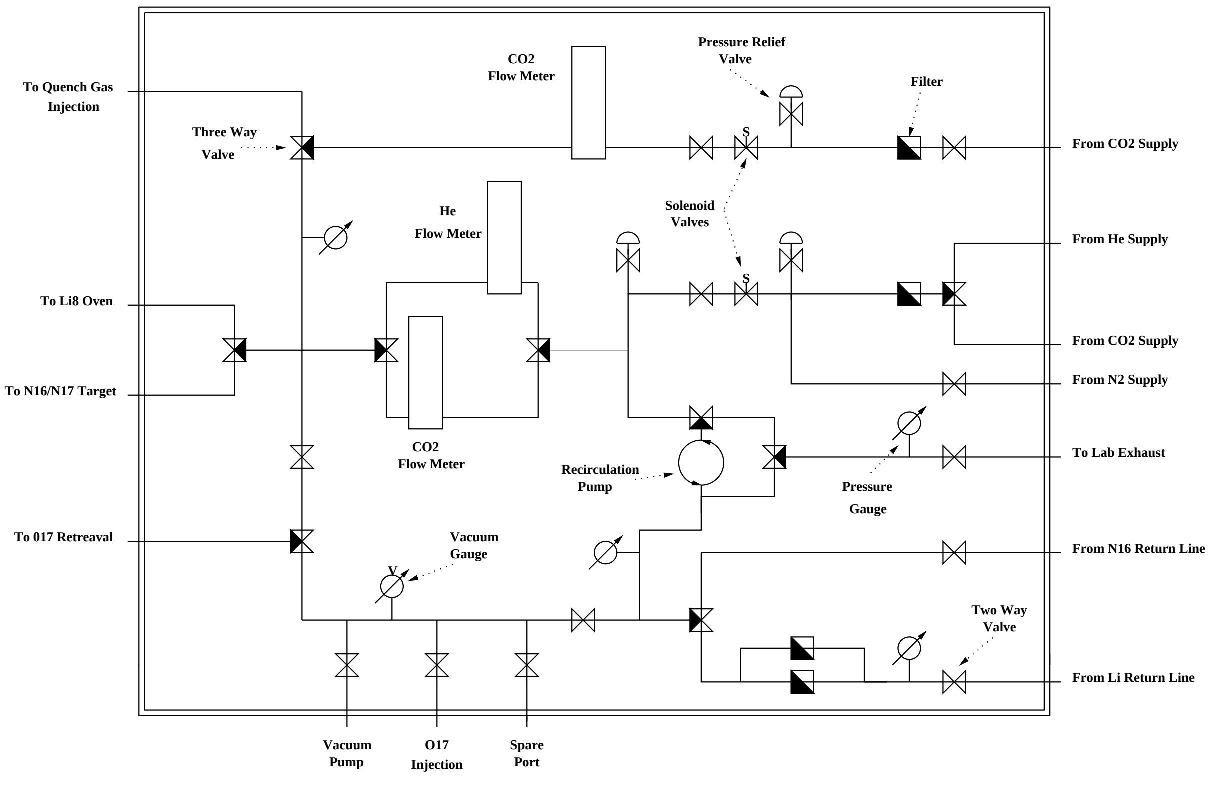

Figure 5.9: The gas flow control board for ^{16}N, ^{17}N, and ^{8}Li transfer systems.

In addition to monitoring flows and pressures, the main instrument box feeds signals from the radiation monitors (inside and outside the pit) and a target position sensor to the monitor computer, and is part of the system interlock. The monitor computer can also communicate the status of the DT generator and gas systems to the lab controls, monitoring, and alarms system (CMA) and to the SNO data stream via TCP/IP protocols.

5.2.4 The decay chambers and source triggering

The ^{16}N and ^{17}N decay chamber

The ^{16}N and ^{17}N sources use the same decay chamber (see Figure 5.10). The decay chamber is a 41.91 cm long, 11.43 cm diameter, stainless steel cylinder with 0.476 cm thick walls. The wall thickness of the cylinder effectively blocks any of the β's from exiting the chamber. The stopping power in steel for 10.4 MeV β's is 2 MeV cm^2/g, and for 3-4 MeV β's is 1.6 MeV cm^2/g. The top and bottom of the cylinder are similarly shielded with stainless steel plates. The top plate, however, has a 1.59 cm diameter hole for entry of the source umbilical which contains the source gas lines and monitoring wires. O-rings around the upper and lower plates provide a seal to the cylinder. Similarly O-rings are used to seal the umbilical. Mounted on top of the chamber is a weight and carriage which interfaces to the SNO source positioning system.

The decay chamber has two compartments, which are separated via an additional central plate and O-ring. The distance between the center plate and the end plates is set by two thin 0.0625 cm thick aluminum sleeves which line the inside of the main stainless steel tube. The lower compartment has the cylindrical decay volume which is surrounded by a 0.3175 cm thick plastic scintillator shell. The scintillator is from BICRON and is made of BC400 plastic. The top compartment has a 5.08 cm PMT for detecting the light from the lower chamber scintillator. The PMT is manufactured by Electron Tubes Ltd (model # 9208B) and was chosen for its use of low radioactivity glass. High voltage for the PMT is supplied by a power supply internal to the chamber.

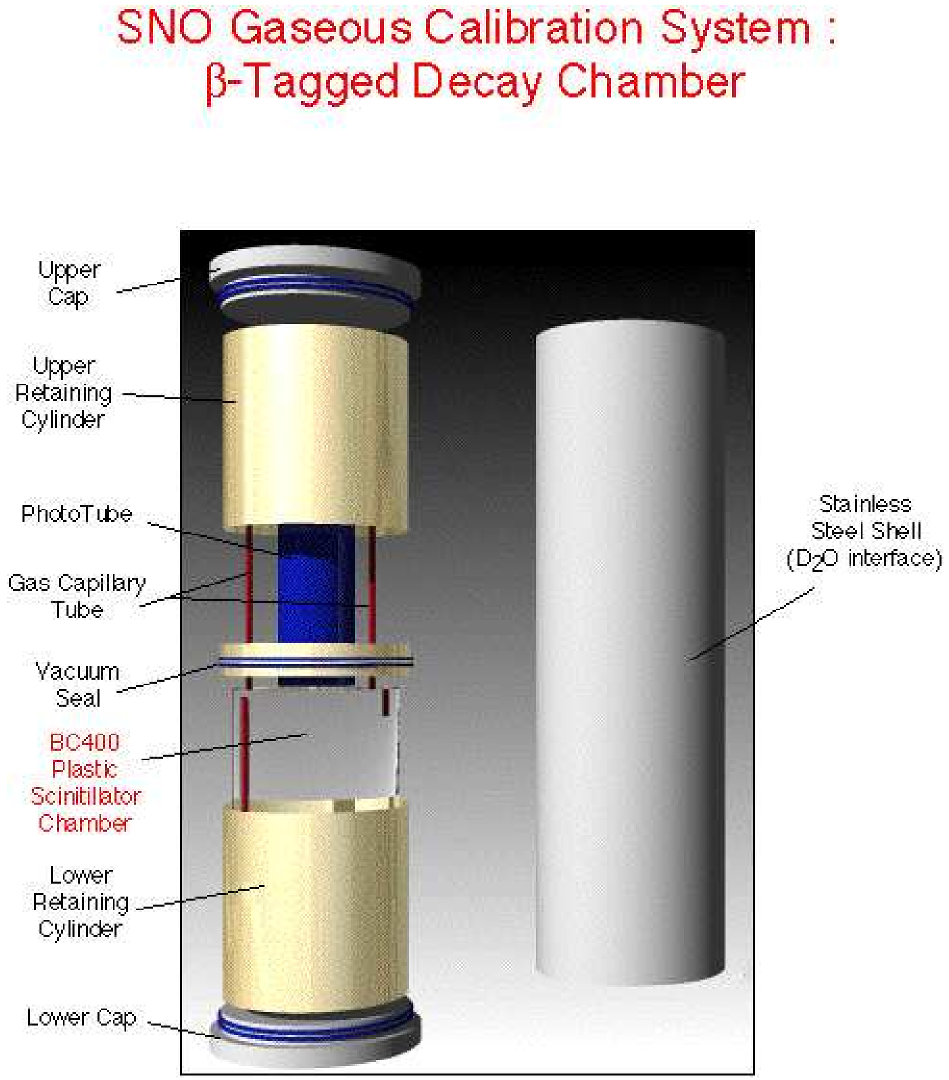

Figure 5.10: The ^{16}N decay chamber.

The outer polyethylene gas line is connected to the bottom compartment of the chamber with a Swagelok union fitting. The center teflon line continues to the bottom of the chamber. The PMT signal wire and control voltage wires for the power supply are coiled around the output gas transfer line and sent up to the deck via the 35 meter long umbilical (see Figure 5.8). On deck, the signal is sent to the SNO trigger system, and the reference voltages for the power supply to a control box placed near the universal interface.

The PMT can be connected to the SNO trigger system by several means. It can be sent directly to the Master Trigger Card (MTC) via the Trigger Utility Board (TUB) which converts the raw negative trigger pulse from the tube into an MTC compatible ECL pulse. The PMT pulse height, however, can be measured if the pulse is sent to one of SNO's specially designed PMT interface cards in one of the crates. Then triggering is done via that one channel. Alternatively the signal can be split with one end going to the TUB and the other to the PMT interface card so that triggering is via the TUB, yet signal pulse height information is retrieved via the crate channel.

The ^{16}N chamber performance has been demonstrated on many occasions, both on-line and off-line to SNO. Figure 5.11 shows the scintillator signal with ^{16}N flowing through the chamber and without. The latter corresponds to the chamber background and is equivalent to approximately 4 % of the typical ^{16}N rates. The gamma-rays from the decay chamber, as seen with a 12.7 by 12.7 cm NaI detector and a Ge detector, are shown in Figures 5.12 and 5.13, respectively. In both instances the scintillator signal was used as a gate to eliminate external backgrounds. An important observation is that, with the exception of a small peak at 1.46 MeV due to random coincidences between the scintillator triggering and environmental ^{40}K detection in the NaI detector, there are no observable γ-peaks other than those due to ^{16}N decay. These ^{16}N spectra were taken underground in the SNO laboratory. Finally, the ^{16}N chamber trigger efficiency has been measured at 95 % [98].

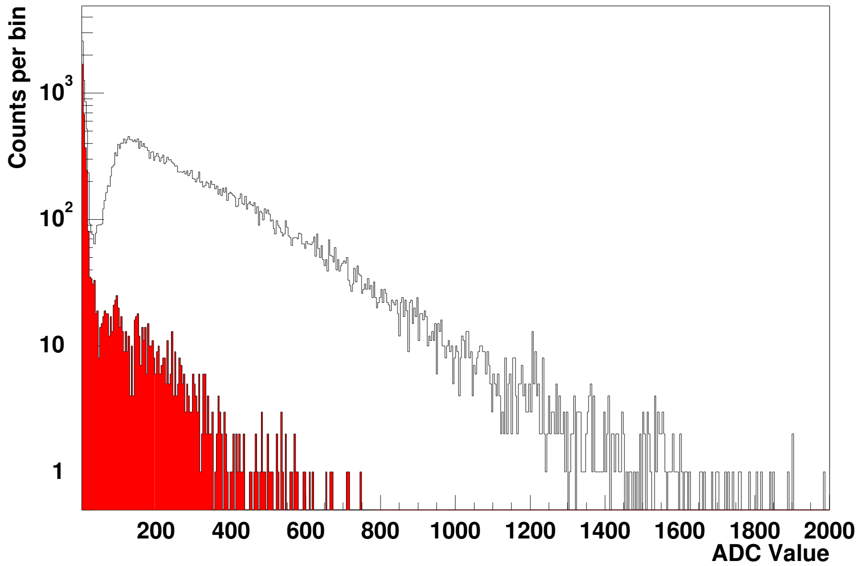

Figure 5.11: A ^{16}N chamber scintillator spectrum. The unshaded spectrum was acquired with ^{16}N production and the shaded spectrum without ^{16}N production (i.e the background spectrum).

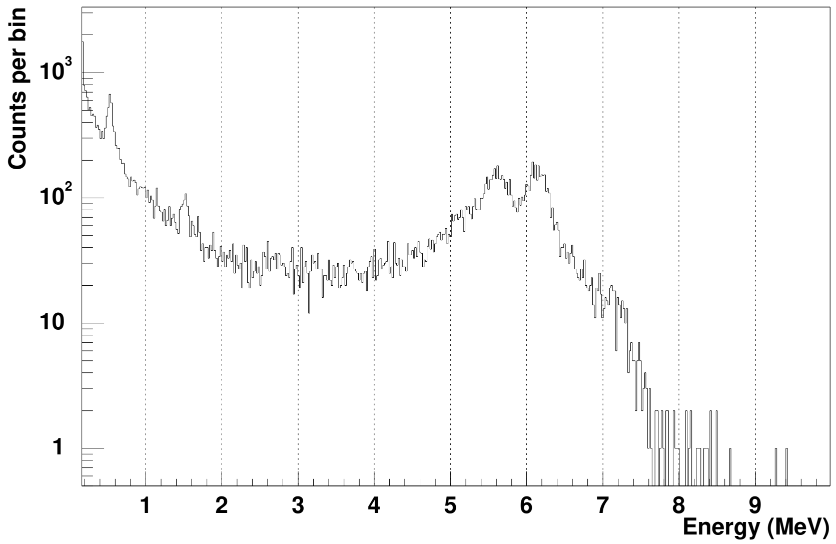

Figure 5.12: A ^{16}N γ-ray spectrum from a NaI detector. The spectrum was obtained with the NaI detector gated on the ^{16}N chamber scintillator signal.

The ^{8}Li decay chamber

The design of the ^{8}Li chamber has not yet been finalized but prototypes based on a proportional chamber design have been built and tested. Another design based on the detection of α's via scintillation is also being investigated [99].

The latest version of the proportional chamber (PC) is shown in Figure 5.14, is made of stainless steel, is 81.28 cm long, has a 2.54 cm diameter with a 0.0508 cm wall thickness, and a central stainless steel anode wire. Two end-caps are used to isolate and support the central wire, as well as feed and vent the gas stream containing aerosol. The trigger is supplied by the PC pulse but the details of how it will interface to the SNO electronics have not yet been finalized. The PC counter design requires a quench gas to work. A 5 % mix of CO_2 must therefore be added to the gas transport stream. The CO_2 would be injected downstream of the target chamber to avoid producing ^{16}N. Methods using pulse shape discrimination techniques have been tested for decay

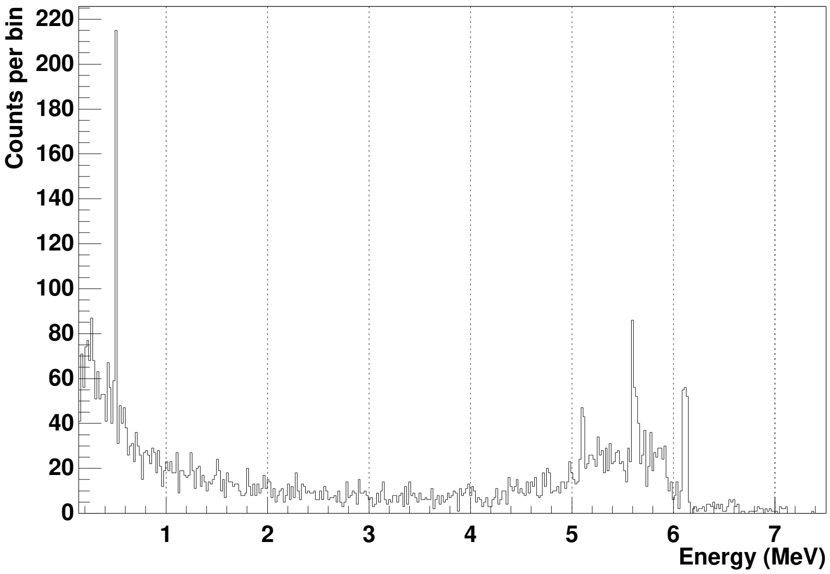

Figure 5.13: A ^{16}N γ-ray spectrum from a Ge(Li) detector. The spectrum was obtained with the Ge(Li) detector gated on the ^{16}N chamber scintillator signal. The 6.13 MeV gamma-ray and its first and second escape peaks are evident, as is the peak due to $e^{+}e^{-}$ annihilation at 511 keV.

position determination along the tube. This would benefit the position resolution calibration for SNO.

The proportional counter design has been tested with ^{8}Li at Chalk River Laboratories [100]. The configuration of the test experiment is shown in Figure 5.15. Gas flow was controlled with a very simple gas control panel. Helium gas flowed through the quartz oven tube containing the NaCl aerosol. The line following the oven was water cooled. The Helium then flowed through the target chamber followed by the decay chamber and an exhaust line. For this system, it was possible to have the PC quench gas injected downstream or upstream of the aerosol oven, or directly into the decay chamber. Both the Helium and CO_2 flow were varied using MKS gas flow controllers and the pressure upstream of the target and downstream of the chamber monitored with Bourdon pressure gauges.

An early prototype counter was built for these tests. The length of the sensitive region within the chamber tube was 1 meter and the inner diameter $\approx$ 2.5 cm. The wire used was made of 25 μm diameter stainless steel. The chamber had gas-tight O-ring-sealed end-caps for high voltage connectors and gas capillary lines. The gas from the capillary was injected directly into the sensitive region through a hole in an insulating plate (G-10) used to support the central wire. The chamber also had 5 ports placed at 5.0, 27.5, 50.0, 72.5, and 95.0 cm for a ^{241}Am calibration source producing 5.5 MeV alphas.

The position of an alpha decay in the chamber was determined by two techniques. The first technique used two-ended charge division where both ends of the wire are connected to pre-amps. The ratio of the charge difference to the charge sum is a function of position. The electronics configuration used for this technique is shown in Figure 5.16.

The results for calibration with the Americium source are shown in Figures 5.17 and 5.18. Figure 5.17 shows the charge difference/charge sum ratio for the five calibration positions, and Figure 5.18 shows a scatter plot of the charge sum versus the charge difference. The position resolution (FWHM) for the five positions are shown in Table 5.3. The results with ^{8}Li flowing

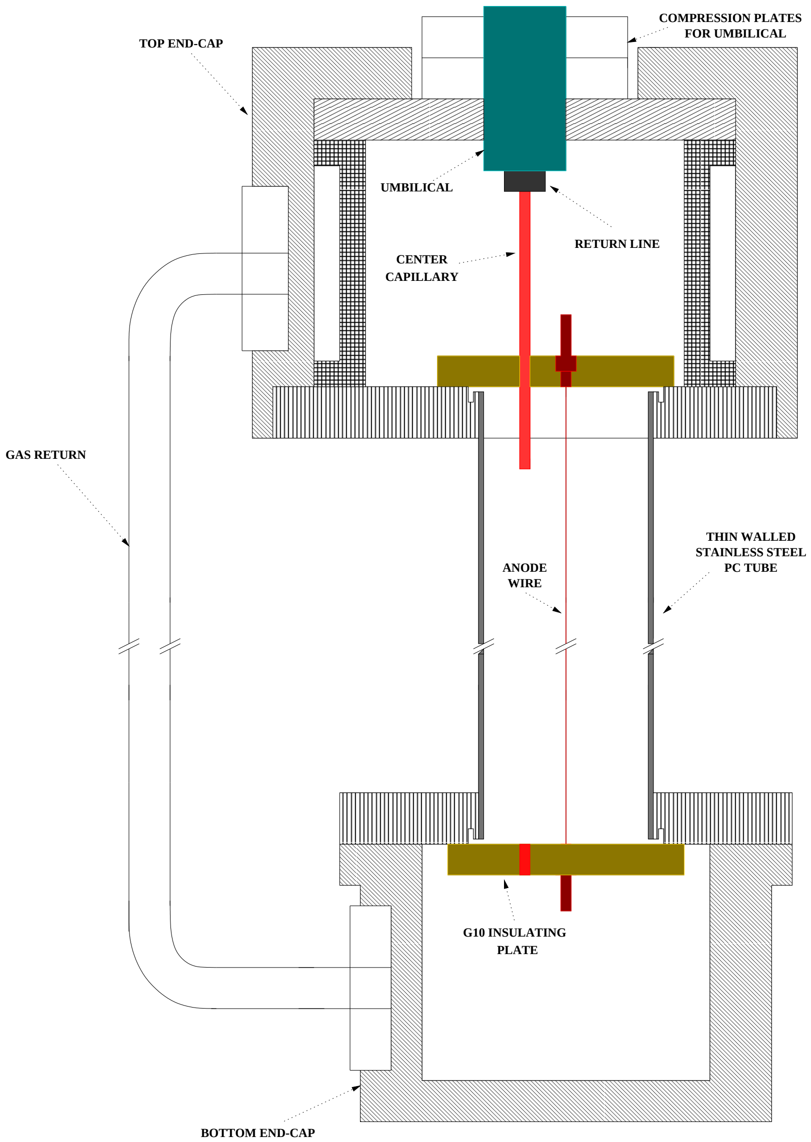

Figure 5.14: The ^{8}Li proportional counter decay chamber.

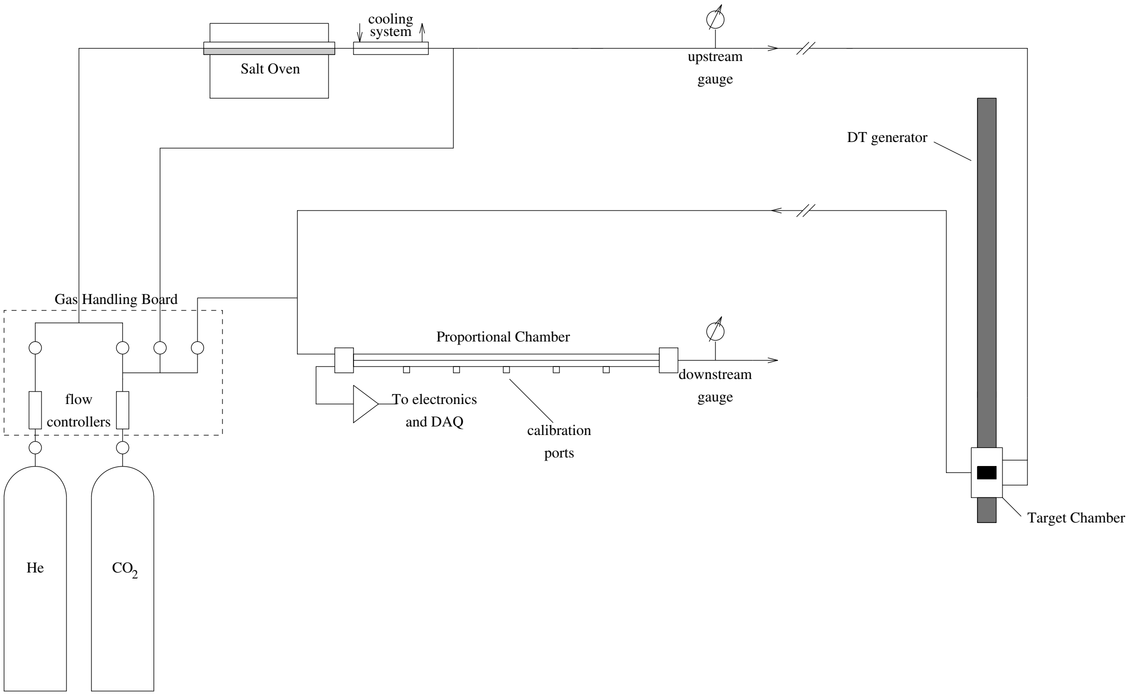

Figure 5.15: The experimental set-up for ^{8}Li tests with a proportional counter.

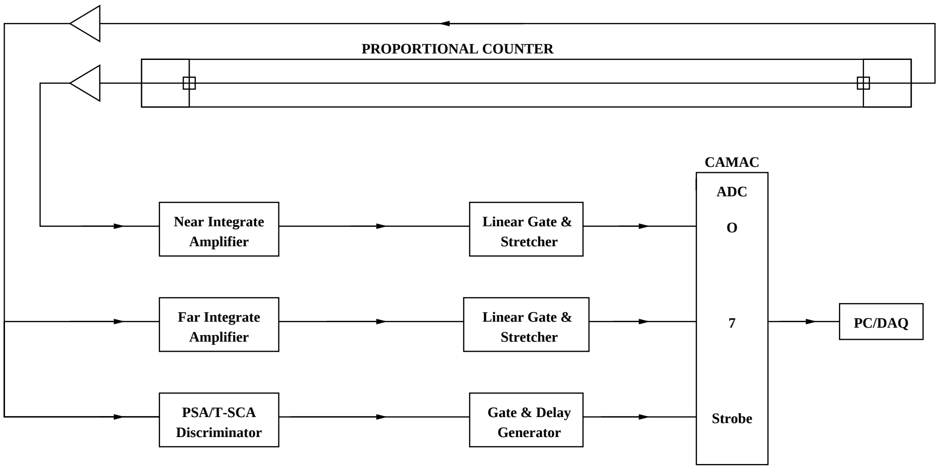

Figure 5.16: The electronics set-up for two-ended charge division with the prototype ^{8}Li proportional chamber.

Table 5.3: Position resolution (FWHM) for the ^{8}Li chamber from charge division techniques

Port	Two-ended	One-ended
1	10.5 cm	7.1 cm
2	5.4 cm	8.4 cm
3	3.1 cm	8.7 cm
4	2.6 cm	9.3 cm
5	4.0 cm	17.4 cm

through the chamber are shown in Figures 5.19 and 5.20. Figure 5.19 shows the pulse heights for the near and far end pulses. Figure 5.20 shows the reconstructed alpha decay position where the response function was determined by fitting the calibration charge ratios versus port position to a low order polynomial. The exponential-like drop in count rate versus distance is due to the fact that the transfer time across the chamber at the $\approx$ 160 cc/sec flow rate is $\approx$ 3.4 seconds which is longer than the ^{8}Li half-life of 0.83 seconds.

One-ended charge division techniques were tested as well [101]. In this instance, a pre-amp is connected to only one end of the chamber. The other end has a 2000 pF grounding capacitor attached. In this configuration, the output pulse is observed to have two components with different rise times. The amplitude of the fast component is proportional to x/L, with x the distance between the decay position and the capacitor, and L the total length of the chamber. The slow component, however, is proportional to the total charge collected and is independent of event position. By sending the pre-amp signal to two linear amplifiers with fast and slow constants, respectively, the decay position can be determined by taking the ratio of the resulting pulse heights. The electronics configuration used is shown in Figure 5.21. The calibration data is shown in Figures 5.22 and 5.23, and in Table 5.3. In this instance the position response was less linear. The polynomial fits for the response function were divided into two regions. The results with ^{8}Li flow are shown in Figures 5.24 and 5.25. Figure 5.24 shows the fast and slow pulse heights, and Figure 5.25, the reconstructed

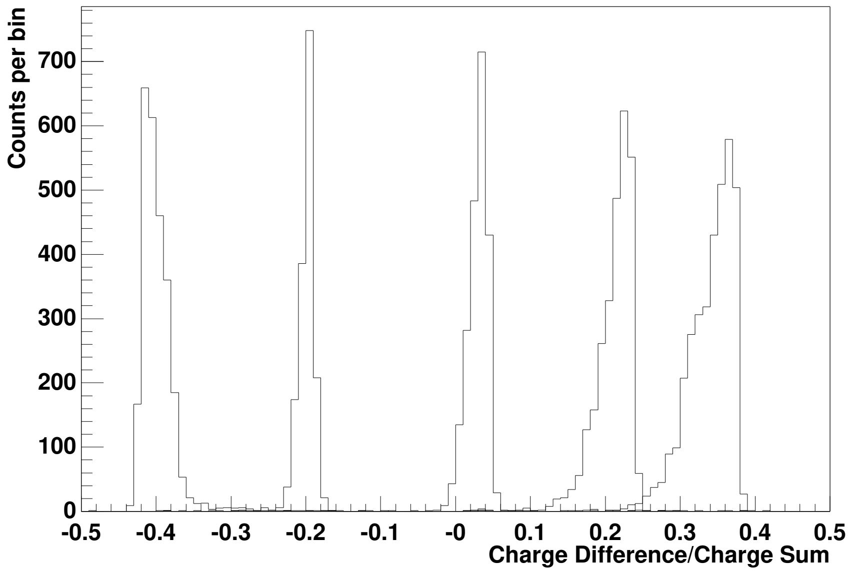

Figure 5.17: Two-ended charge division calibration with the ^{251}Am source at five positions along the chamber length.

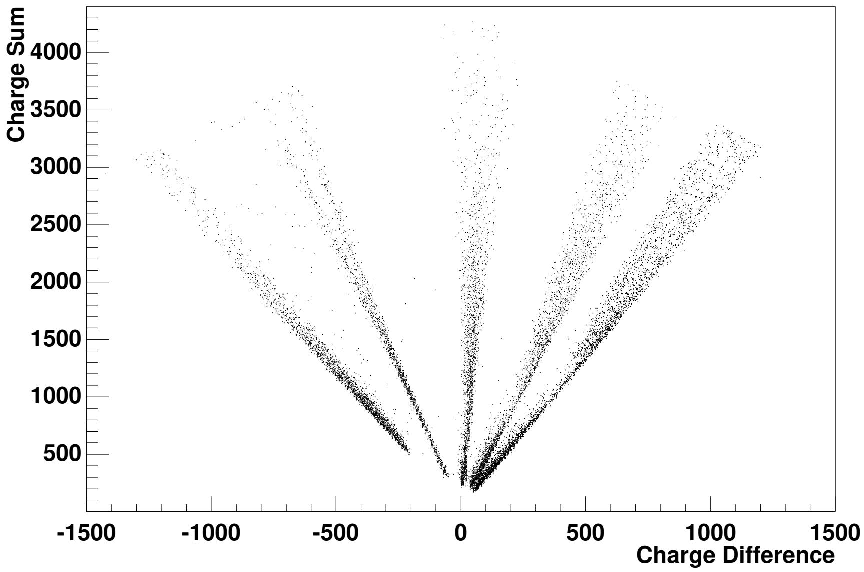

Figure 5.18: Scatter plot for two-ended charge division calibration with the ^{251}Am source at five positions along the ^{8}Li chamber length.

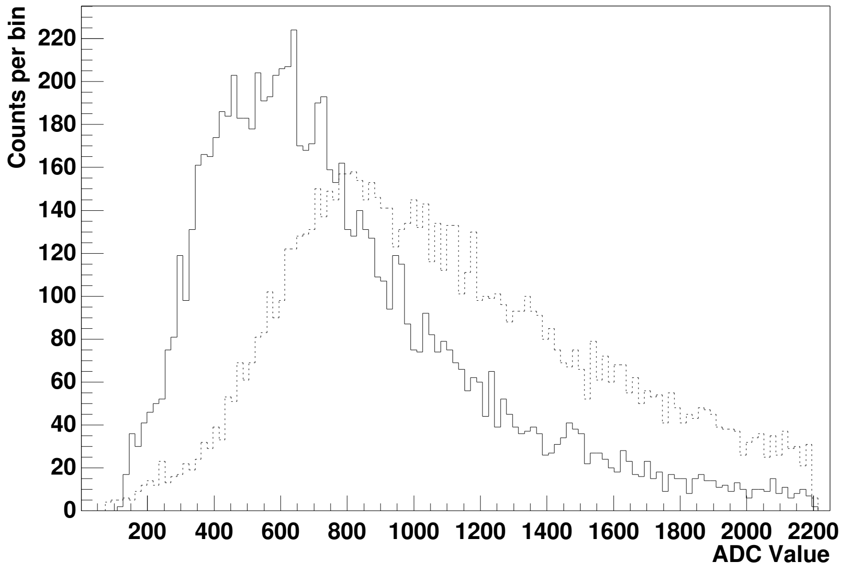

Figure 5.19: Two-ended charge division pulse heights for the near (dotted line) and far end (solid line) preamplifiers for ^{8}Li decay alphas in the prototype ^{8}Li proportional counter.

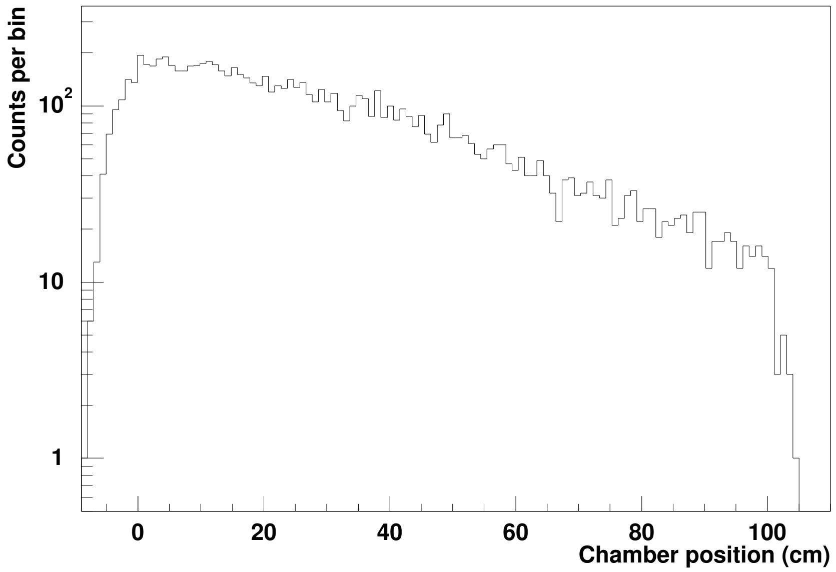

Figure 5.20: ^{8}Li decay positions determined from two-ended charge division.

position.

With the above tests it was shown that the proportional counter design could be used to trigger ^{8}Li. Position determination was demonstrated as well but the methods require further optimization. More importantly, these results provided proof of principle for ^{8}Li production and transfer. The alpha scintillation technique is now being actively investigated, but the proportional counter option has not been ruled out.

5.2.5 Status of the gas calibration systems

Presently the complete ^{16}N calibration system is underground in the SNO laboratory and has been used for calibration purposes (see chapter 7). The details of the commissioning of this system can be found in [102–104]. The ^{17}N system shares the same gas transfer lines as the ^{16}N system and therefore all that remains to be done is the installation of a cryogenic recovery system and

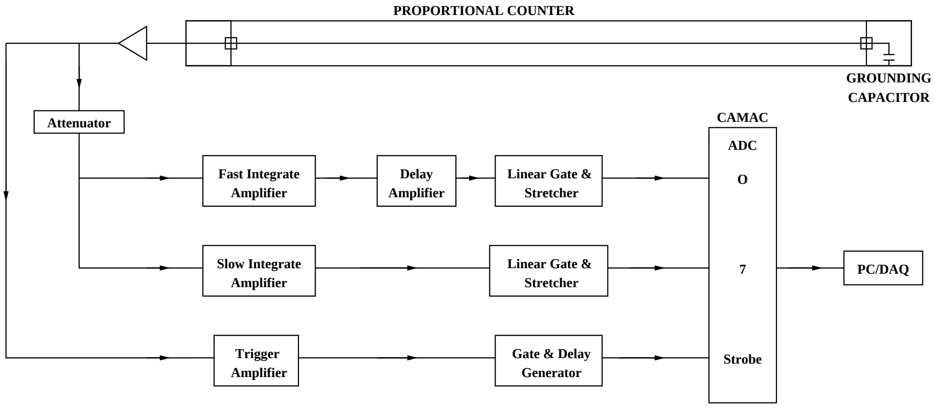

Figure 5.21: The electronics set-up for one-ended charge division with the prototype ^{8}Li proportional counter.

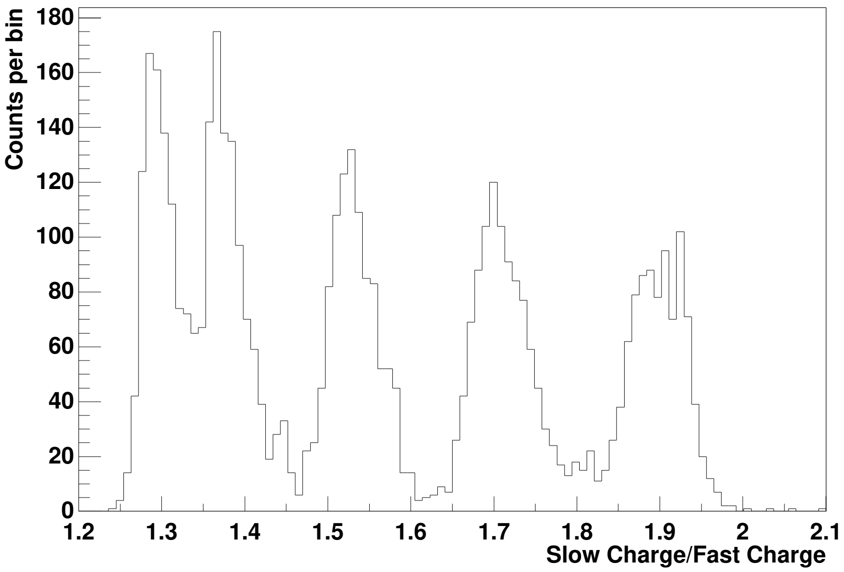

Figure 5.22: One-ended charge division calibration with the ^{251}Am source at five positions along the ^{8}Li chamber length.

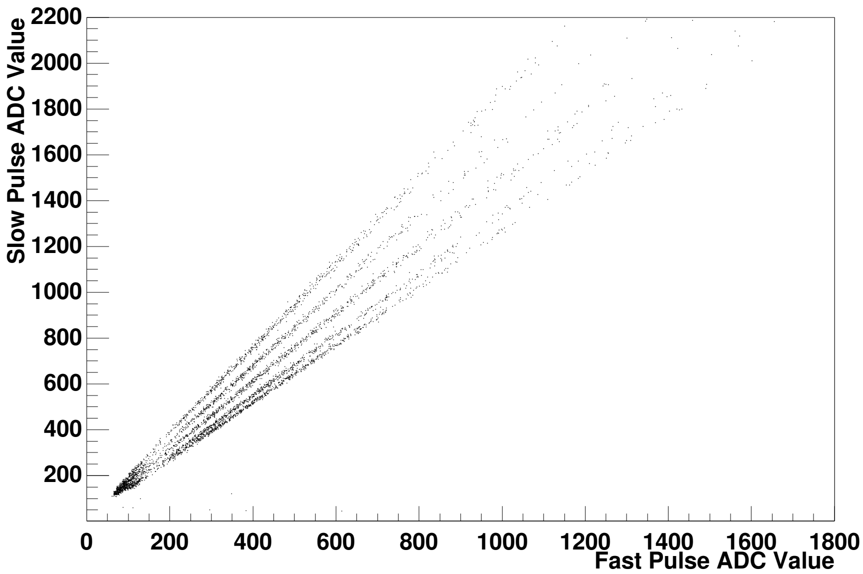

Figure 5.23: Scatter plot for one-ended charge division calibration with the ^{251}Am source at five positions along the ^{8}Li chamber length.

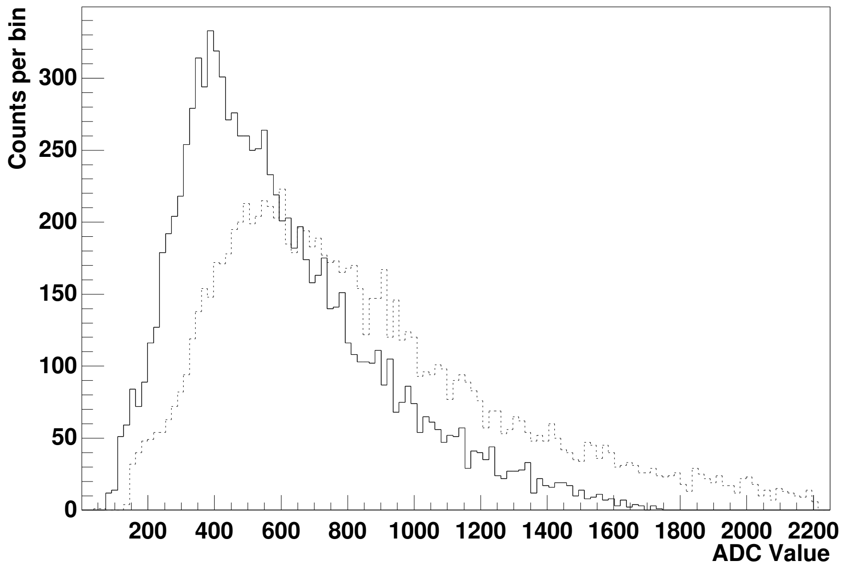

Figure 5.24: One-ended charge division pulse heights. Fast (solid line) and slow (dotted line) integrated pulse heights for one-ended charge division for ^{8}Li decay alphas are shown.

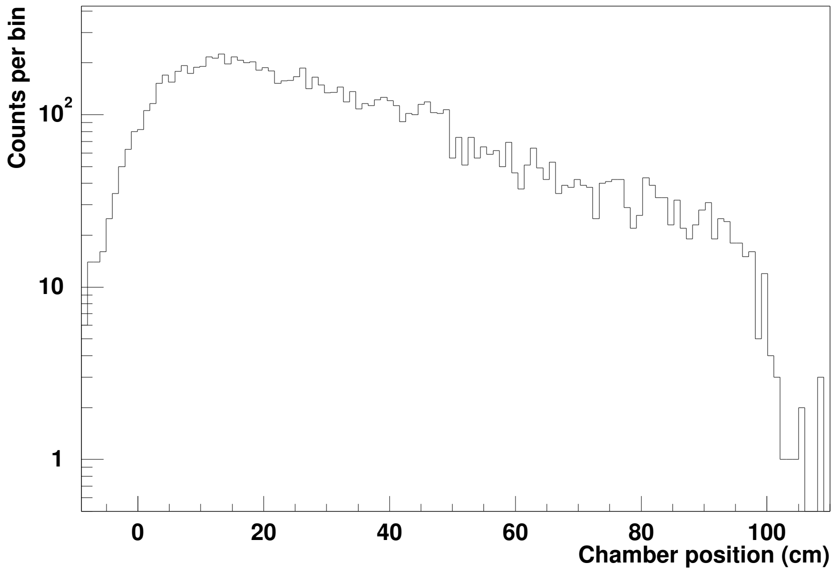

Figure 5.25: Reconstructed ^{8}Li decay positions from one-ended charge division.

a thorough system leak check. The ^{8}Li system requires the installation of the target chamber in the DT pit and the gas transfer lines. The aerosol generator must be transported and installed underground and an umbilical made. Finally a ^{8}Li decay chamber design must be finalized and approved for use in SNO.

5.3 The Radioisotope yields

In order for any of the above radioisotopes to be useful, sufficient numbers must be produced and transferred to the decay chambers. The following discusses the various efficiencies that are used to estimate the overall production yield for ^{16}N. Such calculations were performed initially to optimize the design of the gas transfer systems [105]. A detailed discussion of the yields for ^{8}Li can be found in [92]. Also presented are the results of ^{16}N yield tests with various gas and solid targets.

Table 5.4: Dimensions and constants for ^{16}N yield calculations

chamber half height (h)	3.95 cm
chamber inner radius (R_1)	2.32 cm
chamber outer radius (R_2)	5.72 cm
cross section (σ)	35 mb
gas density at 95 PsiA (ρ)	3.52 x 10^{20} cm-3
Yield per neutron (Y_n)	6.92 x 10^{-5} ^{16}N/neutron

Target yields

With the present ^{16}N system, CO_2 is used as the target for ^{16}N production. For the cylindrical geometry of the target chamber, the yield per isotropically emitted neutron in a chamber volume element as a function of r and θ coordinates is given by

$$dY_n(4\pi) = \frac{\sigma\rho}{2} d\theta dr \tag{5.2}$$

where σ is the cross-section in cm^2 (1 barn = 10^{-24} cm^2) and ρ the gas density in atoms-cm^{-3}. Integration of equation 5.2 results in the following function for the overall yield,

$$Y = \sigma\rho\left[\tfrac{h}{2}\log\left(1+\left(\tfrac{R_2}{h}\right)^2\right) - \tfrac{h}{2}\log\left(1+\left(\tfrac{R_1}{h}\right)^2\right)\right] - \sigma\rho\left[R_1\arctan\left(\tfrac{R_2}{h}\right) - R_1\arctan\left(\tfrac{R_1}{h}\right)\right]$$
$$+\sigma\rho(R_2-R_1)\left[\tfrac{\pi}{2} - \arctan\left(\tfrac{R_2}{h}\right)\right] \tag{5.3}$$

where h is the half-height of the chamber, and R_1 and R_2 are the inner and outer radii, respectively. The quantities and dimensions required to determine the yields are given in Table 5.4. For a 10^8 n s^{-1} source, one can expect over 6900 ^{16}N atoms produced per second. The yields for ^{17}N should scale with the cross-sections and the amount of target gas available.

Yield tests with fiber targets

Solid targets were also considered for ^{16}N production with the gas transfer system. Early tests with a teflon (C_2F_2) target disk where ^{16}N is produced by the (n,α) reaction on fluorine showed lower yields [89]. This was expected and was explained partly by the lower ^{19}F(n,α)^{16}N cross-section, but mostly because a large fraction of the ^{16}N recoils can not penetrate out of the solid. In order to maximize the solid target surface area, a variety of oxygen-containing and fluorine-containing fibers were tested for ^{16}N production at Chalk River Laboratories (CRL). The experimental set-up for these tests is shown in Figure 5.26. Gas flow and pressures were controlled and monitored using the present gas control board. The distance from the target to the decay chamber was 6.4 meters and was as short as possible given the location of the DT generator in the CRL shielding room. A dummy decay volume (12.7 cm by 12.7 cm cylinder) was used with a NaI detector placed in front of it for γ detection. Data was collected with a CANBERRA series 35Plus multi-channel analyzer. The list of target fibers used is given in Table 5.5. The mean ranges are for the maximum recoil energy and were calculated numerically using TRIM (Transport of Ions in Matter) [106]. A variety of transfer gases were used and the maximum recoil ranges though them were calculated using TRIM as well and are given in Table 5.6.

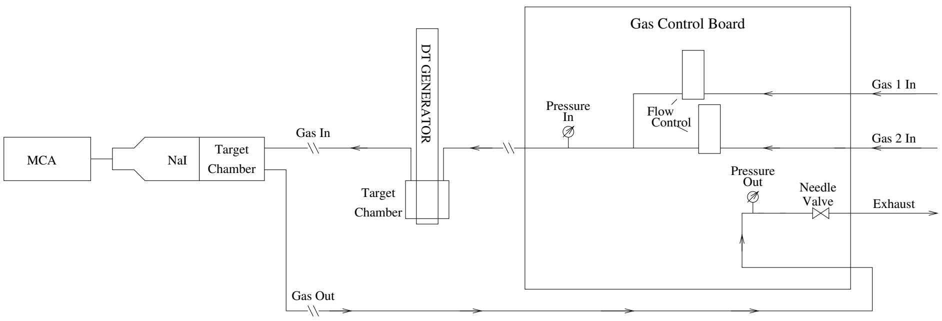

Figure 5.26: The experimental configuration for ^{16}N fiber target tests.

The results are summarized in Table 5.7 and show the NaI count rate for the 6.13 MeV γ-peak for an empty chamber and a chamber filled with quartz, cotton, viscose, and teflon. Three quartz

Table 5.5: List of ^{16}N target fibers and properties. The mean range is for the maximum recoil energy.

Material	Composition	Diameter (μm)	Mean Range (μm)
Quartz	SiO_2	4-8	2.0
Cotton	$C_6H_{10}O_5$	18	3.5
Viscose	$C_6H_{10}O_5$	9	2.6
Teflon	C_2F_2	12	3.2

Table 5.6: ^{16}N recoil ranges for various gases.

Gas	O_2	He	CO_2	N_2	Air
Range (μm)	898	4810	551	907	916

fiber samples were prepared with varying packing densities in the chamber. The target and decay chamber pressures, and the mass flow rate, were kept constant for all runs so that the flow conditions were close to identical and the difference in count rates could be attributed to differences in the target chamber production. The exceptions are the CO_2 results where the flow rates used were actually lower than the other measurements because of a faulty flow meter calibration. Corrections (shown in brackets) were calculated to compensate for the differences in residence times in the decay and target volumes at the different flow rates. Residence time calculations are discussed below. These corrections do make some assumptions about mixing in the decay volume. The yield results can be explained in terms of the amount of target available, the stopping powers of the gases, and recoils burying themselves in adjacent fibers. For example, the CO_2 and O_2 rate results are higher than the air results because air has less oxygen content per volume. The N_2 results are consistently higher than the He results, indicating a stopping power dependence. In many instances, the pure gas results (CO_2 and O_2) have higher rates than with fibers present suggesting burying of the recoils into adjacent fibers. A more detailed account of these results can be found in [107]. The

Table 5.7: Summary of ^{16}N fiber target test results. Shown are the 6.13 MeV count rates per second from the NaI detector. The CO_2 rates shown between brackets are corrected values which take into account the differences in flow conditions for these runs. The effective masses for each fiber sample is given as well.

Targets	He	He + N_2	N_2	Air	CO_2	O_2
None	-	-	0.5	-	16.8(22.5)	26.4
QuartzB(1.2 g)	1.3	1.5	2.1	7.7	17.1(22.9)	26.8
Cotton(7.5 g)	1.1	2.3	7.2	-	11.4(15.3)	7.8
QuartzA(9.8 g)	2.3	2.8	8.4	12.8	16.3(21.8)	21.8
Viscose(19.1 g)	3.8	3.9	10.7	13.4	12.8(17.1)	18.3
QuartzC(21.2 g)	1.9	-	10.6	14.6	20.9(28.0)	19.8
Teflon(20.6 g)	2.6	2.5	4.1	9.6	17.1(22.9)	24.7

main conclusion is that fiber targets are a viable option but that there is no great advantage over CO_2 gas.

Target chamber escape efficiency

To determine the efficiency for exiting the target, ϵ_{tgt}, complete mixing is assumed so the time taken for the gas to pass through the container, τ_{tgt}, is

$$\tau_{tgt} = \frac{PV}{Q} \tag{5.4}$$

where P is the chamber pressure in atmospheres, V the volume in cubic centimeters (cc) and Q the flow rate in cc/sec/Atm. While passing through the target chamber an amount of the produced gas will decay, the fraction that survives is given by

$$\epsilon_{tgt} = \frac{1}{1 + \frac{\tau_{tgt}}{\tau_{16_N}}}. \tag{5.5}$$

The target chamber volume is 678 cc, and the nominal target pressure is 6.5 Atmospheres, the nominal flow is 230 cc/sec, and so the residence time is 19.2 seconds. Given that the ^{16}N mean life is 10.28 seconds, the target chamber exit efficiency, ϵ_{tgt}, is 34.9 %.

Transfer efficiency

The transit time in the capillary tube is given by

$$\tau_{cap} = \int_0^l \frac{P(x)}{Q} A dx \tag{5.6}$$

where P(x) is the pressure along the tube length, Q is the mass flow rate, and A is capillary cross-sectional area. For ^{16}N, flow is in the turbulent regime so the average pressure between the target and decay chambers is used for P(x). The methods applied for the turbulent flow calculations were taken from [108]. It should be noted that because the flow is turbulent and is complicated by the flow through the irregular shaped pipe in the umbilical (i.e. coaxial and likely off-center), many of the calculated pressure differentials used are approximate. Empirical studies in which pressure differentials were measured across coaxial segments of pipe, however, showed agreement with calculations to within 10 %. Measurements of the pressure differentials across the present gas configuration have not been done. For the lengths and diameters given in Table 5.2, the calculated transit time to the decay chamber is $\approx$ 12.4 seconds. The fraction of radioactive gas that survives passing through the capillary is

$$\epsilon_{cap} = e^{-\frac{\tau_{cap}}{\tau_{^{16}N}}} \tag{5.7}$$

which corresponds to a 29.8 % transfer efficiency for ^{16}N.

Decay chamber efficiency

The fraction of gas that does decay in the chamber, assuming complete mixing of the gas, is given by

$$\epsilon_{dec} = \frac{1}{1 + \frac{\tau_{^{16}N}}{\tau_{dec}}}. \tag{5.8}$$

where τ_{dec} is the residence time in the decay chamber which is 18.5 seconds. The efficiency is therefore 64.2 %.

The overall efficiency

The product of the target, transfer, and decay efficiencies is $\approx$ 6.7 %. For 6920 ^{16}N atoms produced in the target chamber one would therefore expect roughly 460 ^{16}N triggers. The measured rate in the SNO system is 350 Hz (a 30 % difference in yield) and so some of the assumptions and approximations made above must therefore not be completely correct. It is quite possible, for example, that the target chamber position relative to the DT generator is not fully optimized, that not all the ^{16}N recoils range out in the target chamber, the flow calculations are off, or that there is not perfect mixing in the decay chamber. Nevertheless, the yields are more than adequate for the SNO calibration purposes.

Chapter 6

^{16}N Source Simulation and Energy Response Sensitivity

In chapter 4 the methods were outlined for energy calibration with generic monoenergetic γ-ray sources. The details of each source, however, must be considered. In the case of the ^{16}N source, the γ emission is not purely monoenergetic. Also, the interactions with the ^{16}N chamber will affect the energy output. For these reasons, a careful examination of systematic uncertainties associated with the ^{16}N branching ratios and source geometry must be made. Ultimately, these uncertainties will limit the sensitivity of the ^{16}N source for energy calibration and response verification.

The following chapter aims at studying the above systematic uncertainties and determining the overall sensitivity of the ^{16}N source for probing the energy response. The discussion begins with a description of the Monte Carlo simulation of the ^{16}N source which is designed to include any known systematic effects due to the decay branches and source chamber. The Monte Carlo is then used to illustrate various properties of the source energy and NHIT output. This is followed by a discussion of how the various systematic uncertainties in the absolute energy calibration are determined. An estimate is made of the overall sensitivity of the ^{16}N source for energy calibration. Finally a short discussion of the possibility of unknown systematic effects is given.

Table 6.1: Branching ratios and particle energies used in the ^{16}N simulation. The end-point values are given for the betas.

^{16}O Energy Levels (MeV)	Branching Ratio (%)	β (MeV)	γ (MeV)	γ (MeV)
0.0	28.0	10.4190		
6129.89	66.2	4.2891	6.1286	
7116.85	4.8	3.3022	7.1152	
8871.9	0.076	1.5471	8.8693	
8871.9	0.13	1.5471	2.8222	6.0482
8871.9	0.82	1.5471	2.7415	6.1286
8871.9	0.038	1.5417	1.9544	6.9155
8871.9	0.121	1.5417	1.7549	7.1152

6.1 The ^{16}N Monte Carlo

In addition to simulating neutrino events, the SNOMAN Monte Carlo is also designed to simulate events from calibration devices. For ^{16}N, the Monte Carlo simulates beta and gamma production, source triggering, β and γ interactions with the chamber, and finally Čerenkov light generation and detection in the SNO detector.

The branching ratios and energies for gammas and betas used in the Monte Carlo are taken from evaluations given in the Table of Isotopes (see Figure 5.1). Only the main branches are used, and are listed in Table 6.1. Inclusion of the other branches would have negligible effects.

The Monte Carlo simulates a trigger for the source in the same manner as the trigger for the real detector. It can be triggered with an NHIT trigger or via a calibration trigger. The calibration trigger includes the β detection with the chamber scintillator. The EGS4 determined energy deposition in the scintillator is used as a signal. The simulation also includes the time off-set and width of the trigger pulse, the gain of the trigger circuit, and the trigger channel discriminator setting.

Simulation of β and γ interactions with the source chamber are done using the EGS4 processors in SNOMAN. Various properties and observables associated with these interactions are discussed in section 6.2. Accurate simulation of these interactions requires that the details of the source geometry be included. The chamber components, their dimensions, and the medium used in the Monte Carlo are listed in Table 6.2. In the case of the scintillator, acrylic is used in place of BC400 because their properties are very similar and BC400 is not available as a media in SNOMAN. For the same reason, air is used in place of CO_2 in the decay volume. Finer details like the PMT power supply and the gas line fittings are not included and should not affect the final result. The thin aluminum sleeves used to maintain the distance between the chamber plates are, however, also not included in the default Monte Carlo but might potentially have an impact. The geometry of the source chamber was verified by simulating neutrino generation in various parts of the chamber and noting the EGS4 media boundary crossing vertices. The result is shown in Figure 6.1.

The manipulator weight which is used to couple the ^{16}N source chamber to the manipulator system is modeled as a 3.2 cm outer radius, 1.0 cm inner radius, 26.4 cm long annulus made of stainless steel. The annulus has 2 mm thick walls and the interior is filled with air for the ^{16}N source. The true manipulator weight geometry differs only slightly from the Monte Carlo having an attachment flange at the top and four small attachment screws at the bottom. The umbilical is modeled as a cylindrical tube with a 0.9 cm outer radius and a 0.5 cm inner radius. The tube is modeled as polyethylene, and the inner volume as air. The true umbilical is made of an outer silicone jacket with an inner polyethylene core, but silicone is not available as a medium. These differences should have absolutely no impact. The only notable component missing in the Monte Carlo is the coupling between the manipulator weight and the chamber. The coupling is made of stainless steel, is cylindrical, has the same diameter as the chamber, and adds 7.62 cm to the chamber's overall length. The coupling has 8 oblong holes, each 5.715 cm long and 2.54 cm wide. The purpose of the these holes was for mounting small LEDs for aiding in the source positioning. Because of the complexity of the geometry, it is not modeled in the Monte Carlo. It is, however,

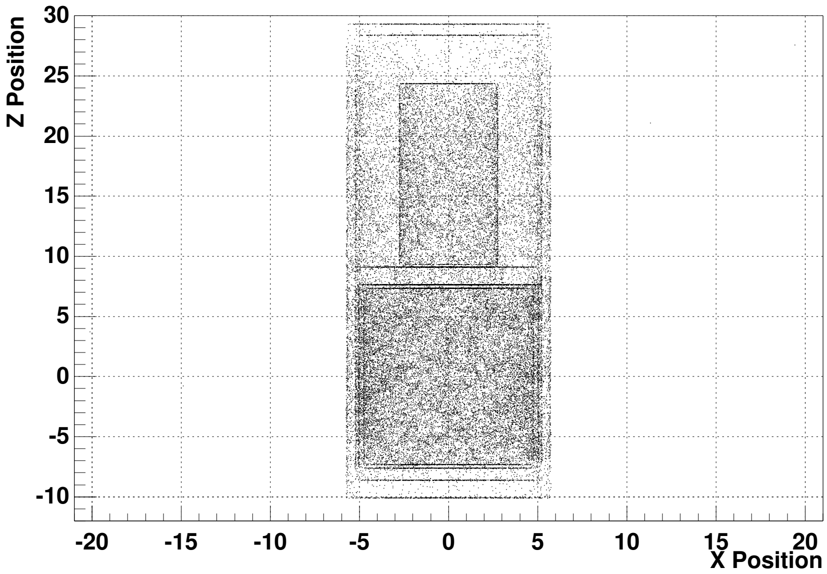

Figure 6.1: Neutrino crossing vertices for ^{16}N geometry verification. Shown are the EGS4 boundary crossing vertices as a function of X and Z coordinates (in cm) for neutrinos produced at various positions within the chamber. All the chamber features that were input into the Monte Carlo are evident. The decay gas volume is centered at X=0 and Z=0.

Table 6.2: List of chamber components used in the SNOMAN Monte Carlo. All the components are cylindrical. Given are the radii, half height, and vertical off-set with respect to the reference position. Here the reference position is given as the center of the decay volume. The measurements are all in cm.

Component	Material	Radius	Half Height	Vertical Offset
Outer container	Stainless steel	5.715	19.685	9.60625
Chamber divider ring	Stainless steel	5.239	18.495	9.88
Optical coupling between chambers	Acrylic	3.048	0.75225	8.37225
Gap between scintillator and can	Air	5.239	8.1175	-0.4975
Plastic scintillator	Acrylic	5.08	7.62	0.0
Decay volume within scintillator	Air	4.78	7.32	0.0
Upper chamber instrument volume	Air	5.239	9.625	18.7495
The trigger PMT (outside)	Aluminum	2.771	7.62	16.7445
The trigger PMT (inside)	Vacuum	2.571	7.42	16.7445

sufficiently distant from the decay volume that its omission should have little impact.

Treatment of the Čerenkov light production, propagation, and detection, is the same as would be used in simulating neutrino events in the detector. The most up-to-date detector parameters from optical calibrations and other measurements are therefore used and include

- D_2O, acrylic, and H_2O absorption coefficients.
- Optical scattering, and reflection coefficients.
- PMT thresholds and relative efficiencies.
- Models of the detector noise.
- The absolute PMT collection efficiency.

In the discussions below, the best estimates of the above parameters are used. A listing of the main parameters is given in Table 6.3. The factor used to scale the theoretical calculation of Rayleigh scattering is based on earlier experiments on scattering and absorption of light in D_2O by Boivin et al [109]. It should be noted that all of these estimates are based on off-line measurements and will likely change a bit after a full optical calibration of the detector is complete.

6.2 The ^{16}N source properties

The Monte Carlo is used to reproduce the ^{16}N source NHIT distribution which is used for the comparison to data in the energy calibration. The Monte Carlo can also be used to study the various ^{16}N source properties which distinguish it from the ideal monoenergetic γ-ray point source. Such an understanding is required if estimates are to be made of systematic uncertainties in the energy calibration due to source properties.

The main features which distinguish the ^{16}N source from the ideal monoenergetic source are

- its decay scheme,

and

- the chamber geometry.

The primary decay scheme branching ratios along with the particle emission energies were given in Table 6.1. The main gamma-ray contribution is the 6.13 MeV γ, but the 7.1 MeV γ is also significant. Associated with each of these γ's is a β-ray. Finally, there is an important branch which β-decays directly to the ground state. The design goal of the chamber was to block the β's from exiting into the D_2O, yet permit the γ's to exit with minimal energy loss. Both goals could not be fully realized and therefore a small amount of β energy will be deposited in the D_2O and some of the γ's will be affected by interactions with the chamber.

Table 6.3: List of input parameters used in the Monte Carlo. These are the best estimates based on off-line measurements. Eventually the parameters will be determined via optical and energy calibration.

Parameter	Input Values
D_2O Absorption Coefficients (254nm 313 nm, 366 nm, 406 nm, 436 nm, 548 nm, 578 nm)	In cm^{-1} 1.0e-5, 1.0e-5, 1.0e-5, 1.0e-5, 1.0e-5, 1.0e-5, 1.0e-5
H_2O Absorption Coefficients (250 nm, 350 nm, 400 nm, 450 nm, 500 nm, 548 nm, 578 nm)	In cm^{-1} 1.0e-5, 1.0e-5, 1.3e-5, 6.0e-5, 2.0e-4, 5.8e-4, 9.2e-4
Acrylic Extinction Coefficients (300 nm, 320 nm, 340 nm, 360 nm, 380 nm, 420 nm, 440 nm, 500 nm, 600 nm)	In cm^{-1} 0.490, 0.180, 0.07, 0.04, 0.02, 0.01, 0.005, 0.005, 0.005
Rayleigh Scattering Scaling Factor	 2
Overall energy scale PMT Quantum Efficiency PMT collection Efficiency	 Peak of 23.6 % at 430 nm 55 %
PMT Noise rate	0.5 kHz

To study the energy output of the ^{16}N source, the energy deposition in D_2O was determined using the EGS4 entries in the SNOMAN Monte Carlo data structure. The result is shown in Figure 6.2. The peaks in the upper panel distribution (γ branches) include the 6.13, 7.12, and 8.87 MeV branches. These peaks correspond to the case where the full γ-ray energy is deposited in the D_2O. The tails associated with the γ-ray peaks are due to Compton scattering in the walls of the source chamber. Of the gamma-ray events that produced Čerenkov light, 18 % will have energy taken away via Compton scattering in the chamber steel. The lower panel shows the ground state β contribution to the D_2O energy deposition. In this case, the β's were not fully attenuated by the stainless steel, or because of the high Z of the steel, experienced energy loss via radiation (Bremsstrahlung). Of the ground state beta decays, 7.25 % deposit enough energy into the detector for Čerenkov light to be produced.

The resulting NHIT distribution from the Monte Carlo is shown in Figures 6.3 and 6.4. In Figure 6.3 the ^{16}N source is modeled with zero PMT dark noise in order to illustrate the low NHIT Compton scattering and ground state β contributions where Čerenkov light was produced. Clearly many of these latter contributions can be eliminated if events with NHIT < 10 are cut in the data reduction. Of events which registered more than 10 hits, 14 % are associated with Compton scattering in the chamber, and only about 0.75 % with ground state betas. Also shown in Figure 6.3 is the NHIT distribution for pure, chamber-less, 6.13 MeV γ-rays. The distributions are very similar in the gamma-peak range except for a slight difference in width.

Figure 6.4 shows the NHIT spectrum if dark PMT noise (0.5 KHz) is added to the Monte Carlo. In this case there are many "false triggers" in which no Čerenkov light is produced. This is mainly due to ground state β's which were completely absorbed in the stainless steel. There is also a contribution due to Compton scattering or pair production processes in which the full energy (above the Čerenkov threshold) of the γ-rays were absorbed in the chamber (about 15 %). Finally, there will be false triggers associated with photodisintegration of deuterium because the 6.25 MeV γ's produced from neutrons occur much later than the chamber scintillator trigger. These events can be removed from the subsequent analysis if the requirement is made that an event reconstruct

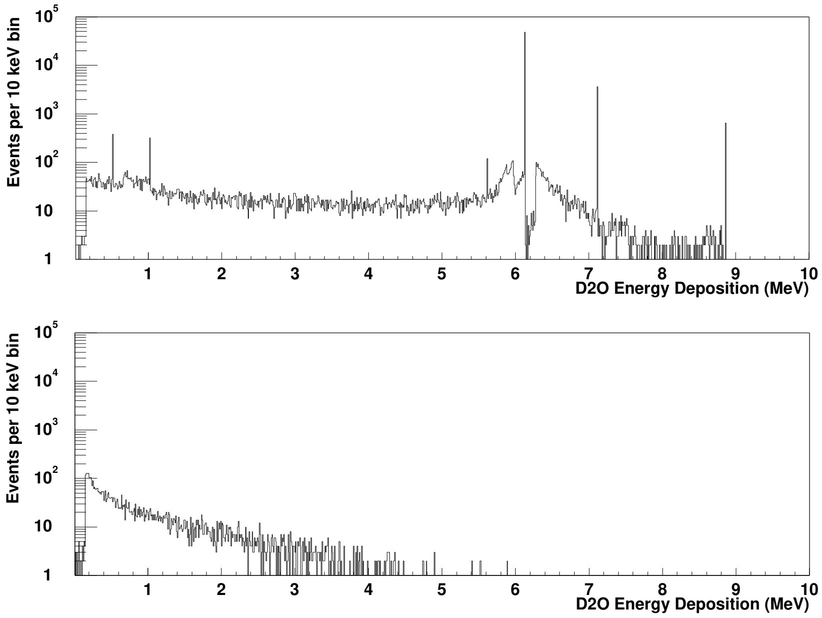

Figure 6.2: Energy output of the ^{16}N source in D_2O. Shown is the energy deposition in the D_2O due to gamma branch ^{16}N decays (upper panel) and those due to the ground state betas (lower panel). Distributions are from the Monte Carlo. The apparent deficit of events with energy deposition above 6.13 MeV in the upper panel is an EGS4 artifact. The deficit is caused because the Bremsstrahlung gamma-rays which contibute additional energy are not tracked out into the D_2O if they are below the EGS4 tracking threshold for gamma-rays which is set to just below the Čerenkov threshold (150 keV).

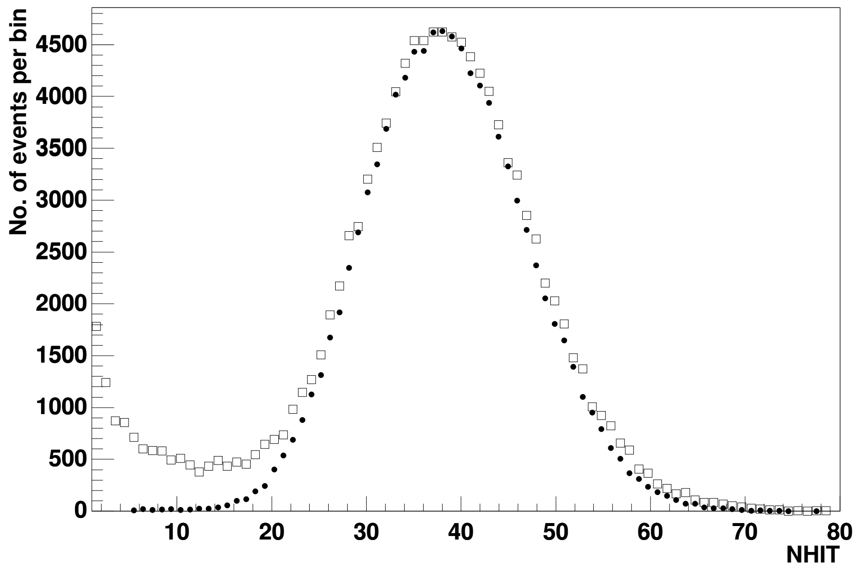

Figure 6.3: NHIT distributions for 6.13 MeV gamma-ray (dots) and ^{16}N (open squares) sources. Both distributions were calculated with the SNOMAN Monte Carlo.

within the D_2O volume (see Figure 6.4).

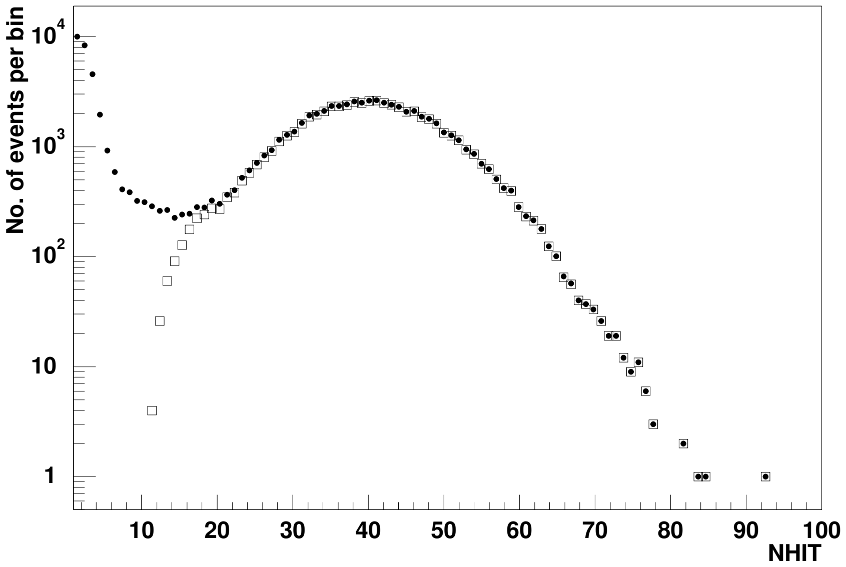

Figure 6.4: ^{16}N NHIT spectrum with noise added. The complete NHIT spectrum, including PMT dark noise, is shown (solid dots). The ground state beta false triggers are evident at lower NHIT values. These events, however, can be removed by cutting on NHIT or the requirement that the events reconstruct within the D_2O volume (open squares). Both distributions are from Monte Carlo simulations.

A study of the impact of the various chamber and decay scheme properties on the energy scale calibration is required. The impact of the ^{16}N source properties on the measured mean of the NHIT distribution was studied by switching off various components in the Monte Carlo and comparing the results to the most complete simulation. This included switching off PMT dark noise, interactions in the chamber, the β's coincident with the γ's, the ground state β's, and photodisintegration. In the case where interactions in the chamber were eliminated, the chamber media were switched to D_2O. For each Monte Carlo, the source was placed at the center of the detector, the PMT dark

Table 6.4: Monte Carlo studies of source properties. Shown are the mean NHIT values of the ^{16}N Monte Carlo with various of the source properties switched on ($\surd$) or off (-). The errors are statistical.

γ's	Photodisin.	Grd. State β's	Coincident β's	Chamber	Noise	Mean
6.13 MeV	-	-	-	-		39.07±0.03
6.13 MeV	-	-	-	-	$\surd$	40.35±0.04
^{16}N	-	-	-	-	$\surd$	41.26±0.03
^{16}N	-	-	-	$\surd$	$\surd$	40.12±0.04
^{16}N	-	-	$\surd$	$\surd$	$\surd$	40.16±0.04
^{16}N	-	$\surd$	$\surd$	$\surd$	$\surd$	40.08±0.04
^{16}N	$\surd$	$\surd$	$\surd$	$\surd$	$\surd$	40.04±0.04

noise rate was set at 0.5 KHz, and the means were determined only for events which reconstructed within the D_2O volume. The results are summarized in Table 6.4. The results first indicate that adding PMT noise at the expected rates will shift the mean NHIT value for the pure 6.1 MeV gamma ray case by roughly 3 %. Including the other decay gammas will further shift the mean up by 2.3 %. Interaction of the gammas with the chamber walls, however, will shift the mean back down by 2.8 %. The impact of the β's is negligible, as is photodisintegration. Given that the effects of certain source properties are non-negligible (above the percent level), a further discussion of how uncertainties in the ^{16}N source properties are determined, along with the effect on the overall systematic uncertainty in the energy response determination, is required. This is discussed in the following section.

6.3 Determination of the ^{16}N source systematic uncertainties

Given that there are uncertainties associated with the ^{16}N source properties, their impact on the energy calibration must be assessed. This requires that

- the proportionality constants which relate changes in energy scale to changes in source properties be determined,

and

- uncertainties of the source properties must be determined.

In the absolute energy scale determination, NHIT distributions from Monte Carlo simulation are compared to actual ^{16}N data. Ultimately the comparison will be done via a chi-squared comparison of the NHIT binned Monte Carlo and experimental results. For the analysis in chapter 7 and the study of the systematic uncertainties below, however, an approximate function is used to fit both distributions for the comparison. The following therefore first presents the approximate function along with its fit parameters. Estimates of the systematic uncertainties associated with the fit function itself are discussed. This is followed by the discussion of the proportionality constants, and then estimates of the source property uncertainties. The overall systematic uncertainty is then calculated.

6.3.1 Theoretical fit function for the energy scale analysis

If the source were truly monoenergetic, both experimental and Monte Carlo distributions could be approximated by Gaussians. For the ^{16}N source, because of the decay scheme and chamber effects, the Gaussian approximation will no longer hold. However, a good approximation is to fit the distribution to two Gaussians weighted according to the branching ratios for the 6.13 MeV and 7.12 MeV γ contributions. This fit function has the form

$$F(NHIT) = C\left[\frac{B_1}{\sigma_E}e^{-\frac{1}{2}\left(\frac{NHIT-Noise-(E_1-A)\beta_E}{\sigma_E}\right)^2} + \frac{B_2}{\sqrt{E_2/E_1}\sigma_E}e^{-\frac{1}{2}\left(\frac{NHIT-Noise-(E_2-A)\beta_E}{\sqrt{E_2/E_1}\sigma_E}\right)^2}\right] \quad (6.1)$$

with B_i and E_i, the main branching ratios and energies (6.13 and 7.12 MeV) for ^{16}N decay. The factor A can be fixed to take into account the off-set in energy response due to the Čerenkov energy threshold. A and $Noise$ are used in the fit so that the β_E value corresponds roughly to the energy scale in NHITs per MeV. Use of A and $Noise$ should have no effect on the quality of the fit. In the fit, only the three parameters β_E, σ_E, and C are allowed to vary. β_E is a measure of the energy scale but is only approximately equivalent to the true NHITs per MeV value because of the chamber effects. σ_E is a measure of the energy resolution, and C is an overall normalization factor. The width for the 7.12 MeV contribution is assumed to be related to that of the 6.13 MeV contribution according to $\sigma_E(7.12MeV) = \sqrt{E_2/E_1} \cdot \sigma_E(6.13MeV)$. To minimize the effect of Compton scattering and the additional γ-branches, only the NHIT range near the γ-peak is used in the fit and only events which reconstruct within the D_2O volume are included. The fit range is symmetric about the peak value and is chosen so as to minimize the χ^2 value. Figure 6.5 illustrates this fit to the ^{16}N Monte Carlo distribution with 0.5 KHz noise added. The χ^2 value of the fit (1.53 per degree of freedom) is a little high because the function is only approximate and does not include factors for the chamber interactions. The function is, however, sufficient for a preliminary analysis and the study of the source systematics.

The systematic uncertainties associated with the fit function itself must be considered. Because the NHIT distribution used in the fit only has events which reconstruct, the dependences on the event reconstruction algorithms should be assessed. A detailed study of these dependences has not been included here but would consist of repeating the fit exercise for NHIT distributions from all the various reconstruction algorithms. In addition, for each algorithm, the various inputs used such as the time acceptance window widths would be varied. The impact of the NHIT ranges used in the fit were, however, studied and the results presented in Table 6.5. Here, the NHIT range width used was varied from 2.8 to 5.2 times the RMS (Root Mean Square deviation) of the distribution. The best fit corresponded to a NHIT range equal to four times the RMS. The maximum deviation from the best solution was 0.18 % in the β_E determination. If the requirement that the event position reconstructs is removed, the β_E parameter for the 4 time RMS range is shifted by 0.23 %. In the analysis presented in chapter 7, and likely in any future SNO energy scale analysis, an event reconstruction requirement will be applied. It is very likely that uncertainties associated with this reconstruction requirement can be made to be quite small, but to be conservative the 0.23 % value

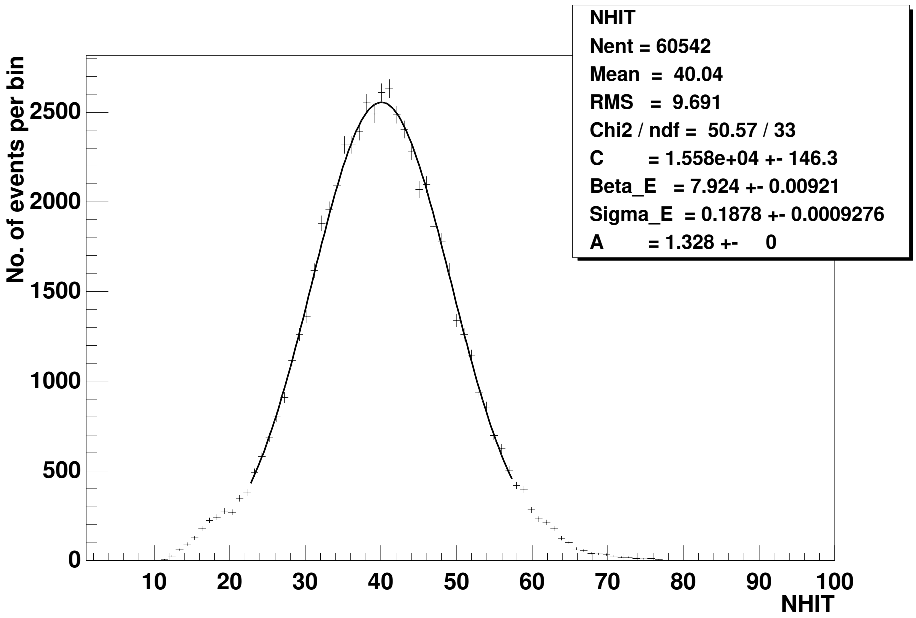

Figure 6.5: Energy scale fit (equation 6.1) to the ^{16}N Monte Carlo. Events were required to fit within the D_2O volume.

Table 6.5: Energy fit function dependence on NHIT range. Shown are the χ^2 values and percent shift in β_E values due to changes in the NHIT fit range. This is shown for data with and without a reconstruction requirement. The constant C_{RMS} is the multiplicative factor for the width of the NHIT fit range. The width is defined as C_{RMS} times the RMS of the reconstructed event NHIT spectrum.

C_{RMS}	With Cut χ^2/dof	With Cut $\Delta\beta_E/\beta_E$ %	No Cut χ^2/dof	No Cut $\Delta\beta_E/\beta_E$ %
2.8	1.83	-0.13	1.86	-0.29
3.2	1.68	-0.08	1.73	-0.25
3.6	1.53	-0.04	1.59	-0.23
4.0	1.75	0	1.87	-0.23
4.4	2.70	-0.09	3.53	-0.35
4.8	4.22	-0.13	6.54	-0.44
5.2	4.40	-0.18	10.09	-0.57

corresponding to the no-cut case with $C_{RMS} = 3.6$ to 4 is used as an uncertainty in the subsequent analyses.

6.3.2 Determination of the proportionality constants for the energy scale uncertainties

The proportionality constants associated with changes in the chamber properties were determined by fitting the parameter β_E using the function 6.1 for multiple Monte Carlo simulations where the various source properties were either switched off or varied. The effect of Compton scattering in the stainless steel was studied by dividing a 100 000 event Monte Carlo data-set into two subset categories. The first category consisted of only events in which the full energy of the ^{16}N decay γ's was deposited in the D_2O, and the second category consisted of only events in which

Table 6.6: Impact of various uncertainties on the measure of the energy scale factor, S_{Energy}. Shown are the partial derivatives of the β_E factor as a function of the uncertain quantities , X_i. Also shown are conservative estimates for these uncertainties, ΔX_i and their effect on the energy scaling parameter, ΔS_i.

X_i	$\frac{1}{\beta_E}\frac{\partial \beta_E}{\partial X_i}$	ΔX_i (%)	ΔS_i (%)
The ratio of the 7.12 MeV to 6.13 MeV branches	0.011	11	0.12
The fraction of events which interact with the chamber wall	0.011	30	0.33
The measured detector noise rates	0.03	1	0.03

Compton scattering occurred in the chamber. NHIT distributions could then be reconstructed by scaling the Compton scattering contribution. A similar procedure was used to vary the relative branching ratios (6.13 and 7.12 MeV). Monte Carlo simulations with varying noise rates were done as well. The results are summarized in Table 6.6 where the variations in β_E with changes in the parameters, X_i, are represented by the partial differentials $\partial\beta_E/\partial X_i$. The partial differentials are divided by the β_E value for the most complete Monte Carlo so that multiplying it by the property uncertainty (ΔX_i) gives the uncertainty in the energy scale determination (ΔS_i). The slopes associated with the beta contributions were shown to be negligible and therefore are not listed

6.3.3 The source property uncertainties

The source property uncertainties (also summarized in Table 6.6) are either extracted from the literature or estimates were made based on observations in the data. In SNO, the mean detector noise rate can be measured to great accuracy using PGT triggers. In the experiments discussed in chapter 7, PGT triggers were set at a 5 Hz rate and a typical ^{16}N run was of an hour's duration. For the accumulated statistics, the error in the mean noise rate determination is therefore roughly a percent. The uncertainty in the ratio of the 6.13 to 7.12 MeV gamma-contributions is taken from the table of isotopes evaluations. The branching ratios for beta decay to the excited states of oxygen including uncertainties are 66.2±0.45 for decay to the 6.13 MeV state and 4.8±0.51 for decay to the 7.12 MeV state. This corresponds to an uncertainty in the beta decay branching ratios of 11 %. There are a few minor branches which include 6.13 and 7.12 MeV γ's in the subsequent cascade of decays to the ground state of oxygen (see Table 6.1), but the uncertainties contributed by these are small in comparison to the uncertainties in the β branching ratios. Therefore the 11 % value calculated above is used for the uncertainty in ratio of the 6.13 and 7.12 MeV gamma-contributions. Uncertainties in the thickness of the various ^{16}N chamber components that are modeled in the Monte Carlo are negligible. Details of the source geometry that may be missing in the Monte Carlo, however, would have an effect on the fraction of events which Compton scatter in the chamber steel. Limits on the uncertainties in the Compton scattering contribution are therefore obtained by comparing the lower NHIT component of the experimental NHIT distribution to that determined via the Monte Carlo simulation. The distributions for the fraction of reconstructed events as a function of measured angle with respect to the Z axis can be studied as well. This last test is important because the major chamber asymmetries are a function of this angle. These comparisons are done in chapter 7 and result in a very conservative estimate of 30 % for the uncertainty in the Compton scattering component of the NHIT distribution. Further comparison between Monte Carlo simulations and experimental data, as well as further improvements in Monte Carlo source modeling, could perhaps reduce this uncertainty to less than the 5 % level.

6.3.4 The overall sensitivity of the ^{16}N source for energy scale determination

Given the above uncertainties and the uncertainties associated with EGS4 presented in chapter 4, the total uncertainty in the energy scale determination is

$$\Delta S_{Systematic} = \sqrt{\Delta S^2_{Chamber} + \Delta S^2_{Decay} + \Delta S^2_{Fit} + \Delta S^2_{EGS4} + \Delta S^2_{Noise} + \Delta S^2_{Statistical}} \qquad (6.2)$$

where $\Delta S_{Chamber}$ is the uncertainty associated with interactions with the source chamber, ΔS_{Decay} are those associated with the ^{16}N branching ratios, ΔS_{Fit} are those associated with the event reconstruction, ΔS_{EGS4} are those due to the EGS4 treatment of γ-rays, ΔS_{Noise} are those due to the

Table 6.7: List of all the uncertainties associated with the energy scale determination along with the calculated total systematic uncertainty.

$\Delta S_{Chamber}$	0.33 %
ΔS_{Decay}	0.12 %
ΔS_{Fit}	0.23 %
ΔS_{EGS4}	0.30 %
ΔS_{Noise}	0.03 %
$\Delta S_{Statistical}$	0.05 %
$\Delta S_{Systematic}$	0.52 %

noise determination, and $\Delta S_{Statistical}$ is the statistical uncertainty in the primary energy calibration measurement. Given that the ^{16}N can provide a million events in little over an hour, statistical accuracies of better than 0.05 % are easily achieved. The above uncertainties are summarized in Table 6.7. The calculated overall systematic uncertainty in the energy scale determination, and hence the sensitivity of the energy calibration, is 0.52 % which is well within the requirements of SNO. It is very likely that improvements in the Monte Carlo modeling of the source geometry and a better understanding of the systematics associated with event reconstruction can lower this uncertainty.

From the above, the ^{16}N source can clearly be used to measure the position and direction dependence of the energy scale to within a percent. The averaged measured uncertainty in the energy scale as a function of position and direction, $\Delta S_{\overline{x},\overline{u}}$, can then be determined. The total energy scale uncertainty for SNO would then be calculated using

$$\Delta S_{Total} = \sqrt{\Delta S^2_{Systematic} + \Delta S^2_{\overline{x},\overline{u}} + \Delta S^2_{Statistical}}. \tag{6.3}$$

The $\Delta S_{Statistical}$ uncertainty would be that of the position scans whose duration would likely be shorter than the primary calibration and the data would be subdivided according to fit position and direction. Statistical accuracy of better than 1 % will nonetheless be achieved. A preliminary estimate of ΔS_{Total} is discussed in chapter 7.

6.4 Unknown systematics

Above, the treatment of the known systematic uncertainties were discussed. A search for unknown systematic effects would include a comparison between Monte Carlo and DATA for all conceivable observables, off-line measurements, and cross-checks with sources of similar energy. Observables that may be investigated are the angular distribution of PMT hits with respect to the fitted direction, a detailed study of the NHIT spectrum (fraction of false triggers and the spectral shape at high NHIT values, etc), and a measure of the response (NHIT distributions and fraction of events) as a function of angle with respect to the source vertical axis. Some of these results are discussed in chapter 7. Off-line measurements have already been performed to search for the possibility of backgrounds produced with the DT generator or due to backgrounds in the chamber scintillator itself. This was done by placing the source in front of a Ge(Li) detector with the results shown in Figure 5.13. There are no observable peaks above the 6.13 MeV Compton scattering tail and therefore additional backgrounds should have no impact on the observed NHIT distribution mean. Finally a comparison of the ^{16}N NHIT spectrum to that of the 6.25 MeV γ-ray from neutron capture on deuterium can be made as a cross-check of the energy scale determination. A detailed discussion of this last option was given in [67]

Chapter 7

Experiments and Results

The following chapter presents results from experiments with the ^{16}N source taken during the air-fill stages of detector commissioning and shortly after the final D_2O fill.

7.1 Air-fill experiments and results

The air-fill stages of commissioning permitted the first tests of the SNO detector, in particular the electronics and data acquisition systems. Data taken during this period consisted mainly of detector background studies but also included calibration data with LEDs, the laserball, the sonoluminescence source, an alpha-scintillation source, and the ^{16}N source. Tests of the Monte Carlo were permitted by the detection of atmospheric muons and γ-rays from the surrounding rock wall interacting with the acrylic vessel, as well as with the calibration devices.

Some discrepancies were discovered between the Monte Carlo and the data. The number of PMT hits associated with muons was higher than expected and the muon hit patterns on the PSUP were more diffuse than expected. Also there was an excess of events with greater than 40 PMT hits in the spectrum from radioactive backgrounds compared to the Monte Carlo prediction. One possible explanation was that the energy scale in the Monte Carlo was incorrect or that the optics of the acrylic vessel were not fully understood. In order to do an additional test of the Monte Carlo and directly measure the light detection for gamma-rays in air-fill, the ^{16}N source was deployed in August of 1998.

Detector and trigger configuration

Air-fill data were taken with the ^{16}N source placed at the detector center and at various locations along the vertical axis. For all of these runs, the asynchronous (ASYNC) trigger was used. In the ASYNC trigger configuration, the ^{16}N PMT triggers the SNO detector promptly. This was done by sending the negative ^{16}N phototube pulse directly to the Master Trigger Card (MTC) via the Trigger Utility Board (TUB). The TUB can be used to convert trigger signals from various calibration devices to MTC compatible trigger pulses. For some of the runs, the source signal was split and part of the signal sent to the calibration front end card so that ^{16}N PMT information, such as the pulse height, could be retrieved. In addition to the ASYNC trigger, a software generated Pulsed Global Trigger or PGT was set at 100 Hz to sample the detector background. To get an estimate of the number of operational phototubes, PMT occupancies were calculated with the center ^{16}N run data (see Figure 7.1 histogram). All phototubes with greater than 250 hits were considered operational. The total number of tubes calculated was 8255 or 86.5 % of the PSUP total. The remaining channels had not yet been activated.

Study of the NHIT and timing distributions

In air-fill, the Čerenkov light for ^{16}N is produced as a result of γ-ray Compton scattering in the acrylic vessel. The energy deposition as determined in the Monte Carlo is shown in Figure 7.2. Part of the light produced will be totally internally reflected within the acrylic vessel and not be detected.

The NHIT spectrum for the chamber triggered events (ASYNC) is shown in Figure 7.3. Also shown are the PGT triggered events scaled to the lower NHIT peak in the chamber triggered

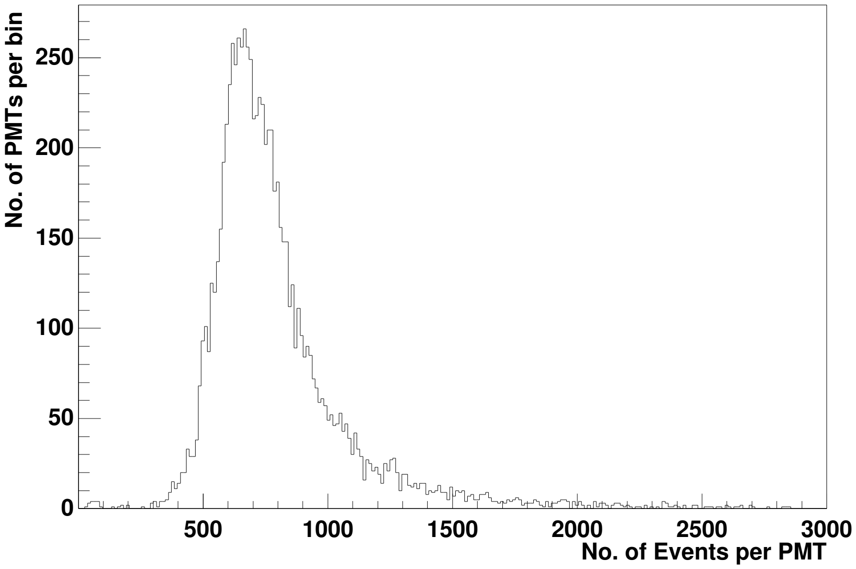

Figure 7.1: Phototube occupancy histogram for ^{16}N air-fill data.

spectrum. Subtraction of the PGT spectrum results in the Figure 7.4 spectrum which is more representative of the Compton scattering event spectrum. The PGT spectrum is due mostly to PMT dark noise, but also to real physics backgrounds. Because of these additional physics backgrounds, the "PGT-like" background is not modeled in the Monte Carlo. The Monte Carlo used for comparison to the data was therefore generated with no noise added and was convolved with the measured PGT background. This method was previously applied to the analysis of air-fill ^{16}N data in [83]. There is an obvious discrepancy between data and Monte Carlo. In order to agree, the ^{16}N component of the Monte Carlo spectrum must be scaled up (along the NHIT axis in Figure 7.4) by 90 %, as reported in [83].

The PMT timing distribution was used to identify ^{16}N Čerenkov-light-producing events. This was done by defining a 6 nano-second window around the summed event prompt region. A cut was then made on events in which one (TAC=1), two (TAC=2) , or three (TAC=3) tubes fired inside the gate, and the resulting NHIT spectra are shown in Figure 7.5. The TAC=2 cut timing spectrum

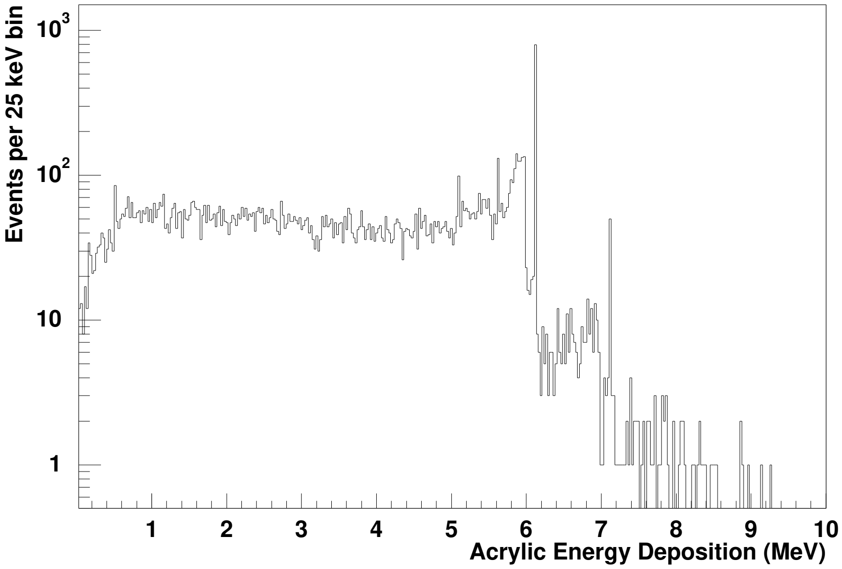

Figure 7.2: Energy output of the ^{16}N source in air-fill from Monte Carlo simulation. In air-fill ^{16}N γ's produce Čerenkov light by interacting with the acrylic vessel.

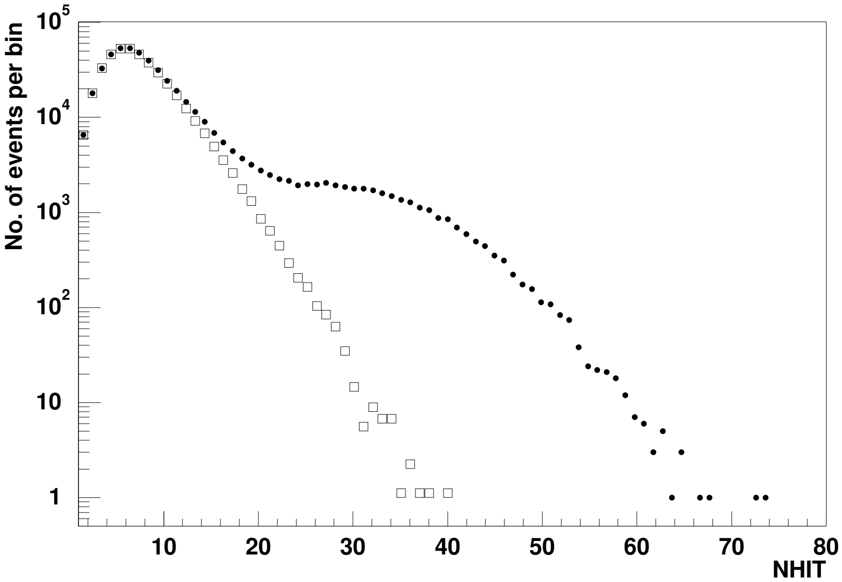

Figure 7.3: Air-fill ^{16}N NHIT distributions. Shown are the ASYNC spectrum (dots) which are due to ^{16}N triggers and the PGT spectrum (open squares) which is a sampling of the detector backgrounds.

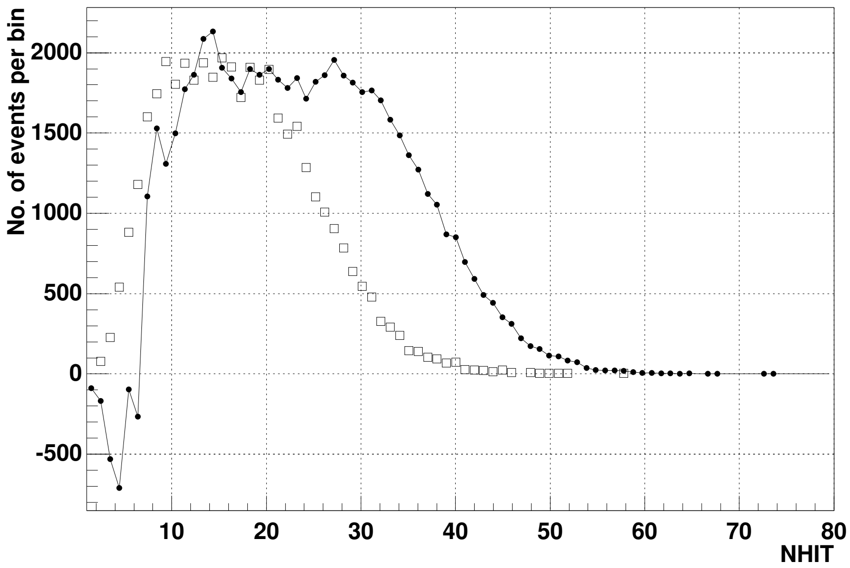

Figure 7.4: Air-fill background subtracted ^{16}N NHIT distribution (connected dots) compared to a noiseless ^{16}N Monte Carlo convolved with the PGT spectrum (open squares).

is shown in Figure 7.6. This is compared to the ^{16}N Monte Carlo which had dark noise added at PGT levels. Both spectra were scaled to the noise hits prior to the prompt light peak. Irrespective of the normalization, the data has additional late light which strongly suggests that the excess hits are due to light that should, according to the Monte Carlo, have been totally internally reflected in the acrylic vessel. In Figure 7.7, the fitted radial position of the events with the TAC=2 cut is shown and is consistent with Čerenkov light production at the acrylic vessel.

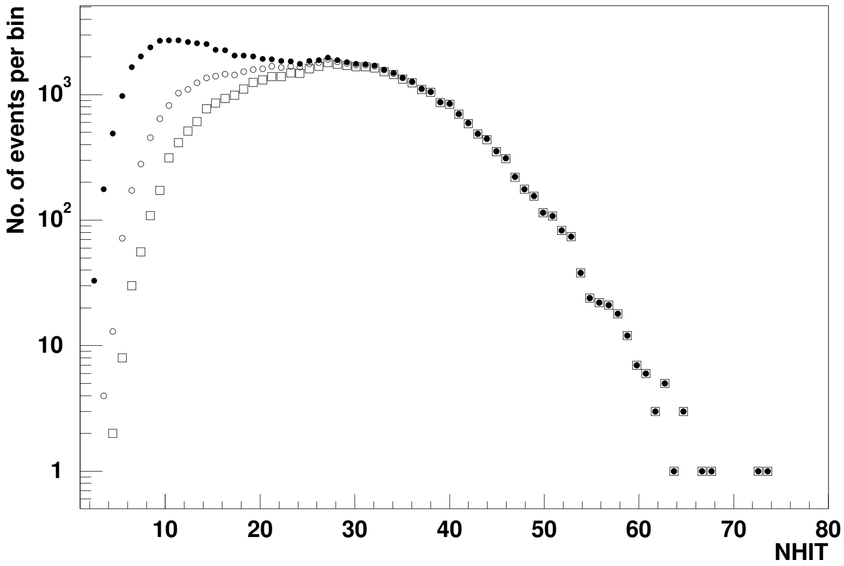

Figure 7.5: Air-fill ^{16}N NHIT spectra with TAC cuts. Shown are NHIT spectra with a TAC = 1 cut (dots), TAC = 2 cut (open circles), and a TAC = 3 cut (open squares).

The time structure was also studied by counting the number of hits registered in time acceptance windows, or gates, of different width in the Čerenkov light detection region. Figure 7.8 shows the hit distributions inside a 30 nanosecond window around the prompt peak for TAC=2 events. In this instance, the data and Monte Carlo are in better agreement. If progressively longer time acceptance windows are used, the discrepancy between Monte Carlo and data increases. This is

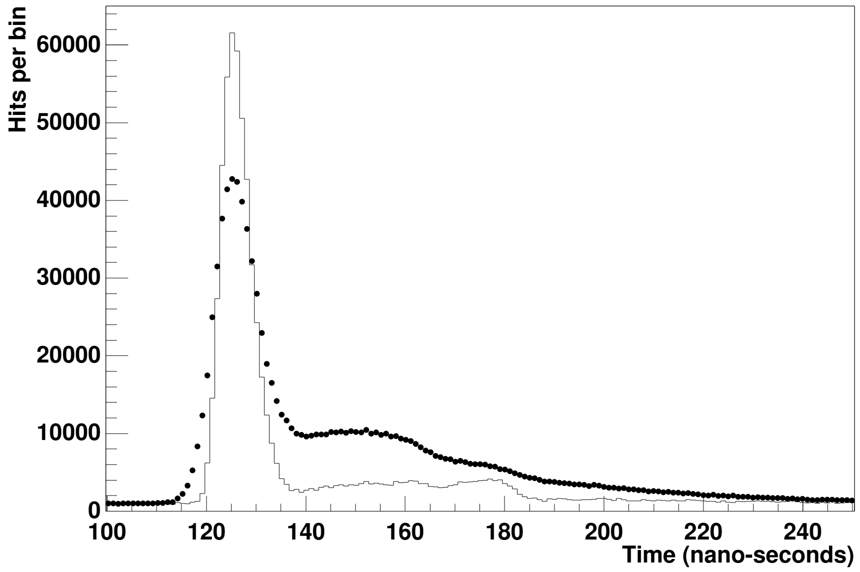

Figure 7.6: PMT timing distribution for ^{16}N events with a TAC cut. Timing distributions for both ^{16}N data (dots) and Monte Carlo (line) are shown. A TAC = 2 cut was applied.

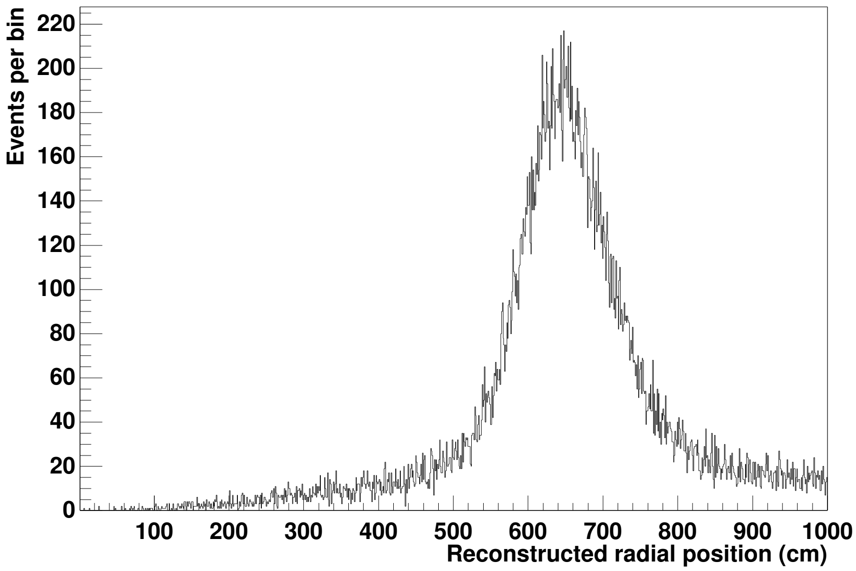

Figure 7.7: Reconstructed ^{16}N fit event radii in air-fill with a TAC = 2 cut. The acrylic vessel is located at 600 centimeters and therefore the mean fitted position is systematically shifted outward.

consistent with the conclusion that the higher mean NHIT value is due to additional scattered and reflected light escaping the acrylic vessel as opposed to radical differences in the energy scale.

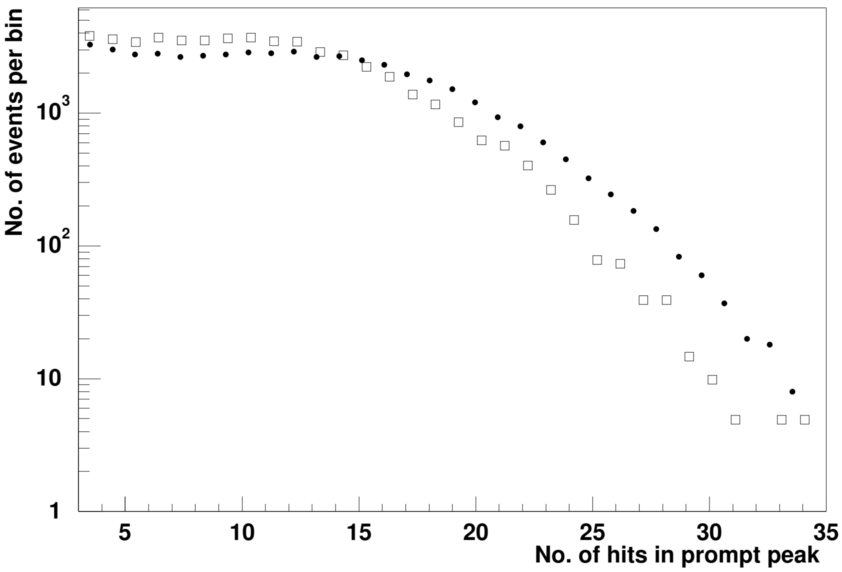

Figure 7.8: ^{16}N air-fill hit distribution for a 30 ns time Air-fill hit distributions in a 30 nanosecond time acceptance window for ^{16}N data (dots) compared to Monte Carlo (open squares). A TAC = 2 cut was applied.

Conclusions

The ^{16}N source results demonstrated that the Monte Carlo underestimated the number of PMT hits for gamma-rays interacting in the acrylic vessel for an air-fill detector. Also it was shown that the additional light was being detected after the direct Čerenkov light hit times (i.e the prompt peak). It is therefore likely that less light was trapped in the acrylic vessel than was predicted in the Monte Carlo. Possible escape avenues for this light include slight imperfections on the acrylic vessel surfaces or the acrylic bond joints. Another possible explanation is that the level of diffuse scattering and the acrylic attenuation at long wavelengths are different than in the Monte Carlo.

This last explanation was reported in [110] for explaining the muon data. The exact nature of the additional detected light is not yet fully understood, but it should be noted that these effects should not be present in the D_2O detector where the acrylic and water indices of refraction are better matched.

7.2 D_2O energy calibration experiments and results

The following sections present analysis results of the initial ^{16}N energy calibration experiments for the detector filled with D_2O taken in July of 1999. This includes the ^{16}N energy scale and response verification measurements. At the time of these experiments, the SNO detector was fully operational, but the electronics constants (ECA and PCA) had not yet been fully optimized and detailed analyses of the optical properties of the detector were incomplete.

Detector and trigger configuration, and run descriptions

The experiments followed the procedures outlined in chapter 4. An initial energy calibration measurement was taken with the ^{16}N source (center of gas volume) positioned at X = -16 cm, Y = +23.5 cm, and Z = -11 cm, with respect to the center of the D_2O volume. An additional 11 measurements were taken with the source located at varying Z positions for the energy response verification. The manipulator system had not yet been configured for locations off the Z axis. A variety of trigger configurations were tested but for these runs, NHIT triggers were set along with the external ^{16}N chamber scintillator trigger. The scintillator triggers were used for energy calibration, and the NHIT triggers with a veto on the scintillator trigger were used for analyzing decays in the umbilical tube. In addition to the above triggers, the detector noise was sampled with PGTs. As with the air-fill runs, PMT occupancies were calculated with the central ^{16}N run (see Figure 7.9 histogram). Of the 9546 SNO PMTs, 9221 (96.5 %) were accepted and used in the accompanying Monte Carlo. It should also be noted that the magnetic compensation coils were turned on for these runs and that the measured increase in gain with the coils on, from ^{16}N source measurements, was 10 %.

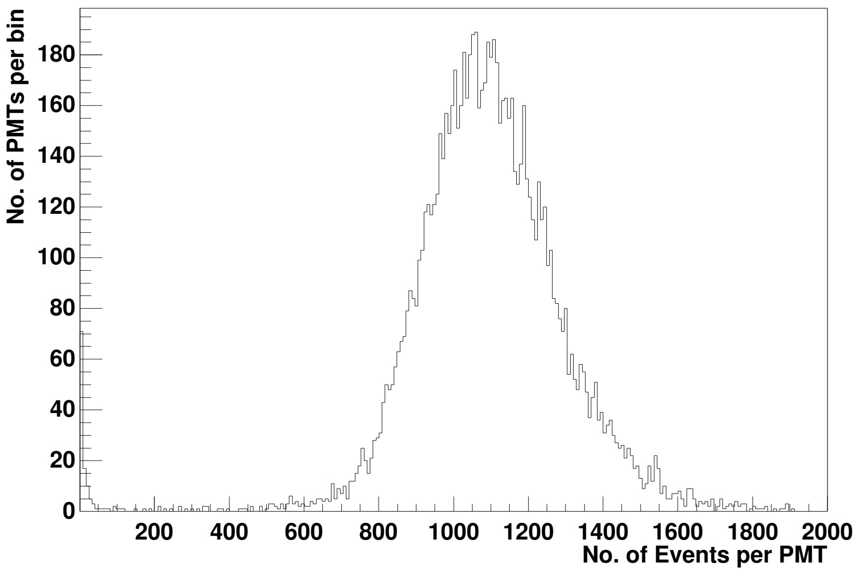

Figure 7.9: PMT occupancy histogram for ^{16}N D_2O data.

The raw NHIT and timing distributions

The NHIT distribution for the center run is shown in Figure 7.10. Also given is the Monte Carlo result. The Monte Carlo used the parameters listed in Table 6.3 which are the default values for the SNOMAN version 3.0185. The noise was modeled according to the PGT measurements. The two distributions were scaled to the peak values above NHIT=20. One notices that the shapes are very similar but that the γ-peak mean NHIT value is slightly higher in the data. The discrepancy may be due to incorrect optical parameters in the Monte Carlo or the energy scale. The energy scale measurements are discussed in the following subsection.

The time-of-flight corrected time spectrum using the time fitter algorithm is shown in Figure 7.11. The spectra were scaled to the noise background on the left of the prompt light peak. On the logarithmic scale, there are noticeable differences in the Monte Carlo response. First, this Monte

Carlo does not have PMT pre or late pulsing added in and the PSUP reflections are considerably different. The prompt peak, however, is well modeled. Nevertheless, a correct analysis of the energy response will require a detailed understanding of these timing distributions. It should be noted that the PMT timing characteristics from earlier off-line measurements [71] have since been added to the Monte Carlo.

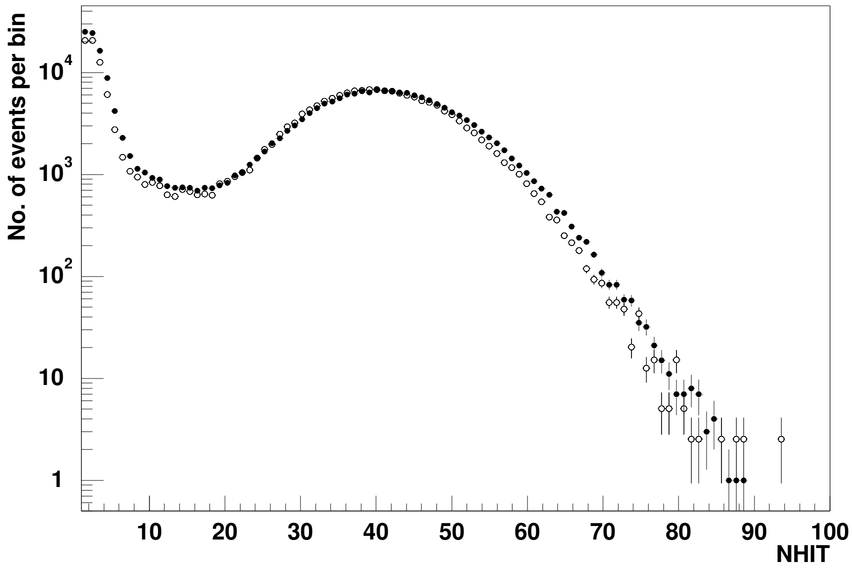

Figure 7.10: NHIT spectra in D_2O for ^{16}N data (solid circles) and Monte Carlo (open circles). The distributions were normalized to the maximum values in the γ-peak region.

The ^{16}N energy scale determination

In the determination of the energy scale, the total number of PMT hits, NHIT, was used. Analysis using only the number of tubes that fire in a predefined window around the prompt peak, N_{Win}, could also be done but must await a better understanding of the event reconstruction algorithm performance. Following the methods outlined in chapters 4, the NHIT distribution for

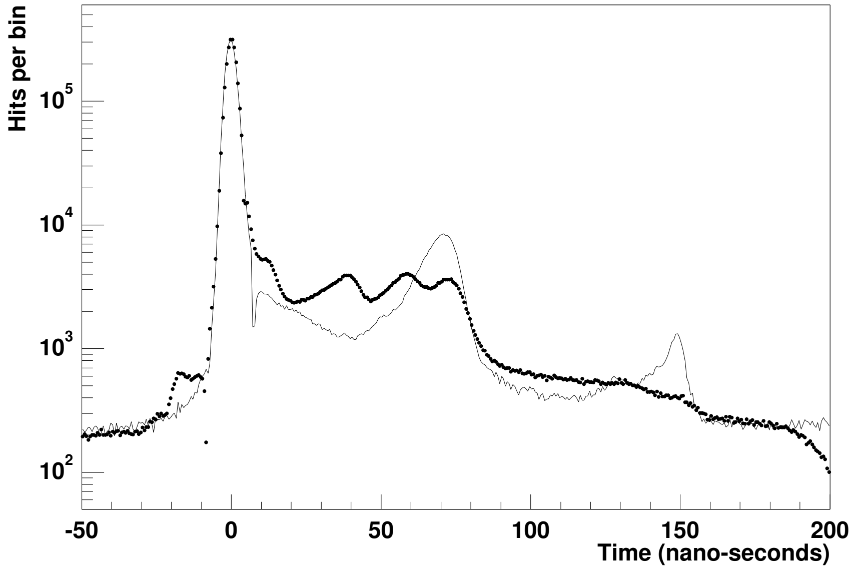

Figure 7.11: ^{16}N time-of-flight corrected PMT time spectrum for data (dots) and Monte Carlo (solid line).

data and Monte Carlo were used to calculate the absolute energy normalization parameter S_{Energy}. Only events in which there was a reconstructed position were selected in order to eliminate the bulk of the ground state beta contributions. The Monte Carlo was modeled with zero PMT noise and was convolved with the measured PGT spectrum. For this analysis, the fit function presented in chapter 6 (equation 6.1) was used to compare the experimental NHIT distribution to that from Monte Carlo simulation. The resulting spectrum for the experimental data and the fit result are shown in Figure 7.12. The optimal PMT collection efficiency correction factor using this comparison is

$$S_{Energy} = 1.047. \tag{7.1}$$

The detailed χ^2 minimization comparison described in chapter 4 was not done for this preliminary analysis. The comparison between data and the scaled Monte Carlo NHIT distributions are shown in Figures 7.13 and 7.14. The measured difference in the RMS's of the distributions is

$$\frac{\Delta\sigma}{\sigma} = 0.7\ \%. \tag{7.2}$$

The details of the full NHIT spectrum and the angular properties of the chamber were also investigated in order to estimate the overall uncertainties in the primary energy scale measurement due to incomplete modeling of the source as was discussed in chapter 6. The results are summarized in Figures 7.15 and 7.16. In Figure 7.15 the ratio of the NHIT bin content for Monte Carlo simulation and experimental data is shown. The two distributions were normalized using the total number of events which reconstructed within the D_2O volume. The results indicate a maximum difference of 30 % in the 10 to 30 NHIT range. This value is used as a very conservative measure of the systematic uncertainty associated with the source geometry. There may also be some discrepancies at high NHIT values that will require further investigation. For example, random coincidences between ^{16}N events (i.e pile-up) are not included in the Monte Carlo. This last detail, however, would likely not affect the energy scale determination. It should be noted that similar effects would arise with a faulty energy scale determination. Use of ratio plots like that of Figure 7.15, or of a cumulative ratio plot, might prove to be a valuable diagnostic for the energy scaling

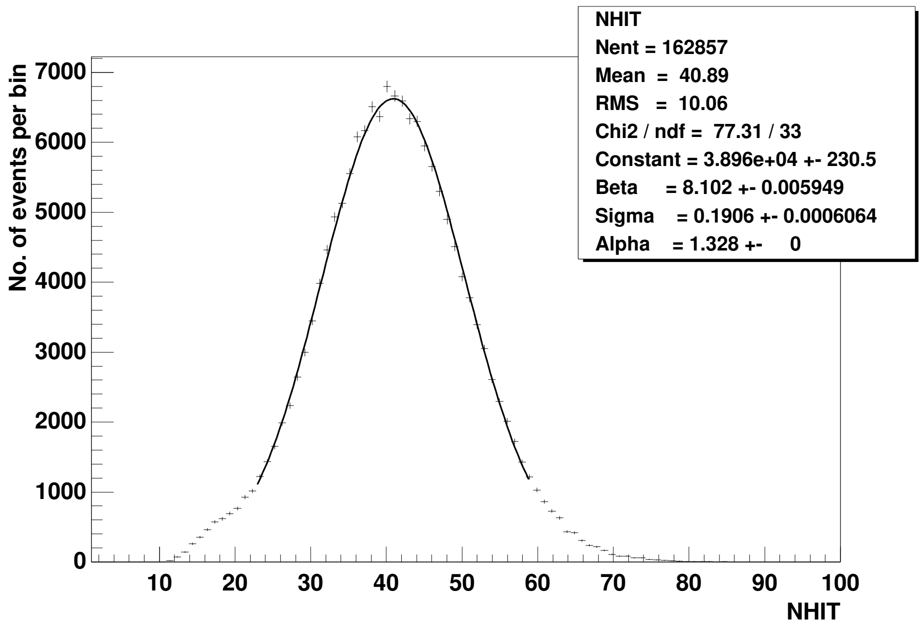

Figure 7.12: Energy scale fit (equation 6.1) to the ^{16}N data. Only events which reconstruct within the D_2O volume are included.

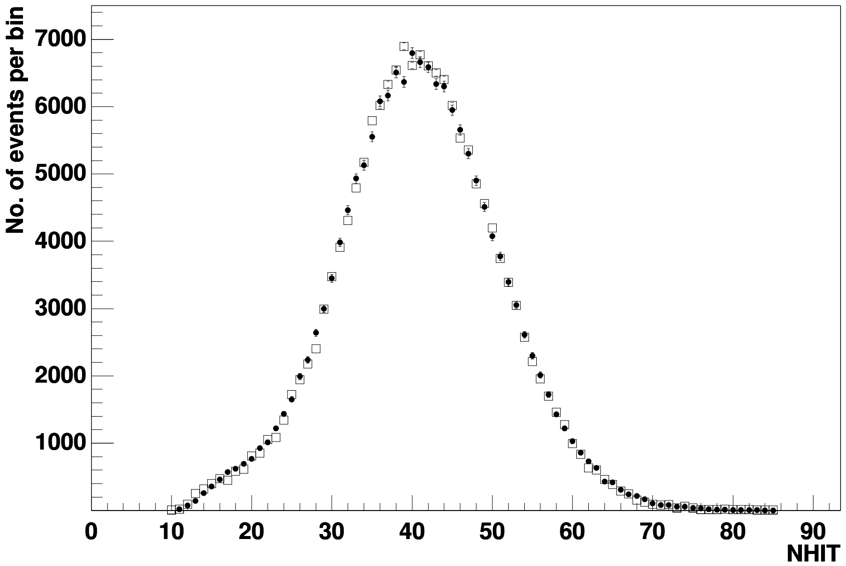

Figure 7.13: Comparison of NHIT distributions for the ^{16}N scaled Monte Carlo (open squares) and data (dots). Statistical errors are included.

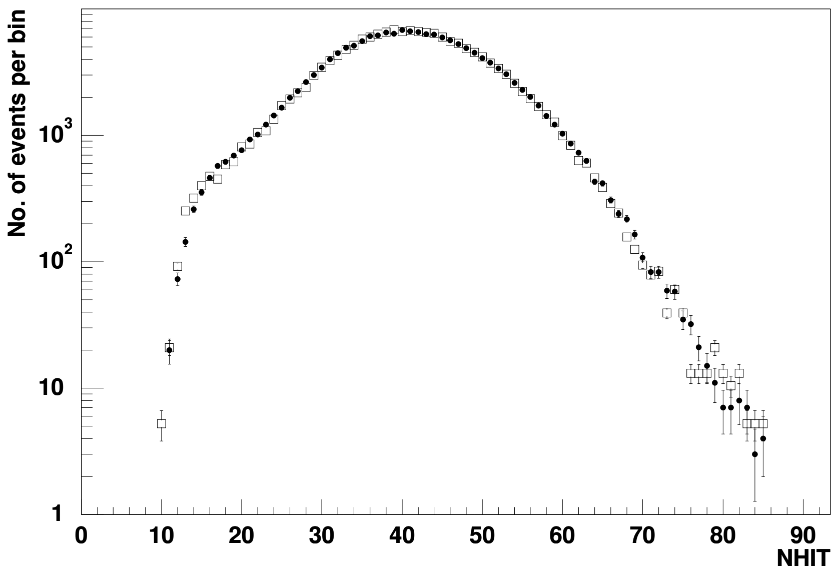

Figure 7.14: Comparison of NHIT distributions (logarithmic scale) for the ^{16}N scaled Monte Carlo (open squares) and data (dots). Statistical errors are included.

determination. Figure 7.16 shows the number of events as a function of polar angle for the source located at the center of the detector and is consistent with the Monte Carlo result.

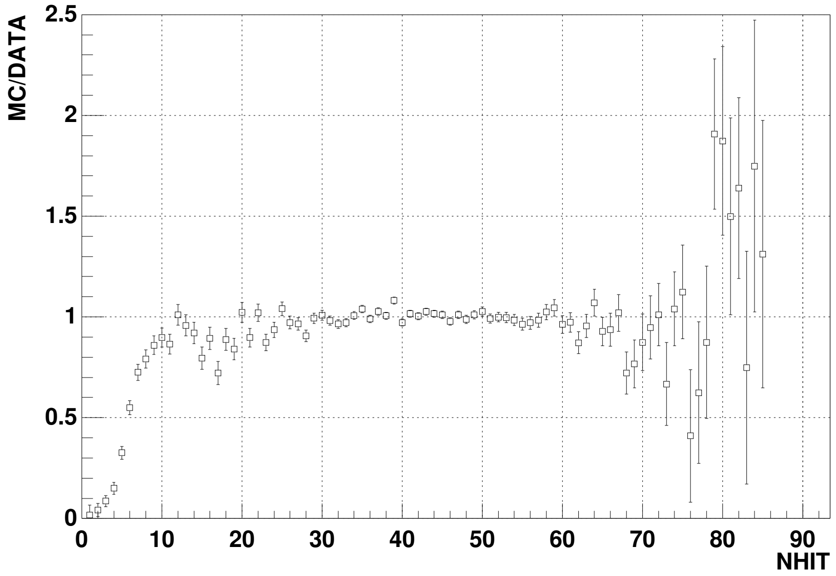

Figure 7.15: ^{16}N spectral shape comparison: Data vs Monte Carlo. The ratio of Monte Carlo results to experiment as a function of NHIT bin are shown. The two distributions were normalized with the total number of events which reconstructed within the D_2O volume. The large discrepancy in NHIT values below NHIT=10 is due to having convolved a noiseless Monte Carlo to PGT data, hence eliminating "false triggers" in the Monte Carlo. The maximum difference between the data and Monte Carlo in the 10 to 30 NHIT range is 30 %. Statistical errors are given.

Energy response measurements

The measurement of the uncertainty in the SNO detector energy response was done following the methods outlined in chapter 4 for the vertical axis data. For position scan measurements, the

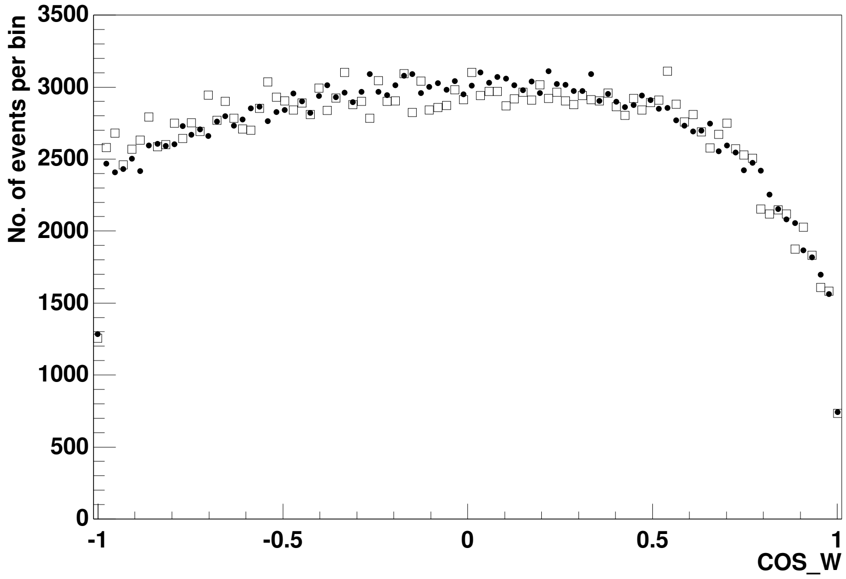

Figure 7.16: Number of ^{16}N events as a function of the fitted direction cosine with respect to the Z axis for data (dots) and Monte Carlo (open squares). The source was located at the center position.

NHIT mean for data and the Monte Carlo are summarized in Figure 7.17 as a function of Z position, and in Figures 7.18 to 7.20 as a function of Z position and fitted direction cosine with respect to the Z axis. The Z position dependence is given in Table 7.1 as well. In Table 7.1, the maximum deviation in the Monte Carlo calculated mean compared to the experimental result is 7.5 %. The likely reason for the discrepancy between data and Monte Carlo are inadequate optical constants. For example, greater levels of D_2O attenuation would enhance the mean NHIT response for events originating further out in radius. Optical analyses are, however, preliminary and are ongoing, and for these reasons Monte Carlos with varying input parameters have not been attempted. Also, because the energy scale uncertainty is presently the main systematic in the energy resolution, a detailed analysis of the energy resolution as a function of position and direction has been postponed as well.

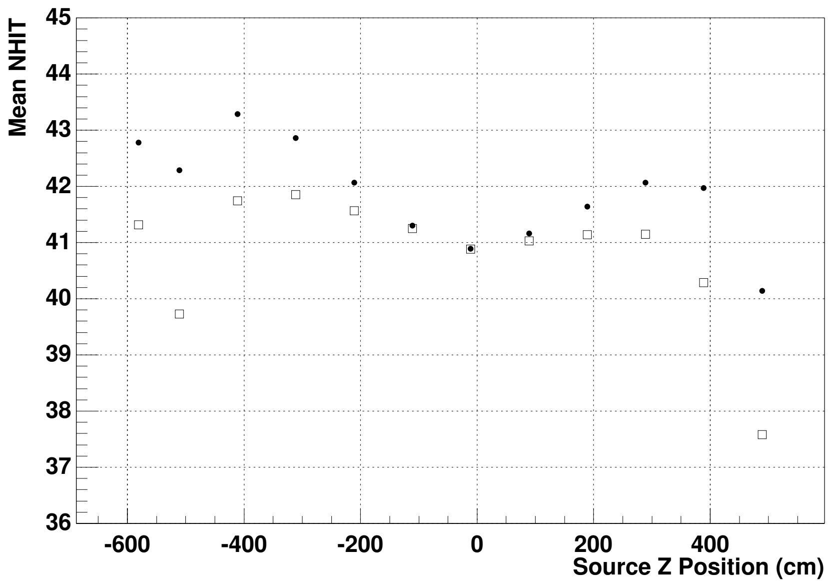

Figure 7.17: ^{16}N NHIT dependence on Z source position for data (dots) and Monte Carlo (open squares).

The results for these preliminary results were nonetheless used to estimate the overall uncer-

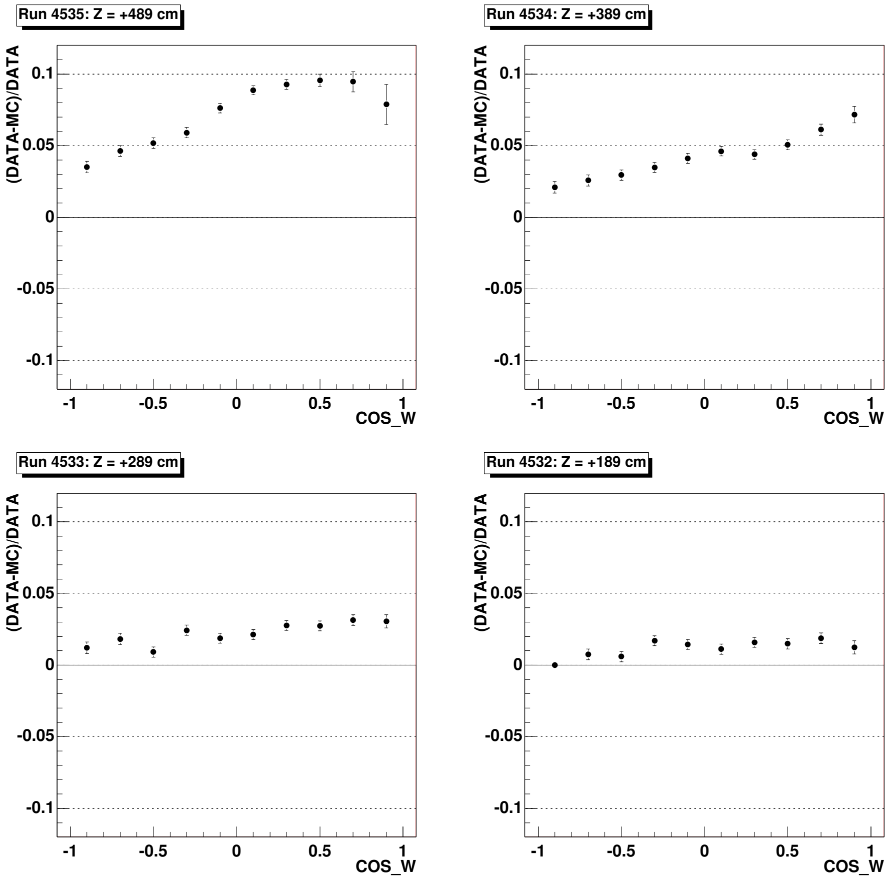

Figure 7.18: ^{16}N position and direction dependence I. The difference in Monte Carlo (MC) calculated response (mean NHIT) compared to the data (DATA). Multiplication of the result by 100 gives the percent difference. Results are given for the source positioned at Z=+489 (upper left), Z=+389 (upper right), Z=+289 (lower left), and Z=+189 (lower right). COS_W is the cosine of the angle between the reconstructed direction and the vertical axis. The errors are statistical.

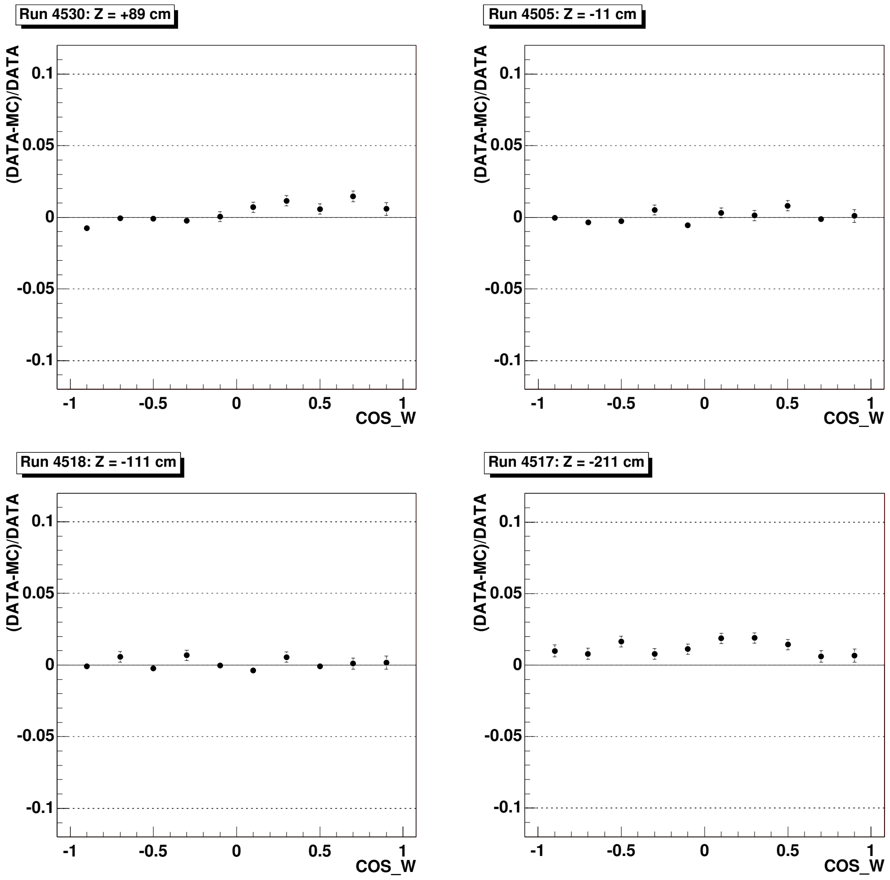

Figure 7.19: ^{16}N position and direction dependence II. The difference in Monte Carlo (MC)calculated response (mean NHIT) compared to the data (DATA). Multiplication of the result by 100 gives the percent difference. Results are given for the source positioned at Z=+89 (upper left), Z=-11 (upper right), Z=-111 (lower left), and Z=-211 (lower right). COS_W is the cosine of the angle between the reconstructed direction and the vertical axis. The errors are statistical.

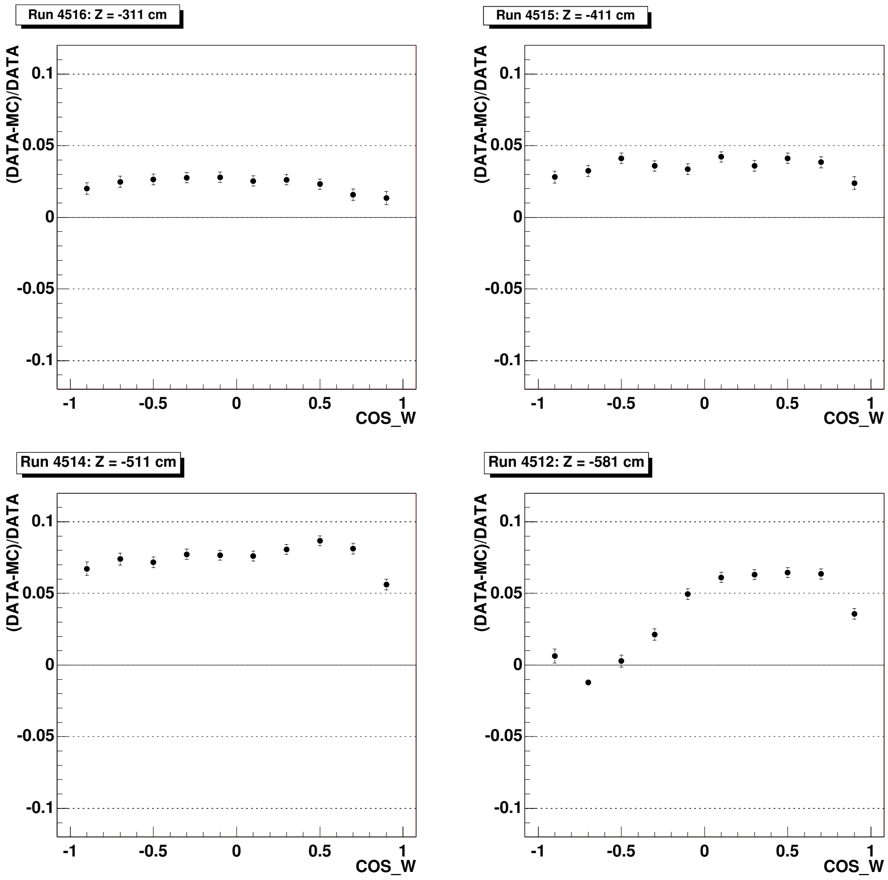

Figure 7.20: ^{16}N position and direction dependence III. The difference in Monte Carlo (MC)calculated response (mean NHIT) compared to the data (DATA). Multiplication of the result by 100 gives the percent difference. Results are given for the source positioned at Z=-311 (upper left), Z=-411 (upper right), Z=-511 (lower left), and Z=-581 (lower right). COS_W is the cosine of the angle between the reconstructed direction and the vertical axis. The errors are statistical.

Table 7.1: Summary of the ^{16}N energy response measurements as a function of Z source position. Shown are mean NHIT values for experimental (DATA) and Monte Carlo simulation (MC) of the ^{16}N source. The percent difference in Monte Carlo and data for the NHIT distribution means is also given.

Run No.	Z Position (cm)	μ_{DATA} (NHIT)	μ_{MC} (NHIT)	$\Delta\mu$ (%)
4535	+489	40.14	37.58	6.4
4534	+389	41.97	40.29	4.0
4533	+289	42.07	41.15	2.2
4532	+189	41.64	41.14	1.2
4530	+89	41.16	41.03	0.3
4505	-11	40.89	40.88	0.0
4518	-111	41.30	41.25	0.1
4517	-211	42.07	41.57	1.2
4516	-311	42.86	41.85	2.4
4515	-411	43.29	41.74	3.6
4514	-511	42.29	39.73	7.5
4512	-581	42.78	41.32	3.4

tainty in the energy scale response. This was done by taking the average of the position scan data (the Z = -581 cm run was excluded) and weighting by the fractional volume of the detector in which each source position is representative. This can be expressed by

$$\overline{\Delta E_{Resp}} = \sum_{i=1}^{i=n_z} \left[\frac{\mu_{DATA}(z_i) - \mu_{MC(z_i)}}{\mu_{DATA}(z_i)} \right] w(z_i) \tag{7.3}$$

where n_z is the number of position scans and $w(z_i)$ are the weightings for each position. This results in an averaged energy uncertainty of 6.1 % for the fiducial volume within a 550 cm radius of the detector center.

Conclusions

The above results have demonstrated that the ^{16}N source calibration techniques work in D_2O. The center position calibration showed that the Monte Carlo PMT collection efficiency had to be scaled by a factor of 1.047 in order to agree. The scaled Monte Carlo results, however, were shown not to agree as a function of position and direction. This is a clear indication that the present optical parameters used in the Monte Carlo are inadequate. Given the present optical constants, the averaged energy scale uncertainty is 6.1 % within a 550 cm radius fiducial volume. Improved optical parameters should reduce this to below the percent level. Further optical calibration and analysis will therefore be required. In addition, a more extensive set of ^{16}N calibrations at multiple positions in the East-West and North-South vertical planes permitted with the source manipulator system will be required.

7.3 Additional observations and analysis

The following presents a first look at other analyses that will be permitted with the ^{16}N data and which will provide additional means for verifying the Monte Carlo. This section is intended to showcase the capabilities of the ^{16}N source for calibration purposes other than for energy scale determination. More detailed analysis will be permitted once a complete set of ECA, PCA, and

OCA constants are available.

The time fitter performance and the photon angular distribution

The time fitter position and direction reconstruction algorithm was tested. The results of the time fitter for the data compared to the Monte Carlo are shown in Figure 7.21 for the center position. The results for all the positions are summarized in Table 7.2. In most cases data and Monte Carlo agree in the calculated mean positions to within a few cm. Differences in the calculated Z positions do, however, show a systematic shift outward in the reconstruction for events occurring further out in radius. Many of these effects may be due to the fact that the PMT timing calibrations used were preliminary and therefore it is premature to make any conclusions about the performance of the fitters. Further experiments and analysis of the performance of the various reconstruction algorithms using ^{16}N data will be required.

The photon angular distribution was studied by looking at the angles between the fitted direction and the vectors joining the fit position to the individual PMTs. This is shown in Figure 7.22 for PMTs that fired within a $\pm$ 10 nano-second timing gate around the prompt peak in the time-of-flight corrected timing spectrum. Also shown is the distribution for Monte Carlo generated events. The distributions are remarkably similar and hence there is great confidence in the Monte Carlo treatment of the Čerenkov light emission.

The fitted direction with respect to the calculated ^{16}N source gamma direction is shown in Figure 7.23. Only events which reconstructed between 100 and 200 cm away from the source position were used to generate the distributions. Sharper angular distributions would result if the position cut was between 200 and 300 cm but is not shown here because of limited statistics in the data and Monte Carlo simulation. Analysis of the angular resolution is ongoing. The technique for studying the angular resolution using the ^{16}N source is shown to be very promising.

Table 7.2: Time fitter response. Shown are the true ^{16}N source position as determined with the manipulator system, and the fitted positions for Data and Monte Carlo (MC). Treatment of the data and Monte Carlo were identical except for the additional requirement that the scintillator fire in the real data.

Run No.	Position			Data			MC		
	X(cm)	Y(cm)	Z(cm)	X(cm)	Y(cm)	Z(cm)	X(cm)	Y(cm)	Z(cm)
4535	-16	+23.5	+489	-15.5	+23.8	+503.6	-15.6	+23.0	+489.0
4534	-16	+23.5	+389	-15.5	+23.3	+399.4	-15.8	+23.0	+389.8
4533	-16	+23.5	+289	-15.1	+22.8	+298.2	-15.9	+23.0	+289.8
4532	-16	+23.5	+189	-15.4	+22.4	+196.2	-15.9	+23.1	+189.4
4530	-16	+23.5	+89	-15.9	+22.9	+94.6	-16.0	+23.0	+89.0
4505	-16	+23.5	-11	-15.2	+22.7	-9.5	-15.6	+23.1	-11.2
4518	-16	+23.5	-111	-16.4	+23.0	-109.4	-15.9	+23.2	-111.3
4517	-16	+23.5	-211	-17.4	+23.2	-211.0	-15.8	+23.1	-211.8
4516	-16	+23.5	-311	-16.8	+23.7	-312.4	-15.6	+22.9	-311.5
4515	-16	+23.5	-411	-17.5	+23.6	-414.3	-15.6	+22.8	-412.0
4514	-16	+23.5	-511	-17.1	+24.8	-516.3	-15.6	+22.8	-514.3
4512	-16	+23.5	-581	-16.9	+24.2	-588.8	-16.2	+23.9	-583.6

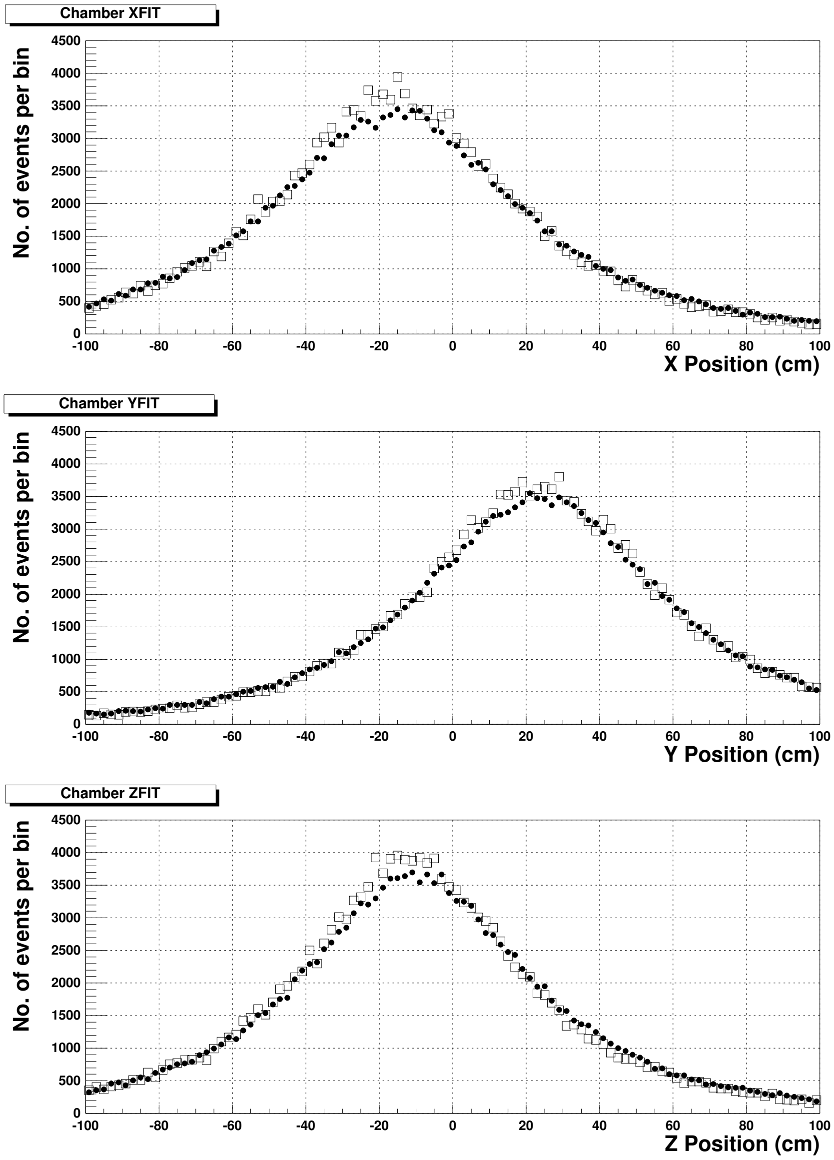

Figure 7.21: Time fitter performance for data (dots) and Monte Carlo (open squares) for reconstructed X (top panel), Y (middle panel), and Z (bottom panel) positions. The source was located at X=-16 cm, Y=+23.5 cm, and Z= -11 cm with respect to the detector center. The distributions were normalized to the total number of reconstructed events.

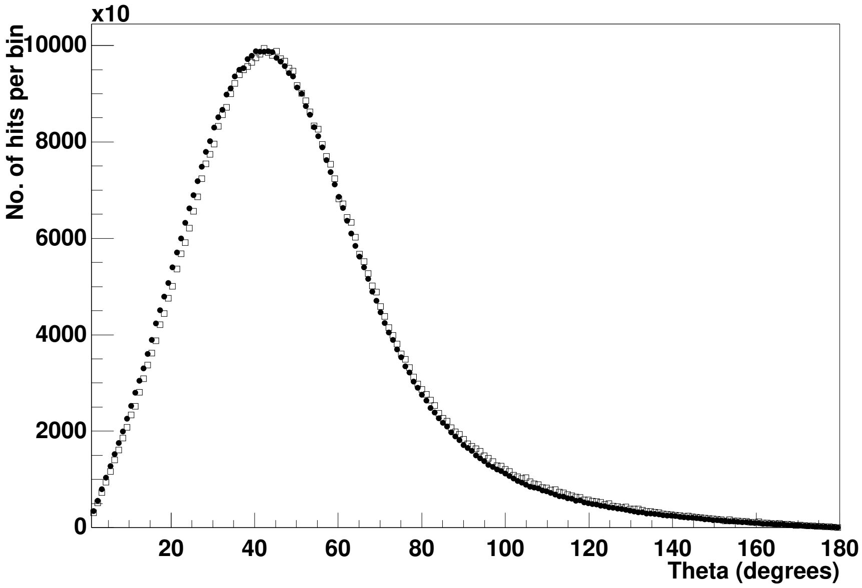

Figure 7.22: Angular distribution of hit phototubes with respect to the time-fitted direction for data (dots) and Monte Carlo (open squares). Only photubes which fired within ± 10 nanoseconds of the prompt Čerenkov peak are included.

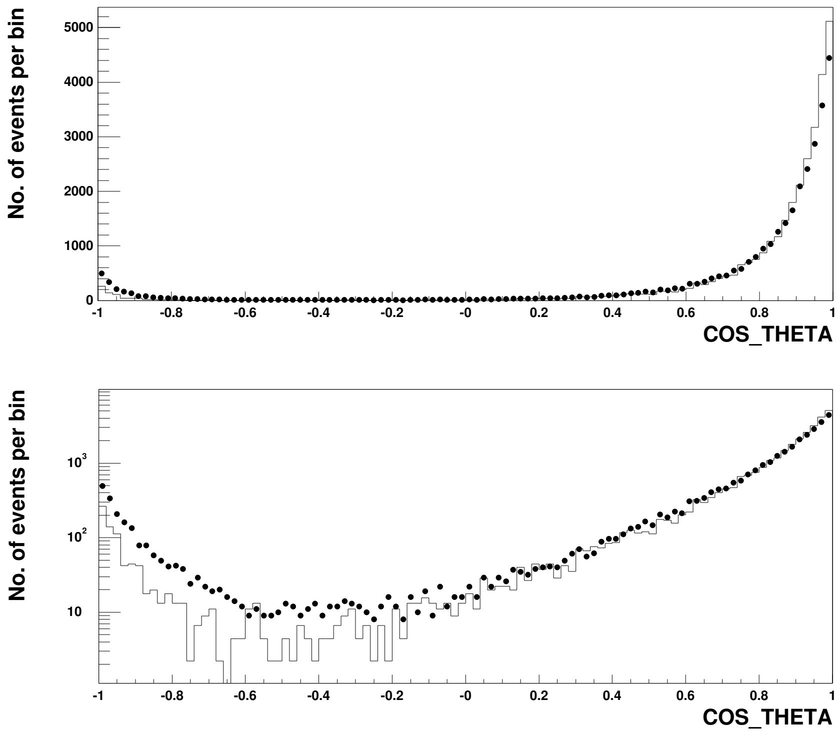

Figure 7.23: Angular resolution studies with the ^{16}N source. Shown are the number of events as a function of the cosine of the angle between the reconstructed direction vector and the vector joining the decay chamber to the fit position for data (dots) and Monte Carlo (line). Only events with a reconstructed position vertex between 100 and 200 cm away from the chamber origin were chosen.

The umbilical decays

An additional analysis was permitted with the umbilical data. The analysis was done with data from a run with the ^{16}N chamber at Z = -581 cm below the center of the D_2O volume. Figure 7.24 shows the reconstructed Z position for events which triggered the scintillator and those that did not. A further cut on a 40 cm distance in the X-Y plane centered about the umbilical was also used. One sees the roughly constant rate all the way down the umbilical with no apparent pollution from chamber events which might have mistriggered the scintillator. The NHIT spectrum for the umbilical events is shown in Figure 7.25. The mean is higher than for the chamber events because many of the β's would deposit energy into the detector as well. The energy absorbed in the umbilical is not well modeled in the Monte Carlo so it is perhaps not appropriate for use in the absolute energy scale determination. However, the calculated NHIT means as a function of calculated position may prove useful for verifying the ^{16}N position scan results. In Figure 7.26, the umbilical means are scaled to the center chamber result and compared to the chamber results along the Z axis and the ^{16}N chamber and umbilical results appear to agree. Further investigation of the use of umbilical data is underway.

Conclusions

Use of the ^{16}N source for purposes other than energy calibration has been demonstrated. Of particular importance are the fitter performance and angular resolution studies.

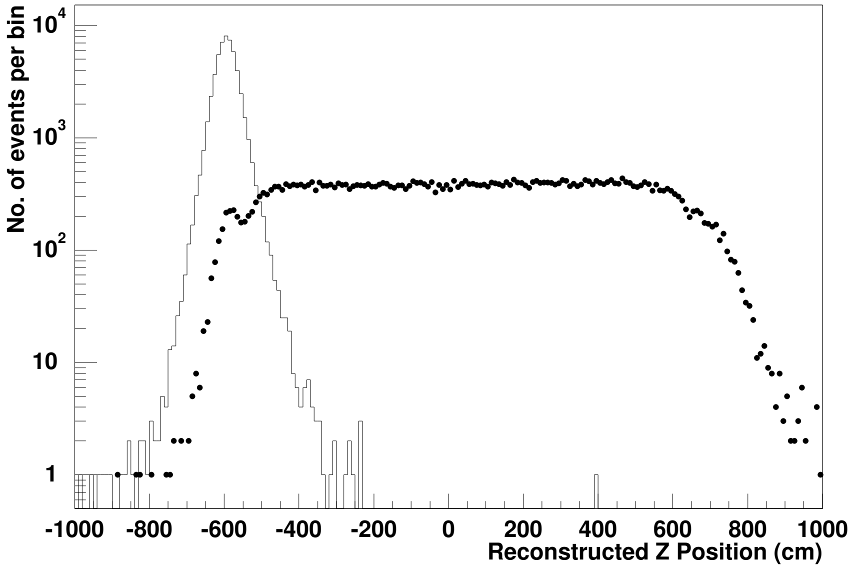

Figure 7.24: Reconstructed umbilical (line) and chamber (dots) ^{16}N decays. Shown are the fit Z position for events which reconstruct within 40 cm of the umbilical position in the X-Y plane.

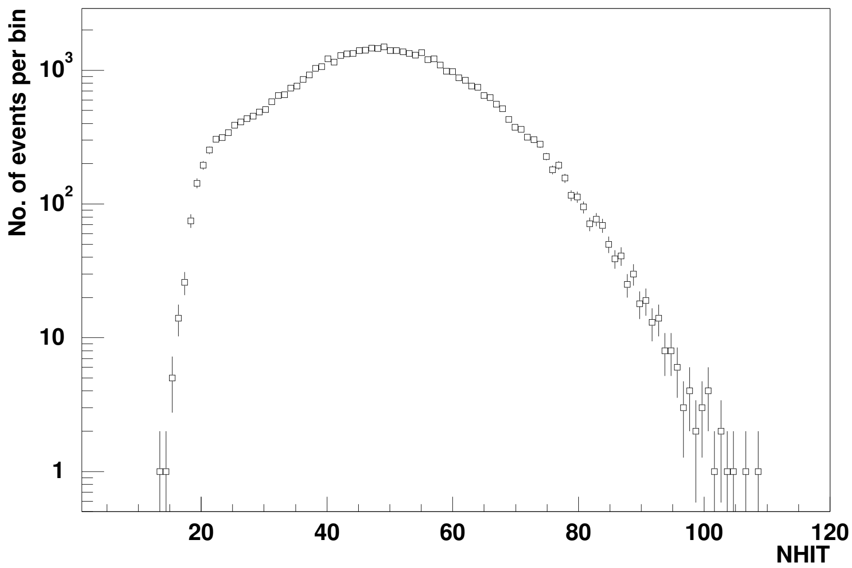

Figure 7.25: The ^{16}N umbilical decay NHIT spectrum. Events which reconstruct within 40 cm of the umbilical in the X-Y plane and within -600 cm and +600 cm in the Z position were selected.

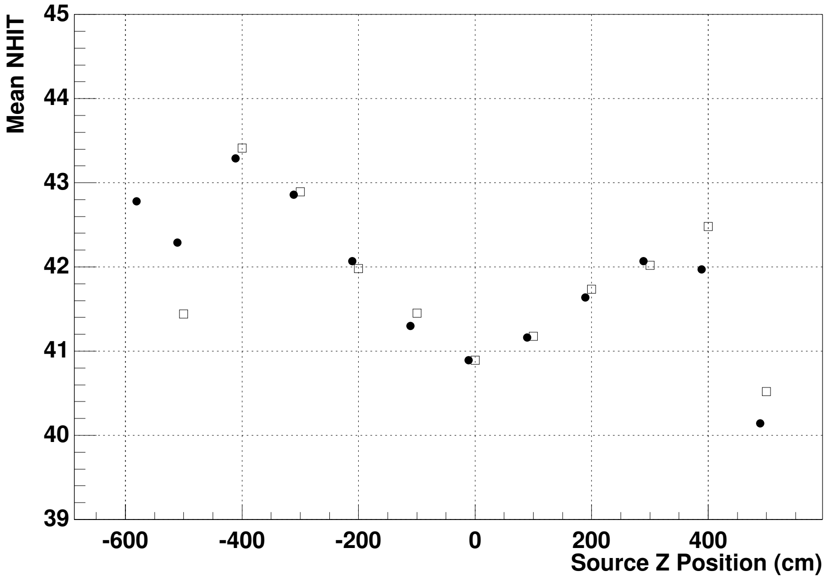

Figure 7.26: Comparison of ^{16}N source chamber (dots) and scaled umbilical data (open squares) as a function of Z position. The umbilical means were first normalized to the center position value, then scaled with the center ^{16}N run mean.

Chapter 8

Conclusions

The solar neutrino problem remains unsolved and solutions in which neutrino oscillations are involved are still actively being pursued. Neutrino oscillations imply finite neutrino mass and therefore are very important for basic particle physics. The Sudbury Neutrino Observatory is a unique detector that will certainly contribute to our understanding of the SNP and its solutions. The measures of the neutrino signal via the charged-current and neutral-current reactions will permit model-independent tests for neutrino oscillations. Provided the neutrinos do not oscillate into sterile species, the neutral-current measurement will test the standard solar model flux predictions. The impact of SNO on physics can therefore be substantial.

An understanding of the detector response was shown to be extremely important in any SNO neutrino analysis. In particular, the energy response was highlighted and the methods for calibrating and testing this response were described. This included the description of key pieces of apparatus which use short-lived radioisotopes for calibration purposes. The primary calibration system described uses ^{16}N for energy calibrations and has been fully installed in the SNO laboratory. A system for producing ^{8}Li for further energy calibration and position resolution determination was described as well. A prototype system has been tested but has not yet been implemented. Similarly a system that produces ^{17}N for neutron calibration has been developed and tested off-line, but certain components remain to be installed underground.

A detailed description of how the ^{16}N source will be used for energy calibration was given. This included the methods for determining the absolute energy scale and verifying the detector response as a function of event position and direction. The sensitivity of the source for studying the Monte Carlo treatment of the detector's optical properties was determined to be ≈ 0.5 %.

The ^{16}N source has been deployed in SNO in the air-fill stages of commissioning and just recently after the final D_2O fill. Air-fill data permitted a better understanding of the air-fill detector response to γ-rays. In particular it demonstrated flaws in the Monte Carlo treatment of light propagation in the acrylic vessel. D_2O data permitted a preliminary energy scale calibration but the position scans showed that the optical parameters used in the Monte Carlo were inadequate and therefore a more detailed analysis must await further optical calibrations and analysis. Early results have the averaged energy determination uncertainty due to position and direction dependences in the response at 6.1 %. Better optical constants will likely reduce this to the 1 % level. The methods for ^{16}N source energy calibration have clearly been demonstrated. Use of the ^{16}N source for testing the event reconstruction algorithms and measuring the detector angular resolution have also been demonstrated.

Presently the SNO detector is in full operation. The calibration program is ongoing, as are efforts for understanding the detector backgrounds and developing data reduction techniques. Once the data is fully characterized, an active program for analyzing solar neutrino data will begin. Calibration data from the devices described in this thesis will undoubtedly play an important role.

Bibliography

[1] B. T. Cleveland et al., Nucl. Phys. B (Proc. Suppl.) **38**, 47 (1995).

[2] Kamiokande Collaboration, Y. Fukada et al., Phys. Rev. Lett. **77**, 1683 (1996).

[3] GALLEX Collaboration, P. Anselmann et al., Phys. Lett. **B342**, 440 (1995); Phys. Lett. B327, 374 (1994).

[4] SAGE Collaboration, J. N. Abdurashitov et al., Phys. Lett. **B328**, 234 (1994).

[5] SuperKamiokande Collaboration, Y. Fukada et al., Phys. Rev. Lett. **82**, 2430 (1999).

[6] S. L. Glashow, Nucl. Phys. **22**, 579 (1961); A. Weinberg, Phys. Rev. Lett. **19**, 1264 (1967); A. Salam, *Elementary Particle Theory, Proceedings of the Eighth Nobel Symposium*, edited by Svartholm, Almquist and Wiksell, Stockholm (1968).

[7] B. Pontecorvo, Zh. Eksp. Teor. Fiz. **53**, 1717 (1967) [Sov. Phys. JETP **26**, 984 (1968)]; V. Gribov and B. Pontecorvo, Phys. Lett. **B28**, 495 (1969).

[8] L. Wolfenstein, Phys. Rev. **D17**, 2369 (1978) and Phys. Rev. **D20**, 26634 (1979).

[9] S. P. Mikheyev and A. Yu. Smirnov, Nuovo Cimento **C9**, 17 (1986); Yad. Fiz. **42**, 1441 (1985) [Sov. J. Nucl. Phys. **42**, 913 (1985)].

[10] P. Fisher, B. Kayser, and K. McFarland, To appear in Annual Review of Nuclear and Particle Science, Vol. 49 (1999).

[11] SuperKamiokande Collaboration, Y. Fukada et al., Phys. Rev. Lett. **81**, 1562 (1998).

[12] Agleitta M, et al., Europhys. Lett. **8**, 611 (1989); Allison W, et al., Phys. Lett. **B391**, 491 (1997); Becker-Szendy R, et al., Phys. Rev. **D46**, 3720 (1992); Caspar D, et al., Phys. Lett. **B277**, 489 (1989); Kamiokande Collaboration, Fukuda Y, et al., Phys. Rev. Lett. **81**, 1562 (1998).

[13] MINOS Collaboration, Ables E, et al., *P-875: A Long-baseline Neutrino Oscillation Experiment at Fermilab*, FERMILAB-PROPOSAL-P-875 (1995).

[14] Nishikawa K, et al., *E326 KWK-PS proposal*, March 1995; Nucl. Phys. (Proc. Supp.) **B59**, 289 (1997).

[15] LSND Collaboration, Athanassopoulos C, et al., Phys. Rev. Lett. **77**, 3082 (1996); Phys. Rev. **C58**, 2685 (1996).

[16] LSND Collaboration, Athanassopoulos C, et al., Phys. Rev. Lett. **81**, 1774 (1998); Phys. Rev. **C58**, 2511 (1998).

[17] KARMEN Collaboration, K. Eitel and B. Keitnitz. *Proceedings Contribution to Neutrino 98 in Takayama*, Japan, June 4-9 (1998). Nucl. Phys. Proc. Suppl. **77**, 212 (1999).

[18] BooNE Collaboration, Church E, et al., *A proposal for an experiment to measure $\nu_\mu \to \nu_e$ oscillations and ν_μ disappearence at the Fermilab Booster:BooNE*, FERMILAL-PROPOSAL-P-0898 (1997).

[19] J. N. Bahcall, M. H. Pinsonneault, S. Basu and J. Christensen-Dalsgaard, Phys. Rev. Lett. **78**, 171 (1997).

[20] J. N. Bahcall and M. H. Pinsonnealt, Rev. Mod. Phys. **64**, 885 (1992); J. N. Bahcall and M. H. Pinsonneault, Rev. Mod. Phys. **67**, 781 (1995); J. N. Bahcall, S. Basu, and M. H. Pinsonneault, Phys. Lett. **B433**, 1 (1998).

[21] B. T. Cleveland et al., Astrophys. J. **496**, 505 (1998); B.T. Cleveland et al., Nucl. Phys. B (Proc. Suppl.) **38**, 47 (1995); R. Davis, Prog. Part. Nucl. Phys. **32**, 13 (1994).

[22] Kamiokande Collaboration, Y. Fukuda et al., Phys. Rev. Lett. **77**, 11683 (1996).

[23] GALLEX Collaboration, P. Anselman et al., Phys. Rev. Lett. **B342**, 440 (1995); GALLEX Collaboration W. Hampel et al., Phys. Lett. **B388**, 364 (1996).

[24] SAGE Collaboration, V. Gavrin et al., in *Neutrino 96, Proceedings of the XVII International Conference on Neutrino Physics and Astrophysics*, Helsinki, edited by K. Huitu, K. Enqvist and J. Maalampi (World Scientific, Singapore, 1997), p. 14; V. Gavrin et al., in *Neutrino 98, Proceedings of the XVIII International Conference on Neutrino Physics and Astrophysics*, Takayama, Japan, 4-9 June 1998, edited by Y. Suzuki and Y. Totsuka. Nucl. Phys. Proc. Suppl. **77**, 20 (1999).

[25] SuperKamiokande Collaboration, Y. Suzuki, in *Neutrino 98, Proceedings of the XVIII International Conference on Neutrino Physics and Astrophysics*, Takayama, Japan, 4-9 June 1998, edited by Y. Suzuki and Y. Totsuka. Nucl. Phys. Proc. Suppl. **77**, 35 (1999).

[26] J. Bahcall, P. Krastev, and A. Smirnov, Phys. Rev. **D58**, 096016 (1998).

[27] N. Hata and P. Langacker, Phys. Rev. **D50**, 632, (1994) and Phys. Rev. **D56**, 6107 (1997).

[28] A. Cumming and W. C. Haxton, Phys. Rev. Lett, **77**, 4286 (1996).

[29] J. N. Bahcall, *Neutrino Astrophysics*, Cambridge University Press, Cambridge, England (1989).

[30] S. L. Glashow and L. M. Krauss, Phys. Lett. **B190**, 199 (1987).

[31] V. Barger, R. Phillips, K. Whisnant, Phys. Rev. **D34** 980 (1986).

[32] S. J. Parke, Phys. Rev. Lett. **57**, 1275 (1986).

[33] T. Kuo and J. Pantaleone, Reviews of Modern Physics, **Vol. 61** (1989).

[34] E. D. Carlson, Phys. Rev. **D34**, 1454 (1986); J. Boucher, M. Cribier, W. Hampel, J. Rich, M. Spiro, and D. Vignaud, Z. Phys. **C32**, 499 (1986).

[35] R. Barbieri and A. Dolgov, Nucl. Phys. **B349**, 743 (1991).

[36] M. B. Voloshin and M. I. Vysotsky and L. B. Okun, Zh. Eksp. Teor. Fiz., **91**, 7544 (1986); Sov. J. Nucl. Phys., **44**, 440 (1986).

[37] E. Kh. Akhmedov, Phys. Lett. **B213**, 64 (1988).

[38] C-S Lim and W. J. Marciano, Phys. Rev. **D37**, 1368 (1988).

[39] SuperKamiokande Collaboration, Y. Totsuka, Invited talk at the XVth Particles and Nuclei International Conference, PANIC99, Uppsala, June 10-19 (1999).

[40] J. Bahcall and P. Krastev, Phys. Lett. **B436**, 243 (1998).

[41] K. Kubodera and S. Nozawa, Int. J. Mod. Phys. **E3**, 101 (1994).

[42] S. Ying, W. C. Haxton, and E. M. Henley, Phys. Rev. **C45**, 1988 (1992).

[43] S. D. Ellis and J. N. Bahcall, Nucl. Phys. Lett. **A114**, 636 (1968).

[44] J. Bahcall and E. Lisi, Phys. Rev. **D54**, 5417 (1996).

[45] Yu. S. Kopysov and V. A. Kuz'min, Yad. Fiz. **4**, 1031 (1966);Sov. J. Nucl. Phys. **4**, 740 (1967).

[46] The SNO Collaboration, G. T. Ewan et al., *Sudbury Neutrino Observatory Proposal*, SNO technical report SNO-STR-87-12 (1987).

[47] SNO Collaboration members, *The SNOMAN User's Manual.*

[48] Sudbury Neutrino Observatory X-Windows Event Display program, written by Phil Harvey, Queen's University.

[49] P. J. Doe, J. V. Germani, A. W. P. Poon, R. G. H. Roberston, T. D. Steiger, J. F. Wilkerson, T. J. Bowles, A. Hime, M. M. Fowler, P. M. Thornewell, J. B. Wilhemy and J. M. Wouters, *Construction of an Array of Neutral-Current Detectors for the Sudbury Neutrino Observatory*, SNO technical report SNO-STR-95-023 (1995).

[50] The SNO Collaboration, *The Sudbury Neutrino Observatory*, Nucl. Inst. Meth., to be submitted.

[51] R. K. Taplin et al., *Design Description for the SNO SUF Plant*, SNO technical report SNO-STR-96-033 (1996).

[52] J. X. Wang, *Data Analysis of ESC Counting for Ra and Rn*, SNO technical report SNO-STR-95-066 (1996);T. Anderson et al., *Recent Results on Extraction Efficiencies, Systematics, and Fines with MnO_2 Coated Beads*, SNO technical report SNO-STR-95-022 (1995).

[53] X. Zhu, *Study of Vacuum Degassing of SNO Water System*, M.Sc. thesis, Department of Physics, Queen's University (1993);S. Noel, *High Flow Rate Degasser for Removing Radon for the Sudbury Neutrino Observatory Project*, M.Sc. thesis, Department of Physics, Queen's University (1995).

[54] M.-Q. Liu, H. W. Lee, and A. B. McDonald, Nucl. Inst. and Meth. **A329**, 291 (1993).

[55] Figure courtesy of E. Korpach, Queen's University.

[56] E. W. Beier, D. F. Cowan, P. T. Kenner, J. R. Klein, F. M. Newcomer, D. S. McDonald, M. Neubauer, R. Van Berg, R. G. Van de Water, and P. Wittich, *Performance of the Electronics in the Sudbury Neutrino Observatory*, SNO tecnhical report SNO-STR-98-022 (1998).

[57] CN/ASD, *ZEBRA*, CERN (1995).

[58] W. R. Nelson, H. Hirayama and D. W. O. Rogers, *The EGS4 code system*, SLAC report 265 (1985).

[59] MCNP4A, *A Monte Carlo N-Particle Transport Code System*, Radiation Shielding Information Center, Los Alamos National Laboratory, (1993).

[60] CN/ASD, *Geant Detector Description and Simulation Tool*, CERN (1994).

[61] N. Hata et al., Phys. Rev. **D50**, 632 (1994).

[62] CN/ASD. *Physicist Analysis Workstation*, CERN (1998).

[63] R. Brun and F. Rademakers, *The ROOT System*, http://root.cern.ch.

[64] R. J. Ford, *SNO N_2/Dye Laser and Fibre Optic Diffuser Ball System Manual*, SNO technical report SNO-STR-96-056 (1997).

[65] R. J. Ford, *Nitrogen/Dye Laser System for the Optical Calibration of SNO*, M.Sc. Thesis, Queen's University (1993).

[66] E. B. Norman, I. Zlimen, and R. M. Larimer, *Testing a Neutron-Activated NaI Detector as a Low-Energy Calibration Device for SNO*, SNO technical report SNO-STR-93-032 (1993).

[67] M. R. Dragowski, *Sudbury Neutrino Observatory Energy Calibration using Gamma-Ray Sources*, Ph.D Thesis, Oregon State University (1999).

[68] A. W. P. Poon, *Energy Calibration of the Sudbury Neutrino Observatory Using Monoenergetic Gamma-Ray Sources*, Ph.D Thesis, University of British Columbia (1998).

[69] F. Dalnoki-Veress, *Investigation of the Triggered Source Technique for the Calibration of SNO*, M.Sc. Thesis, Carleton University (1996).

[70] Figure courtesy of F. Duncan, Queen's University.

[71] C. J. Jillings, R. J. Ford, A. L. Hallin, P. J. Harvey, R. W. MacLeod, H. B. Mak, P. Skensved, and R. L. Stevenson, Nucl. Inst. and Meth. **A373**, 431 (1996).

[72] R.J. Ford, *Fitting Optical Constants in SNO Using a Pulsed N_2/Dye Laser*, SNO technical report SNO-STR-96-055 (1996).

[73] R. J. Ford, *Calibration of SNO for Detection of ^8B Neutrinos*, Ph.D Thesis, Queen's University (1998).

[74] E. Storm and H. I. Israel, *Photon Cross Sections from 1 keV to 100 MeV for Elements Z=1 to Z=100*, Atomic Data and Nuclear Data Tables, 565 (1970).

[75] G. White Grodstein, *X-ray Attenuation Coefficients From 10 kev to 100 MeV*, National Bureau of Standards Circular 583 (1957).

[76] A. Bielajew et al., *History, Overview and Recent Improvements of EGS4*, KEK Internal report 94-4 (1994).

[77] Y. Koshio, *Study of Solar Neutrinos at Super Kamiokande*, Ph.D Thesis, University of Tokyo (1998).

[78] D. W. O. Rogers, Nucl. Inst. and Meth. **227**, 535 (1984).

[79] M. Lay, *Creation and Detection of Čerenkov Light in the Sudbury Neutrino Observatory* Ph.D Thesis, University of Oxford (1994).

[80] S. J. Brice, *The Elastic Fitter*, SNO technical report, SNO-STR-95-040 (1995).

[81] M. E. Moorhead, *Grid Fitter for Reducing Tails in Spatial Distributions*, SNO technical report SNO-STR-95-042 (1995).

[82] W. Frati and R. Van de Water, *Quad Fitter Introduction- Reconstruction and Pattern Recognition*, SNO technical report SNO-STR-94-030 (1994).

[83] C. J. Jillings, *The Elastic Scattering Reaction in the Sudbury Neutrino Observatory*, Ph.D. Thesis, Queen's University, 1999.

[84] M. G. Boulay and A. L. Hallin, private communication.

[85] R. B. Firestone, *Table of Isotopes*, Eighth Edition, New York: John Wiley & Sons, Inc.

[86] D. R. Tilley, H. R. Weller, and C. M. Cheves, Nuclear Physics **A564**, 1 (1993).

[87] W. Frati, H. Leslie, B. Robertson, H. Robertson, and J. Wilhemy, *Neutron Free Gamma Ray Calibration Sources*, SNO technical report SNO-STR-92-032 (1992).

[88] W. Frati, *Blocking the β's in the ^{16}N Source*, SNO technical report SNO-STR-93-008 (1993).

[89] B. Sur, E. D. Gaudette and R. Deal, *^{16}N:A Calibration Source for SNO*, SNO technical report SNO-STR-93-008 (1993).

[90] E. B. Norman and B. Sur, *^{17}N:A Tagged Neutron Source for SNO*, SNO technical report SNO-STR-94-037 (1994).

[91] F.Ajzenberg-Selove, Nuclear Physics **A490**,1 (1998).

[92] B. Sur, E. D. Earle, R. Deal and E. Gaudette, *^{8}Li: A β Calibration Source for SNO*, SNO technical report SNO-STR-95-054 (1995).

[93] G. Jonkmans, I. S. Towner, and B. Sur, Phys. Rev. **C58**, 1278 (1998).

[94] *Model A-320 Neutron Generator Manual*, MFPhysics Corporation.

[95] V. McLane, C. L. Dunford, and P. F. Rose, *Neutron Cross Sections*, Vol. 2 Academic Press (1988);E. B. Norman and B. Sur, Phys. Rev. **C57**, 2043 (1998).

[96] Targets were fabricated by P. Dmytrenko, Chalk River Laboratories.

[97] B. Sur and E. D. Earle, *Gas Transport Calibration System for SNO: A Preliminary Design Document*, SNO tecnical report SNO-STR-95-053 (1995).

[98] G. Jonkmans, B. Sur, Y. D. Chan, E. Norman, N. Tagg, A. Hamer, W. Frati, and D. McDonald, *TEST RUNS with INTERNAL TRIGGER CHAMBER*, SNO technical report SNO-STR-96-053 (1996).

[99] Private Communication, N. Tagg, University of Guelph.

[100] A. Hamer, G. Jonkmans, B. Sur, N. Tagg, R. Deal, *First Run of the SNO ^{8}Li Calibration System*, SNO technical report SNO-STR-96-29 (1996).

[101] A. Uritani et al., Nucl. Inst. and Meth. **A299**, 233 (1990).

[102] G. Jonkmans and D. Earle, *Construction Report*, SNO technical report SNO-STR-97-015 (1997).

[103] G. Jonkmans and B. Sur, *Commissioning Plan*, SNO technical report SNO-STR-97-016 (1997).

[104] B. Sur, A. Hamer, G. Jonkmans, J. Heise, J. Hewitt, and H. Seifert, *DT Generator Commissioning*, SNO technical report SNO-STR-97-049 (1997).

[105] K. Murnaghan, *SNO Calibration Source Optimization*, SNO technical report SNO-STR-95-052 (1995).

[106] J. F. Ziegler, J. P. Biersack and U. Littmark, *The Stopping and Range of Ions in Solids*, Pergamon Press, New York (1985).

[107] A. Hamer and B. Sur, *Targets for the N-16 Calibration Source*, SNO technical report SNO-STR-97-041 (1997).

[108] R. B. Bird, W. E. Stewart, and E. N. Lightfoot, *Transport Phenomenon*, John Wiley and Sons, New York, 1960.

[109] L. P. Boivin et al., Applied Optics **25**, 877 (1986).

[110] N. K. McCauley, *Muons and the* ^{16}N *source in the AirFill Runs at the SNO detector*, SNO internal report (1999).

Curriculum Vitae

Name:	Andre Stephane Hamer
Place and Year of birth:	Oshawa, Canada, 1968
Education:	Ph.D (present program)
	Queen's University, Kingston, Ont. 1999
	Master of Science
	Queen's University, Kingston, Ont. 1994
	Bachelor of Science
	(Honours Physics)
	University of Toronto, Toronto, Ont. 1992
Experience:	Teaching and Research Assistant (Physics Department)
	Queen's University, 1992 - 1999
Awards:	Reinhardt Fellowship 1992
	Dean's Award(Queen's) 1993
	Queen's Graduate Award 1993-1997
	Queen's Graduate Fellowship 1994-1997